Precision measurement of jets at the ATLAS Experiment

A thesis submitted to the University of Manchester for the degree of

Doctor of Philosophy

in the Faculty of Engineering and Physical Sciences

2012

Gareth John Ashley Brown

School of Physics and Astronomy

Contents

Total word count: 19962

List of Tables

List of Figures

Abstract

This thesis describes the measurements of jet activity in the rapidity region between a dijet system formed in proton-proton collisions at a centre-of-mass energy of 7 TeV. The data used were collected by the ATLAS detector during 2010 at the Large Hadron Collider at CERN. A number of observables that probe additional quark and gluon radiation in the dijet topology are studied. The development and performance of the monitoring system for the ATLAS calorimeter high level trigger is described. The performance of the jet calibration and a study of the properties of jets in the forward calorimeter is also given. The fraction of events that survive a veto on jets with transverse momentum above a jet veto scale, Q_0, in the rapidity region between the dijet system is measured for dijets with mean transverse momentum $50 < \overline{p_{\mathrm{T}}} < 500$ GeV and rapidity separation, Δy, of up to six. The mean number of jets that have a transverse momentum above the jet veto scale in the rapidity region between the dijet system is also measured. These measurements are compared to state-of-the-art theoretical calculations from HEJ and POWHEG, and also compared to PYTHIA and HERWIG++ Monte Carlo generators. The results of a preliminary analysis of dijet events with a large rapidity separation are given. In this analysis azimuthal decorrelation variables are also been measured.

Declaration

No portion of the work referred to in this thesis has been submitted in support of an application for another degree or qualification of this or any other university or other institution of learning.

Gareth John Ashley Brown
School of Physics and Astronomy
University of Manchester
Oxford Road
Manchester
M13 9PL
November 2012

Copyright

Acknowledgements

I am sincerely and heartily grateful to my supervisors, Fred Loebinger and Andy Pilkington, for their support, patient guidance and enthusiasm, throughout the last four years. I would also like to thank Mark Owen for his continual help throughout my PhD, and Denis Damazio who supervised and guided me through my service work.

Many thanks to the Manchester HEP group who made a very friendly and intellectually stimulating environment to study. I would like to thank the many friends I have met in Manchester and while at CERN who made the last four years very enjoyable. I would also like to thank Vik and John who shared in the late night work and thesis writing.

I am truly indebted and thankful to my friends and colleagues who I worked with and learnt from through my PhD, in particular James, Caterina, Dag, Pier-Olivier and Pauline.

Special thanks to my parents and my family for their love and support.

Chapter 1

Introduction

ATLAS is a multipurpose detector built with the aim of measuring a wider variety of physics processes, which occur in the high energy proton-proton collisions produced by the Large Hadron Collider (LHC) at CERN. The majority of these measurements are influenced by the presence of jets. Examples include physics signals with jet final states or jets produced in association with other particles. Stringent analysis cuts on additional jets used, for example, in the search for new physics, can force the event topology into regions of phase space that are difficult to calculate in fixed-order perturbation theory. This means the theory models used to predict backgrounds may be imprecise. It is important to test model predictions with precise measurements in similar phase space regions.

Dijet production is ideal for testing the model predictions due to the large number of events even in the phase space near the kinematic limit. Dijet production with a large average jet transverse momentum or large rapidity separation reflect the cuts used in heavy resonance searches and vector boson production of the Higgs boson. Precision measurements of observables sensitive to higher order Quantum Chromo Dynamics (QCD) emission can test the appropriate models.

The fraction of dijet events which survive a jet veto on the jet activity between the dijet system is studied as a function of the rapidity separation of the dijet

system, the mean transverse momentum of the dijet system and the value of the jet veto for separations up to six units of rapidity in the range of mean transverse momentum $50 < \overline{p_{\mathrm{T}}} < 500$ GeV.

In Chapter 2 of this thesis the Standard Model (SM) of particle physics is reviewed with particular emphasis on the relevant aspects of QCD and the analysis observables are defined and discussed. In Chapter 3 both the LHC experiment and the ATLAS detector are described. Monitoring of the calorimeter systems is described in Chapter 4. In-situ methods used to assess the effectiveness of jet calibration and forward jet properties are presented in Chapter 5. Chapter 6 presents the analysis which formed the basis of the first ATLAS paper [1] on dijet production with a veto on jets bounded by the dijet system, as a function of the dijet rapidity separation and the average transverse momentum. In Chapter 7 the analysis is extended to study dijets with a large rapidity separation, and a measurement of the azimuthal decorrelation is made. This analysis is currently in the process of internal review by the ATLAS collaboration [2]. A summary and conclusion of the thesis is given in Chapter 8.

Chapter 2

Theory

The Standard Model (SM) of particle physics is the theoretical framework that describes the interactions of the strong, electromagnetic, and weak forces. Figure 2.1 shows the bosons and fermions in the SM. The matter particles are represented in three generations of fermions, with particles in each generation being heavier than the previous. The electromagnetic force is mediated by the photon, which interacts with charged particles. The weak force in mediated by the W and Z bosons. The strong force describes the interactions between quarks and gluons, and is mediated by the gluon. Finally, there is also the Higgs boson, which is the remnant of the Higgs field that was introduced to give mass to the bosons and fermions. The strong force is described by QCD. This thesis is concerned with QCD measurements, and more detail about QCD is given in this chapter.

2.1 QCD

The QCD Lagrangian is given by

$$\mathcal{L} = -\frac{1}{4}F^a_{\alpha\beta}F^{\alpha\beta}_b + \sum_q \bar{q}_j(i\partial\!\!\!/ - m_q)q^j + g_s\sum_q \bar{q}_i\gamma_\mu t^a_{ik}q^k A^\mu_a, \tag{2.1}$$

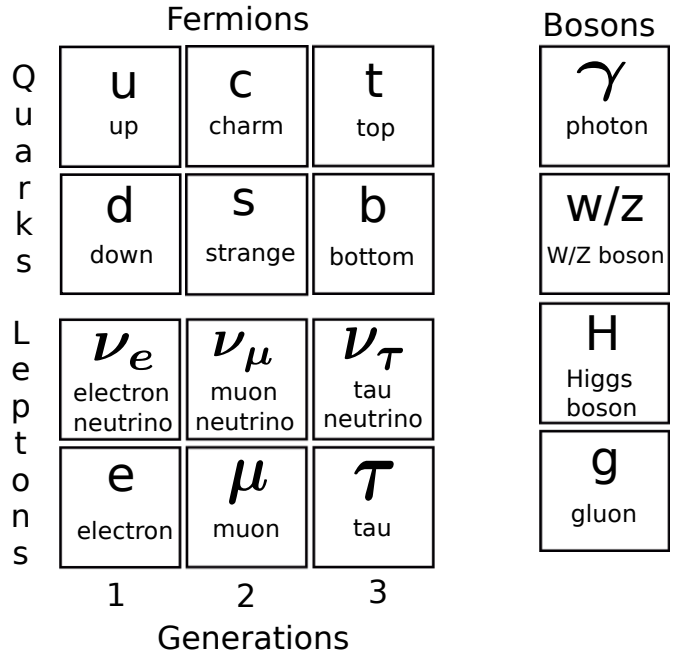

Figure 2.1: The fundamental particles in the Standard Model.

where A^μ_a is the gluon field, $t^a_{ik} = \frac{1}{2}\lambda_a$ with λ_a being the Gell–Mann matrices, γ_μ are the γ matrices, m_q is the mass of the quark, q and $\bar{q}$ are the spin-$\frac{1}{2}$ quark field, and

$$F^a_{\alpha\beta} = \partial^\alpha A^\beta_A - \partial^\beta A^\alpha_a + g_s f_{abc} A^\alpha_b A^\beta_c. \tag{2.2}$$

Here, repeated indices imply summation. Greek characters represent Lorentz vector components and Latin characters representing the different colour charge of the quarks and gluons.

The first term in Equation 2.1 is concerned with the gluon self-coupling and gluon propagator. The product of $F^a_{\alpha\beta}F^{\alpha\beta}_b$ results in terms with g^2, which correspond to a four-gluon interaction, terms with g, which correspond to the three-gluon interaction and other terms that correspond to the basic gluon propagator. The second term in Equation 2.1 corresponds to the basic quark propagator without a gluon interaction. The final term in Equation 2.1 is the gluon-quark interaction.

2.1.1 Asymptotic Freedom and Confinement

The coupling constant, $\alpha_s = g_s^2/4\pi$, is used to quantify the strength of the partonic interactions. Renormalisation is required due to ultraviolet divergences that arise using perturbative QCD (pQCD). This procedure introduces an additional mass scale, μ. The coupling constant at a momentum scale, Q, relative to a scale μ at one-loop order is given by

$$\alpha_s(Q^2) = \frac{\alpha_s(\mu^2)}{1 + b\alpha_s(\mu^2)\ln(\frac{Q^2}{\mu^2})}, \tag{2.3}$$

where

$$b = \frac{33 - 2n_f}{12\pi}. \tag{2.4}$$

Here, n_f is the number of active flavours of quarks and b is positive for all n_f in the SM.

The renormalisation scale μ is arbitrary and can be freely chosen. Measurements of α_s are made at various values of Q and are typically compared at $\alpha_s(M_Z^2) = 0.1184$ [3], where M_Z is the mass of the Z boson. This allows the calculation of α_s at other scales, though as Q gets small, α_s gets large.

The running of α_s with the scale (Equation 2.3) demonstrates two properties of QCD. First, as the value of Q increases, corresponding to probing smaller distances, the coupling constant becomes small and the quarks and gluons behave as if they were free particles. QCD therefore has asymptotic freedom. Second, as Q gets small, the coupling value of α_s gets very large. This hints towards the QCD feature known as confinement, which is the observation that quarks and gluons are always bound in colour neutral states, namely hadrons.

2.1.2 Hadron – Hadron Cross Section

The QCD factorisation theorem suggests that the hadronic cross-section of a given process can be split into the hard partonic scattering process, which can be

calculated using pQCD, and a part that describes the non-perturbative structure of the hadron, characterised using the parton distribution functions (PDFs) [4]. The cross-section for the process shown in Figure 2.2 is given by,

$$\sigma_{AB} = \int\int dx_a dx_b f_{a/A}(x_a) f_{b/B}(x_a) \hat{\sigma}_{ab\to X}, \tag{2.5}$$

where A and B are the initial protons, a and b are different combinations of quarks and gluons, x_a is the fraction of the proton energy that parton a carries, $f_{a/A}(x_a)$ is the PDF which, to leading order, represents the probability of finding a parton with energy fraction x_a within A, and $\hat{\sigma}_{ab\to X}$ is the partonic cross-section for the sub-process $ab \to X$. The partonic cross-section is given by

$$d\hat{\sigma}_{a,b\to X} = \frac{1}{\hat{s}} |\mathcal{M}_{a,b\to X}|^2 d\Phi_n, \tag{2.6}$$

where a and b represent the incoming partons, $\hat{s} = (k_a + k_b)^2$ where k_i is the 4-momentum of a parton i, $d\Phi_n$ is the n-body phase space, and $\mathcal{M}$ is the matrix element that is calculated using the Feynman rules [5]. If X is a final state consisting of just quarks and gluons, the Feynman rules can be derived from the QCD Lagrangian.

Collinear or soft gluon emission from the initial or final state lead to infra-red (IR) divergences. A factorisation scale μ_F is defined such that gluon emissions with a momentum less than μ_F are absorbed into the PDFs, and only emissions above this value are calculated as part of the matrix element. The PDFs have been measured at the electron-proton collider HERA and at fixed-target lepton-nucleon experiments for a range of x and Q^2 values [6–8].

2.1.3 Jet Formation

From pQCD, it is expected that there is partonic emission off the final state partons, and the emission has a high probability if it is either soft or collinear. The

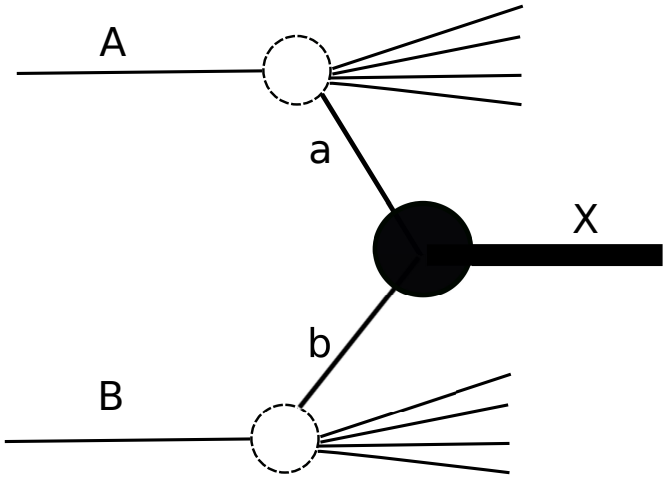

Figure 2.2: Illustration showing hadron-hadron interaction through partons a and b going to X.

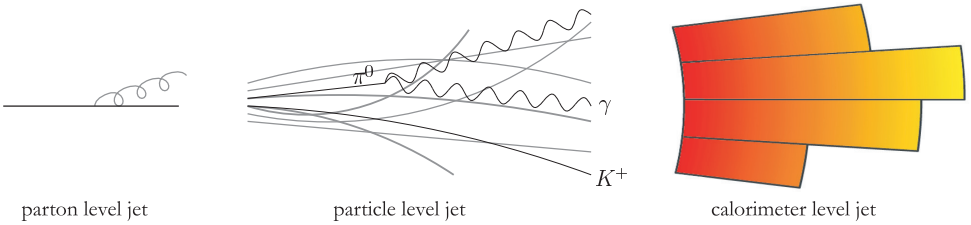

Figure 2.3: Illustration of a jet at parton, particle and calorimeter levels. Illustration from Dag Gillberg.

resulting partons can also emit partons, and a partonic cascade occurs. Confinement requires that all observable particles are colour neutral. This will only occur when there is a low relative momentum between partons. This cascade continues until the parton's energies are at the hadronic scale, $\mathcal{O}(1\text{GeV})$, and they bond into hadrons. The result is a cascade of hadrons in the direction of the original parton.

Calculations with partons in the final state are performed using a jet algorithm. The jet algorithm clusters nearby partons into a single object. The jet algorithms can be applied to calculations at a particular order in perturbation theory, to final state hadrons, or to detector energy deposits. Figure 2.3 shows an illustration of a jet at different levels.

2.2 Dijet Production

The main analysis of this thesis is directed towards dijet production with a veto on additional jet radiation between the dijets. Dijet production cross-section can be calculated using Equation 2.5 with the $\hat{\sigma}$ being the partonic cross-section for $2 \rightarrow 2$ scattering. Measured dijet production cross-sections as a function of the dijet kinematics, for instance the dijet mass, can be compared to leading order (LO) and next-to-leading order (NLO) cross-section calculations. LO cross-section calculations have the lowest order of α_s needed to get the correct final state; for dijets this is α_s^2. Some of the LO parton scattering diagrams are shown in Figure 2.4. NLO cross-section calculations consist of the LO cross-sections with α_s^2, plus the next order in the perturbative series expanded in α_s, i.e. α_s^3. LO and NLO calculations are examples of fixed-order calculations. The dijet cross-section measured by the ATLAS Collaboration is compared to NLO cross-section calculation in Reference [9], with an agreement within the experimental uncertainty.

When describing pp collisions, it is useful to define a co-ordinate system. The z-direction is defined as the collision axis, with the x–y plane defined perpendicular to the collision axis. For an object with energy, E, and momentum, p, the rapidity, y, of the object is defined by

$$y = \frac{1}{2} \ln \left(\frac{E + p_z}{E - p_z} \right), \tag{2.7}$$

where p_z is the longitudinal z component of momentum. The azimuthal angle, ϕ, is defined as the angle in the x–y plane around the collision axis. The transverse momentum, p_{T}, is defined as

$$p_{\mathrm{T}} = \sqrt{p_x^2 + p_y^2}. \tag{2.8}$$

Both p_{T} and differences in rapidity are Lorentz invariant in boosts in the z-direction [10].

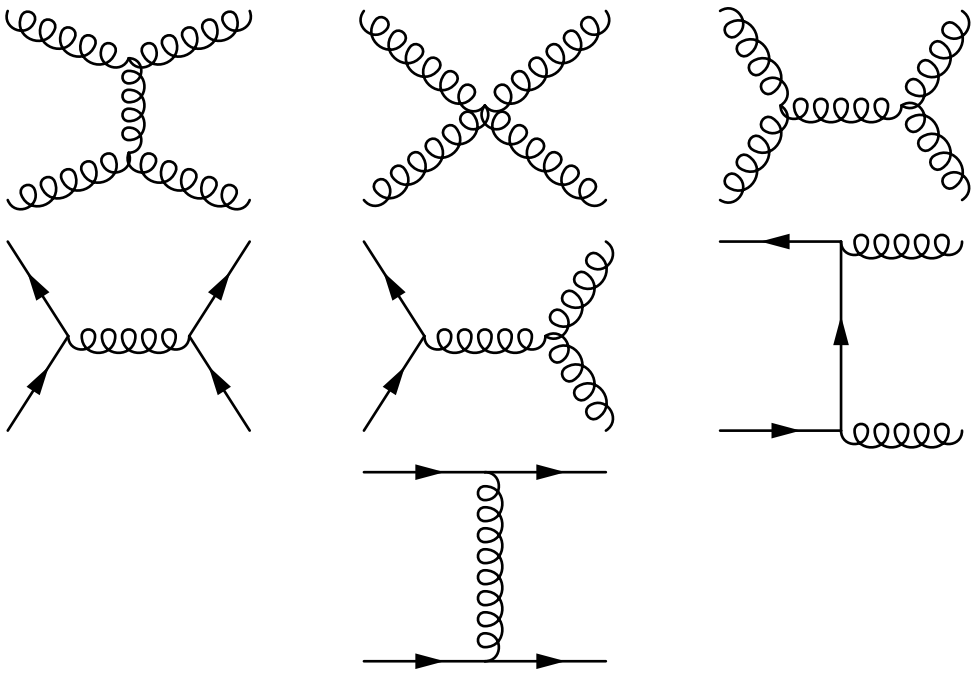

Figure 2.4: Some of the LO Feynman diagrams for dijet production. The straight lines represent quarks, and the curly lines represent gluons. The arrows on the fermion lines going from left-to-right and right-to-left distinguish quarks and anti-quarks respectively.

To study the additional radiation in the dijet region, the fraction of events that do not contain an additional jet between the the two jets is measured. This is the gap fraction, defined as

$$f_{gap}(Q_0) = \frac{\sigma_0}{\sigma}, \tag{2.9}$$

where σ is the dijet cross-section, σ_0 is the cross-section for a dijet system without a parton with p_{T} above the jet veto scale, Q_0, in the rapidity region spanned by the dijet system. The gap fraction is studied as a function of the dijet rapidity separation, $\Delta y = |y_1 - y_2|$, the average transverse momentum of the dijet, $\overline{p_{\mathrm{T}}} = (p_{\mathrm{T}1} + p_{\mathrm{T}2})/2$ and the veto scale, Q_0. The dependence of the gap fraction on Δy, $\overline{p_{\mathrm{T}}}$, and Q_0 is studied after keeping two of the variables fixed.

The dijet cross-section can be calculated at a fixed order using pQCD. However, for some regions of the dijet kinematics or veto jet scale, the pQCD calculation of σ_0 requires increasing number of higher order terms, and so a resummation

is done. Figure 2.5 illustrates the different effects that need to be considered for different regions of the dijet kinematics and jet veto scale. In particular, putting the dijet kinematics to high Δy or to large values of Q/Q_0 requires sophisticated calculation tools, and resummation to all orders in perturbation theory is necessary [11, 12]. As discussed in Reference [13], when considering soft radiation into the region between the two jets, terms arise of the form

$$\alpha_s \Delta y \log \frac{Q}{Q_0}. \tag{2.10}$$

If Δy and $\log(Q/Q_0)$ are small then these terms are small, however this is not true if either term is large, and resummation is required.

A number of other variables are used to probe the effect of higher order QCD. The azimuthal decorrelation variables measure $\Delta\phi$ of jets. For leading order dijet production, $\Delta\phi \approx \pi$, however gluon emission changes this and moves them away from $\Delta\phi \approx \pi$. The azimuthal decorrelation observables considered in this thesis are $d\sigma/d\Delta\phi$, $\langle\cos(\pi - \Delta\phi)\rangle$ and $\langle\cos(2\Delta\phi)\rangle$, which were proposed in [14–17]. The mean number of jets in the rapidity region spanned by the dijet system is another probe of higher order QCD, and suggested in [18].

2.3 Jets

Jets are defined using an algorithm that clusters nearby objects together. A jet finding algorithm needs to be collinear and infrared safe. Collinear safety is the requirement that the jet finding should be unaffected by particles radiated at small angles to the original particle. Infrared safety requires that the jet finding is unaffected by the addition of soft radiation in the event.

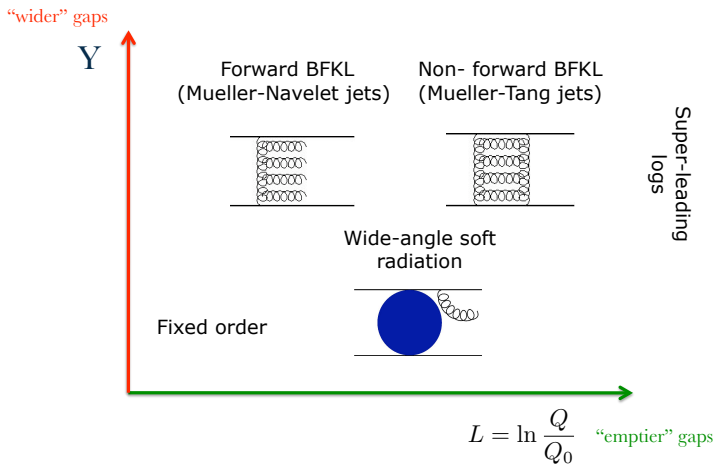

Figure 2.5: Illustration depicting different effects that are important for the gap fraction calculation for dijet rapidity separation, $Y = \Delta y$, and $L = \ln(Q/Q_0)$. Figure taken from [19].

2.3.1 Anti-k_t jets

The standard jet finding algorithm used in ATLAS is the anti-k_t algorithm [20], which is a sequential recombination algorithm. The algorithm defines merging scales for each main pair of objects in the event,

$$d_{ij} = \min\left(\frac{1}{k_{\mathrm{t}j}^2}, \frac{1}{k_{\mathrm{t}i}^2}\right)\frac{\Delta R_{ij}^2}{R^2} \tag{2.11}$$

and each individual object,

$$d_{iB} = \frac{1}{k_{\mathrm{t}i}^2}, \tag{2.12}$$

where $\Delta R_{ij} = \sqrt{(y_i - y_j)^2 + (\phi_i - \phi_j)^2}$, R is the intrinsic distance parameter of the algorithm, and $k_{\mathrm{t}i}^2$ and $k_{\mathrm{t}j}^2$ are the transverse momenta of objects i and j, respectively. The algorithm combines the objects into jets in the following way:

1. Find the minimum of d_{ij} and d_{iB}.

2. If $d_{ij}^{min} < d_{iB}^{min}$ then combine the two objects.

3. If $d_{ij}^{min} > d_{iB}^{min}$ then define object i as a jet and remove it from list of objects.

4. Continue iterating until there is no object left in the list of objects.

The anti-k_t jet finding algorithm combines the objects around the highest p_{T} objects first, which have a $\Delta R < R$, then subsequently lower p_{T} objects. Only jets that have a p_{T} greater than a p_{T} cut-off are kept in the jet collection.

There are many algorithms that are theoretically safe (both IR and collinear safe). The anti-k_t algorithm was chosen to be the standard because it produces circular jets and has a good behaviour under noise and pile-up. The ATLAS jet algorithm recombines jet with two R parameters, 0.4 and 0.6, and full four-momentum recombination.

2.4 MC Event Simulation

Monte Carlo (MC) event simulation is used to compare data to theoretical predictions. They aim to give a full description of a hadron-hadron interaction. As discussed in Section 2.1, the calculation can be factorised to separate the perturbative and non-perturbative parts. First, the differential partonic cross-section is calculated to model the kinematics of the hard interaction. This will consist of n high p_{T} partons in the final state. Parton showering (PS) and hadronisation algorithms are used to turn the partonic final state into a hadronic one.

The PS simulates the higher order contributions to the calculation from soft and collinear parton emission. The effectiveness of the PS for soft and collinear emissions is tested through jet shapes [21]. The PS calculates soft and collinear contributions by summation of leading logarithms [5]. Through the parton showering, the high p_{T} partons successively radiate partons until all partons are at a scale of a few GeV. Once at this scale, hadronisation combines the partons together to make colour neutral hadrons. Emission from multiple parton-parton

interactions (MPI) within one proton-proton interaction are modeled by the MCs and the emissions are included in the event before the hadronisation.

2.4.1 MC Generators

PYTHIA

PYTHIA [22] is a general-purpose MC program with a large library of LO sub-processes, including the LO QCD matrix elements for the $2 \to 2$ sub-processes used for dijet production. The PYTHIA PS orders emissions in transverse momentum and has a veto to ensure angle ordering. The hadronisation used in PYTHIA is based on the Lund string model [23]. The version of PYTHIA used in the analyses presented is PYTHIA 6.4.2.3 with the MRST LO* PDF [8] and the AMBT1 tune [24].

The dijet cross-section is falling in both $\overline{p_{\mathrm{T}}}$ and Δy. To get a large number of events in the high $\overline{p_{\mathrm{T}}}$ and Δy regions, a filter is applied to the centrally produced PYTHIA samples used in Chapters 6 and 7 to obtain a constant distribution in $\overline{p_{\mathrm{T}}}$ and Δy. Event weighting factors are stored which allows the original distribution to be recovered. To improve the description of data, multiple proton-proton interaction, "pile-up", is included.

Unlike the other MC generators considered, the PYTHIA events are passed through a full ATLAS detector simulation, based on GEANT4 [25], which results in a sample of fully simulated events that can be directly compared to data.

HERWIG++

HERWIG++ [26] is another general-purpose MC program which has LO QCD matrix elements for the $2 \to 2$ sub-processes. HERWIG++ has a PS that evolves the partons using angular ordering of emissions. The hadronisation used in HERWIG is the cluster model [27] which forces all the gluons remaining from

the PS to split into quark anti-quark pairs. The version used is HERWIG++ 2.5.0 [26] using the MRST LO* PDF and underlying event tune of LHC-UE7-1 [28].

POWHEG

The POWHEG-box generator [29–31] is used to simulate NLO dijet events. The events are passed through to both PYTHIA and HERWIG for parton showering, hadronisation and MPI. Events were generated with the MSTW 2008 NLO PDF [8]. POWHEG is expected to be better in describing observables that are dependent on the third jet than LO MCs as it explicitly calculates the third jet. The parton showering from both HERWIG and PYTHIA simulate soft emission which would correspond to the small $\log(Q/Q_0)$ region of Figure 2.5.

HEJ

High Energy Jets (HEJ) [12, 32] is a parton level generator. It implements an all-order description of hard wide-angle emissions. It is best suited for events with a large Δy between the most forward and most backward jets. Emitted gluons have similar momenta and are ordered in rapidity. Due to this, HEJ is expected to model the data better than fixed order calculations in the large Δy region in Figure 2.5. Events were generated with the MSTW 2008 NLO PDF.

Chapter 3

The LHC and ATLAS

The basic properties of the LHC are summarised in Section 3.1. Sections 3.2 and 3.3 define the ATLAS coordinate system and give an overview of the detector, working outwards from the beam line. A discussion of the important aspects of jets within ATLAS is given in Section 3.4.

3.1 The Large Hadron Collider

The Large Hadron Collider (LHC) is situated 100 m below the border between Switzerland and France near the Swiss city of Geneva. The LHC was designed to provide two proton beams with 2808 bunches in each beam colliding with 25 ns bunch spacing at a centre-of-mass energy of 14 TeV. Around the LHC ring, which is 26.6 km long, there are four interaction points. The four experiments at these interaction points are ATLAS, CMS, LHCb and ALICE. ATLAS and CMS are general purpose detectors designed to be able to detect a broad range of physics processes. ALICE is designed to investigate heavy ion collisions, and LHCb is designed to explore CP violation and rare B-hadron decays. Figure 3.1 shows the layout of the LHC, and the four experiments.

A series of accelerators provide proton bunches to the LHC at an energy of

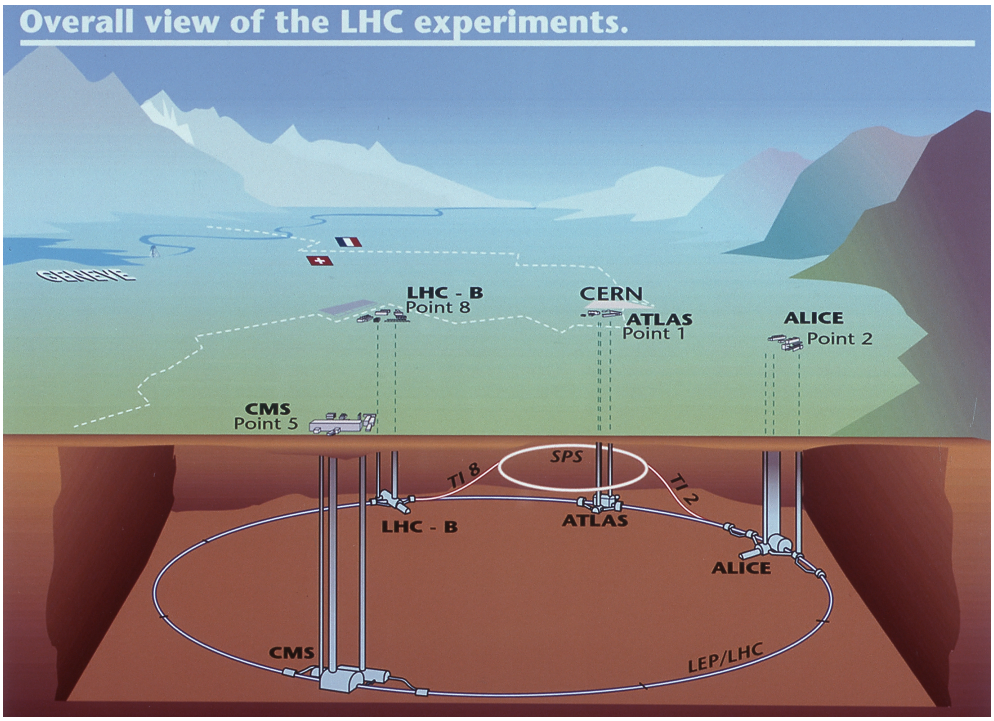

Figure 3.1: The Large Hadron Collider and the sites of the 4 main LHC experiments.

450 GeV. The proton bunches are then accelerated around the LHC by an array of superconducting dipole magnets to provide a beam energy up to 7 TeV. The beam energy during the 2010 and 2011 proton-proton collisions was 3.5 TeV, in 2012 it was 4 TeV.

3.1.1 Luminosity

The event rate for $pp \to X$ is

$$R_X = L\sigma_X, \tag{3.1}$$

where σ_X is the cross-section for the process and L is the instantaneous luminosity. Achieving a large integrated luminosity,

$$\mathcal{L} = \int L \cdot dt, \tag{3.2}$$

is important for observing rare physics processes that have a low cross-section. Accurate luminosity determination is important for measuring differential cross-sections of processes from the event rate.

Instantaneous luminosity is defined by,

$$L = \frac{N_b^2 n_b f_{rev} \gamma_r}{4\pi \epsilon_n \beta^\star} F, \tag{3.3}$$

where N_b is the number of particles per bunch, n_b is the number of colliding bunches per beam, f_{rev} is the revolution frequency, γ_r is the relativistic gamma factor, ϵ_n is the normalised transverse beam emittance, $\beta^\star$ is the β function at the interaction point, and F is the geometric luminosity reduction factor due to the crossing angle of the beams. Due to falling numbers of protons in each bunch and the gradual increase in the beam emittance, the instantaneous luminosity will fall as the length of the run increases. The peak instantaneous luminosity is the maximum instantaneous luminosity for a given data-taking run.

Equation 3.3 is useful to understand both the luminosity and how to increase it. Experimentally, the instantaneous luminosity can be determined by measuring the interaction rate in various ATLAS sub-detectors. The luminosity defined by the interaction rate is,

$$L = \frac{\mu n_b f_{rev}}{\sigma_{inel}} = \frac{\mu_{vis} n_b f_{rev}}{\sigma_{vis}} \tag{3.4}$$

where μ is the number of inelastic collisions per bunch crossing, σ_{inel} is the inelastic cross-section for a proton-proton collision, μ_{vis} is the number of visible inelastic collisions per bunch crossing, and σ_{vis} is a calibration constant related to the visible inelastic cross-section. This is obtained in special runs using Van der Meer scans and provide a luminosity uncertainty of 3.4% [33].

2010 run

The 7 TeV centre-of-mass proton-proton run in 2010 was the first substantial data-taking period provided by the LHC. The initial runs provided peak instantaneous luminosity of $\approx 0.01 \times 10^{30}\text{cm}^{-2}\text{s}^{-1}$ from one pair of interacting bunches with a very low number of protons per bunch. By the end of the 2010 data-taking run, the peak luminosity was $\approx 2 \times 10^{32}\text{cm}^{-2}\text{s}^{-1}$ from 348 colliding bunches. The luminosity increase was mainly achieved by increasing the number of colliding bunches per beam and the number of protons per bunch, though decreasing the $\beta^{\star}$ and reducing the beams crossing angle also increased the luminosity.

The data are split into luminosity blocks, runs and periods. A luminosity block corresponds to the luminosity information stored in two minute intervals during a run. A data run is a group of luminosity blocks consecutively taken. A data period is a group of data runs with similar beam parameter conditions.

The 2010 data taking run was split into nine different data periods, which corresponded to a total integrated luminosity delivered of 48.1 pb^{-1}. Table 3.1 shows the data periods for the 2010 LHC run, and how the beam conditions and peak luminosity changed. In addition, periods G-I used bunch trains where bunches are grouped together with 150 ns spacing between the bunches. As instantaneous luminosity increased, the level of "pile-up", which is multiple proton-proton interactions in the same bunch crossing, increased.

3.2 The ATLAS Coordinate System

The ATLAS experiment uses a right-handed Cartesian coordinate system. The beam line defines the z-axis, with the x-y plane being perpendicular to this. The positive x direction is defined going from the interaction point to the centre of the LHC ring. The positive y direction points upwards from the interaction

Period	Date	Peak Luminosity $\mathrm{cm}^{-2}\mathrm{s}^{-1}$	N_b $\times 10^{11}$	n_b
A	Mar 30 - Apr 18	0.004	< 0.01	1
B	Apr 23 - May 17	0.06	0.01-0.6	1-3
C	May 18 - June 5	0.2	0.7-1.9	3-8
D	June 18 - July 19	1.6	3-8	2-8
E	July 29 - Aug 18	3.9	12-14	16
F	Aug 19 - Aug 30	10	35-100	32-36
G	Sept 22 - Oct 7	70	100-200	50-186
H	Oct 8 - Oct 18	150	250-350	233-300
I	Oct 24 - Oct 29	210	350-400	300-350

Table 3.1: Beam information for the different data taking periods in 2010 data.

point. The detector side in the positive z direction is called A and the side in the negative z direction C. The azimuthal angle, ϕ, is defined as the angle in the x-y plane around the beam, and the polar angle, θ, is the angle to the beam line. Using the polar angle, pseudorapidity η is defined by

$$\eta = -\ln \tan\left(\frac{\theta}{2}\right). \tag{3.5}$$

Pseudorapidity provides a close approximation to the rapidity defined in Equation 2.7. The angle between two objects, ΔR, is defined by

$$\Delta R = \sqrt{(\Delta\eta)^2 + (\Delta\phi)^2}. \tag{3.6}$$

All transverse variables (such as transverse momentum, p_T, and transverse energy, E_T) use only the x and y components of the variable and so are defined in the x-y plane.

3.3 The ATLAS Detector

A schematic of the ATLAS detector is shown in Figure 3.2. In this section the different detectors which make up the ATLAS detector will be reviewed. First

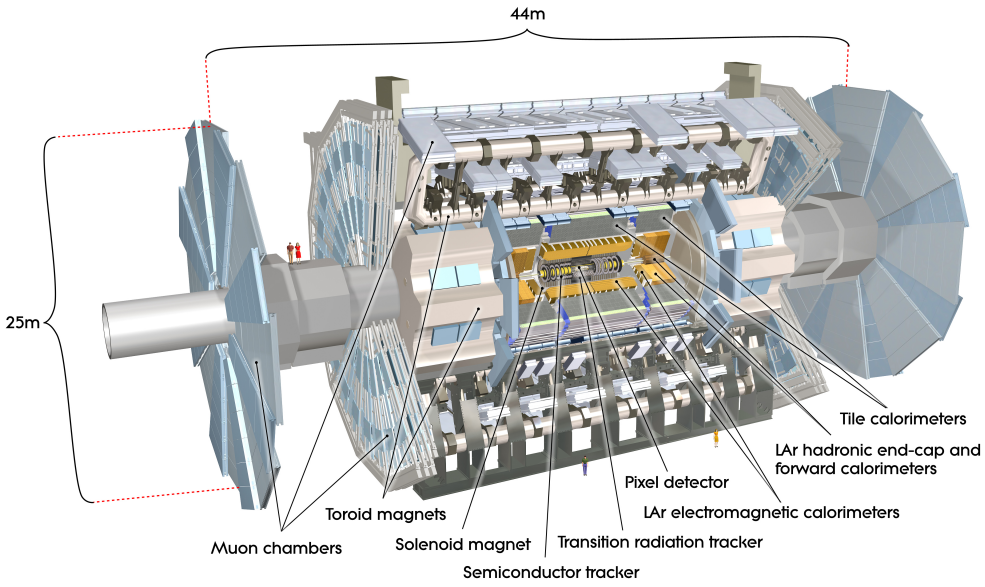

Figure 3.2: Schematic of the ATLAS detector. Figure from [34].

the magnet system, which provides the magnetic field for the tracking detectors, will be described. Next the inner detector, the closest detector to the beam line, will be described, followed by the calorimeter systems and the muon detectors. The calorimeters have been described in higher detail due to their relevance to this thesis.

3.3.1 Magnet System

The purpose of the magnet system in ATLAS is to bend charged particles, such that the tracking detectors can measure their transverse momentum using the curvature of the track. There are two different tracking regions, one very close to the interaction point which measures all charged particles, and then one tracking system at the outermost part of the detector which just measures the muon tracks. There is a different magnet system for each tracking region. The magnet providing a field close to the interaction point is solenoidal, and provides a 2 T field for the inner detector. The system for the muon tracking has a set of

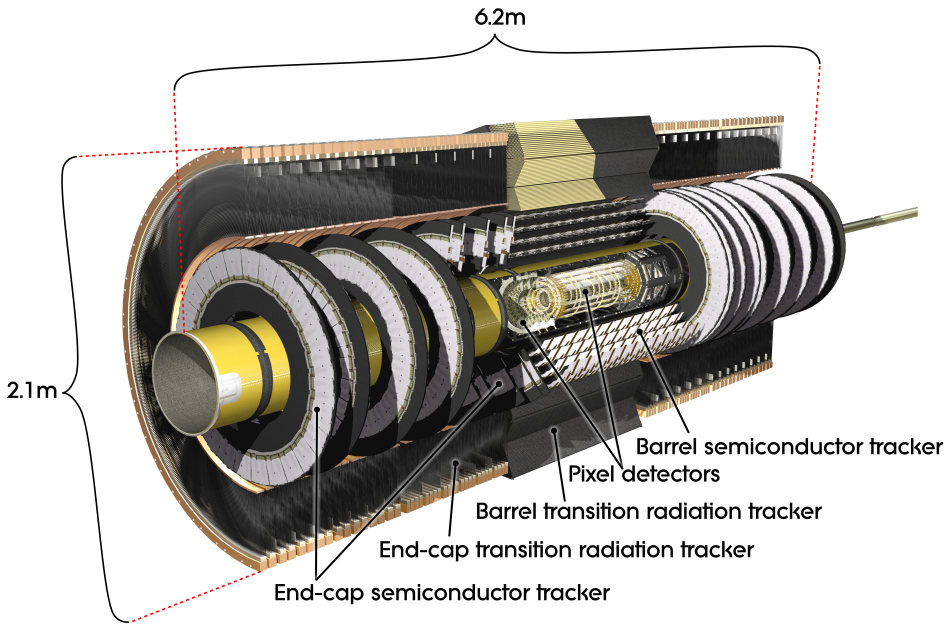

Figure 3.3: A schematic of the ATLAS Inner Detector. Figure from [34].

toroidal magnets. One set of barrel toroids combine with the two end-cap toroids to provide the muon tracking with a magnetic field of 0.5 T and 1 T, respectively.

3.3.2 Inner Detector

The inner detector (ID) provides full tracking information for $|\eta| < 2.5$. The purpose of the ATLAS tracking detectors is to make high precision measurements of charged particle tracks near the beam line. These measurements are used for primary and secondary vertex finding and momentum determination. The tracking detectors have to be able to deal with the high track multiplicity expected at the design luminosity of the LHC.

Figure 3.3 shows the different components of the ATLAS inner detector that will be discussed. Both the pixel detector and the semiconducting tracker have a tracking region out to $|\eta| < 2.5$, and the transition radiation tracker goes out to $|\eta| < 2$.

The pixel detector is the closest to the interaction point, and thus has the

highest granularity of the inner detector trackers. There are three pixel layers in the barrel region each having a 2d segmentation, with a minimum size in $r\phi \times z$ of 50×400 μm^2, giving a well measured space point. The main use of the pixel detector is to find B hadrons and τ leptons.

Further from the interaction point is the Semi Conductor Tracker (SCT) which is less granulated. The main use of the SCT is determining track momenta, impact parameters and vertex positions.

Furthest away from the interaction point is the Transition Radiation Tubes (TRT) detector, which provides a large number of hits per track. The position accuracy of these hits is less accurate than that from the pixel and SCT detectors. The TRT was not used for tracking in 2010 data-taking.

3.3.3 Calorimeter System

The ATLAS calorimeter system, shown in Figure 3.4, is a combination of different sampling detectors that are required to contain and measure both electromagnetic (EM) and hadronic showers over a large $|\eta|$ region. The main ATLAS calorimeter system consists of an EM calorimeter and a hadronic calorimeter, each of which aims to contain and measure EM and hadronic showers, respectively. There are also two forward calorimeters, one at each end of the experiment, at larger η, which measure both EM and hadronic energy deposits. Different detector technology is used depending on the required accuracy for physics measurements and the radiation levels expected in different regions. The amount of material, in interaction lengths, is shown in Figure 3.5 for the different components of the ATLAS calorimeter system.

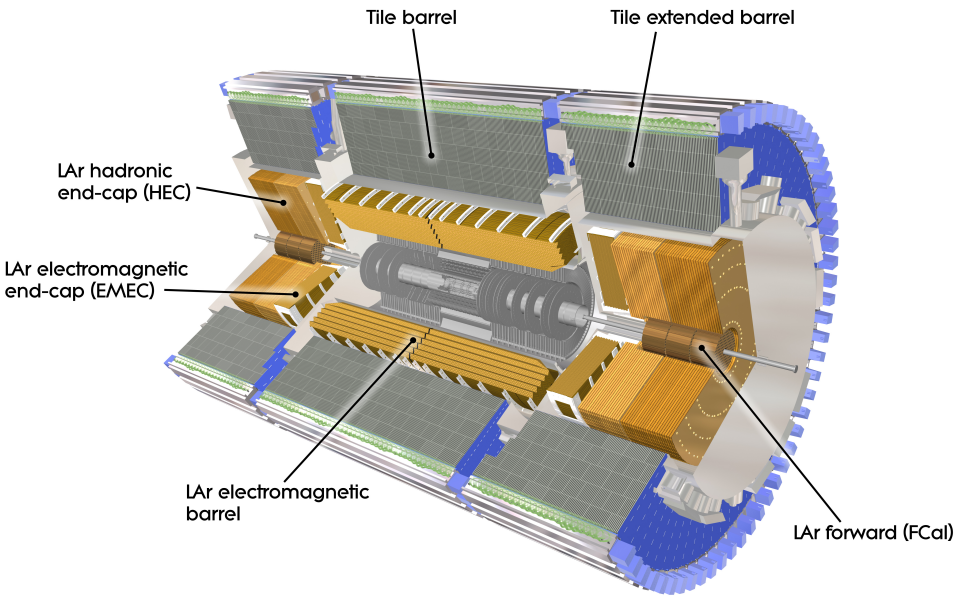

Figure 3.4: Schematic of the ATLAS calorimeter system. Figure from [34].

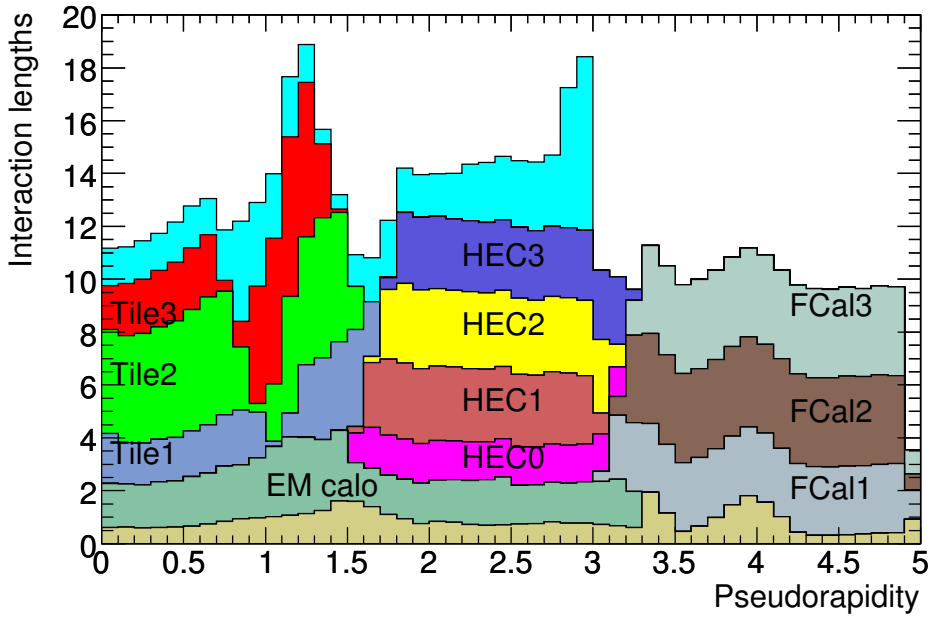

Figure 3.5: Amount of material, in interaction lengths, in front of the different calorimeters. The electromagnetic calorimeter is labelled "EM calo", the hadronic calorimeter is segmented into "Tile" and "HEC" layers, and the forward calorimeters is segmented with labels "FCal". The final layer shown outermost for $|\eta| < 3$ is the muon spectrometer. Figure from [34].

EM Calorimeter

The EM calorimeter is a sampling calorimeter with liquid argon (LAr) as the active material. It has complete azimuthal coverage for $|\eta| < 3.2$ and is used to give precision measurements of EM showers. Figure 3.4 shows the EM barrel and the EM end-cap, which have the pseudorapidity range $|\eta| < 1.475$ and $1.375 < |\eta| < 3.2$, respectively. In the precision region, which is the region that overlaps the inner detector ($|\eta| < 2.5$), there are three active layers and the detector is finely granulated to give a precise position measurement for the EM shower (used for photons). Outside of the precision region there are two active layers and the granularity is coarser. A presampler layer of LAr, which is in front of the first EM layer out to $|\eta| < 1.8$, is used to correct for energy lost before the EM calorimeter. The EM calorimeter has greater than 22 radiation lengths to attempt to fully contain any EM showers. The EM calorimeter cell information is calibrated to an EM scale using the decays of Z, W and $\mathcal{J}/\psi$ as presented in [35]. The uncertainty on the electron EM scale is $< 2\%$ for $|\eta| < 2.7$ and $2 - 3\%$ for $2.5 < |\eta| < 4.9$ for 10–1000 GeV energy electrons.

Hadronic Calorimeter

The hadronic calorimeter is situated behind the EM calorimeter covering the same η region, and is responsible for the measurement of hadronic showers. It consists of three tile calorimeters (one barrel and two extended barrels) in the region $|\eta| < 1.7$ and two hadronic end-caps (HEC) to extend the coverage to $|\eta| < 3.2$ as shown in Figure 3.4. The hadronic calorimeter is a sampling detector, and the different components use different technologies with the tile calorimeter using scintillating tiles as the active material and steel for the absorber, and the HECs using LAr as the active material and copper as the absorber.

The HEC has two wheels per end-cap, each with 32 wedged-shaped modules

and has a granulation of $\Delta\eta$ x $\Delta\phi$ = 0.1 x 0.1 in the region $|\eta| < 2.5$ and $\Delta\eta$ x $\Delta\phi$ = 0.2 x 0.2 in the region $2.5 < |\eta| < 3.2$. Each wheel has two different depth segments, resulting in four layers per end-cap.

The tile calorimeter has three components, one barrel and two extended barrels. The tile barrel and tile extended barrel cover the range $|\eta| < 1$ and $0.8 < |\eta| < 1.7$ respectively. These detectors comprise 64 modules which have a size of $\Delta\phi \approx 0.1$, resulting in a granularity of $\Delta\eta$ x $\Delta\phi$ = 0.1 x 0.1.

Forward Calorimeter

The forward calorimeter (FCal), shown in Figure 3.4, is responsible for measuring both the EM and hadronic showers in the region $3.2 < |\eta| < 4.9$. The FCal has three detecting layers, the first layer is made of copper that is optimised for EM measurements and the following two are tungsten layers used to measure hadronic energy deposits. All layers have LAr as the active material. The choice of materials and design is largely determined by the need to be radiation hard to withstand the high particle flux.

Calorimeter Objects

To help construct offline physics objects, such as photons, electrons, taus or jets, an algorithm to cluster calorimeter readout cells is used. The aim of clustering is to reconstruct the 3D EM or hadronic showers from the calorimeter cells. Two clustering algorithms are used, the "sliding window" algorithm for photon, electron or tau identification, and the "topological" algorithm for jets. The sliding window algorithm combines cell information from cells within a fixed size rectangular window in η and ϕ. Topological clusters, or "topocluster", are formed from a cluster seed, which is a cell with $|E|/\sigma_{noise} > 4$, where σ_{noise} is the expected noise in the calorimeter from the readout electronics and "pile-up" contributions.

The cluster is then extended by including all cells next to it with $|E|/\sigma_{noise} > 2$. An additional layer of cells with $|E|/\sigma_{noise} > 0$ are included. The advantage of using this clustering rather than towers (groups of cells at fixed $\Delta\eta$ and $\Delta\phi$) is to improve noise suppression. More information regarding topoclusters and sliding window clustering, and their performance, can be found in [35, 36].

3.3.4 Muon Detectors

Furthest from the interaction point are the muon detectors. The muon detectors measure the hits from muons which are bent by the magnetic fields from the barrel toroid and end-cap toroids, and a combination of both in the region between. The muon system has separate dedicated detectors for both precision position measurements and for triggering on muons.

For the precision measurement, Monitored Drift Tubes (MDT) are used in the pseudorapidity range $|\eta| < 2.7$, with the higher granularity Cathode Strip Chambers (CSC) used in the more forward region of $2 < |\eta| < 2.7$ in the innermost layer. The muon triggering system consists of Resistive Plate Chambers (RPC) in the barrel region and Thin Gap Chambers (TGC) in the end-cap region. The muon triggering system covers the region of $|\eta| < 2.4$.

3.3.5 Trigger and Data Acquisition

The event rate from the LHC is ≈ 1 GHz, but only $\mathcal{O}(200$ Hz) will be recorded to disk. The ATLAS trigger and data acquisition system (TDAQ) reduces the initial event rate by select the most interesting events containing high p_{T} objects. TDAQ is split into subsystems that are approximately associated with the sub-detectors previously described. The three different trigger levels are level 1 (L1), level 2 (L2), and event filter (EF). The L2 and EF triggers are called the higher level triggers (HLT). The trigger levels are applied in series, with each level refining the

decision and adding additional requirements. L1 is required to make a decision in less than 2.5 μs and reduce the rate to 75 kHz. If the event has passed a L1 trigger, it then goes through the L2 and EF trigger which have more information about the event and reduce the rate to 200Hz. While the trigger is deciding whether the event should be kept, the data acquisition system is buffering the event information.

L1 triggers select interesting objects, such as high p_T jets, electrons, muons, photons, taus or large missing E_T, which are indicative of interesting physics processes. The main three detector systems that trigger events at the L1 level are the RPC and TGC, which trigger on muons, the calorimeter with reduced granularity, which triggers on jets, electrons, muons, photons, or large missing E_T, and the Minimum Bias triggers that trigger on minimal energy and are used to select an unbiased sample of events. The results from the muon, calorimeter and minimum bias triggers are passed to the Central Trigger Processors (CTP). The CTP then applies a trigger menu, which is a list of triggers, their thresholds and prescales. By applying a prescale, p, to a trigger, only p^{-1} of the events that fired the trigger will be passed to L2. The purpose of the prescale is to reduce the rate of less interesting or high rate processes and also to keep the overall rate constant as the instantaneous luminosity changes.

The L1 trigger passes the region of interest, RoI, (this is a $\eta\phi$ region near the triggered object) to the HLT. The L2 triggers have access to the information around the L1 RoI, but cannot attempt a full event reconstruction in the 40 ms given to make the initial decision. The extra information at L2 is used to make tighter cuts in order to reduce the rate to 3.5 kHz. The EF triggers have approximately four seconds to make a decision. This is long enough to do longer offline analysis procedures using the full event reconstruction, which help to reduce the overall rate written to disk to 200 Hz.

The important triggers for this thesis are the calorimeter trigger (specifically the jet trigger) and the minimum bias trigger, which will be discussed below. Additional information about the triggers and their performance can be found in [37].

Minimum Bias Triggers

The minimum bias (Min Bias) triggers aim to provide events that are minimally biased towards any particular physics process. This is achieved by having a set of minimum bias trigger scintillator counters (MBTS) at the front of the calorimeter end-caps ($2 < |\eta| < 3.8$). The MBTS are fired by any low energy particle within their acceptance. The result is a very high rate from the MBTS, such that it is heavily prescaled for all but the lowest luminosity runs.

L1 Calorimeter

The L1 calorimeter trigger (L1Calo) is the trigger system concerned with both the EM calorimeter and the hadronic calorimeter. The EM and hadronic calorimeter readout cells are merged into trigger towers of $\Delta\eta \times \Delta\phi = 0.1 \times 0.1$ for the precision region and increasing size for regions of higher pseudorapidity. Trigger towers are used to define jet, electron, photon and tau trigger objects.

Jet Triggers

L1 jet trigger objects are found by first defining jet elements from 2x2 trigger towers in both the EM and hadronic calorimeters. In the central precision region the jet elements cover a region of $\Delta\eta \times \Delta\phi = 0.2 \times 0.2$. A sliding window algorithm is used to find the L1 jet objects. The algorithm can be set to have a window of either 2×3, 3×3 or 4×4 jet elements for the jet finding. The algorithm looks over the jet elements to find local maxima in transverse energy, E_{T}, and defines

a jet if the E_{T} is greater than a given threshold. The L1 jet triggers are named L1_JX where X is the EM energy threshold for the jet object.

Once the L1 jets are found, the RoIs, corresponding to the position of the L1 jets, are passed to the HLT, and act as seeds. The L2 jet trigger can access the coarse calorimeter information from around the L1 jet RoI. This information is then passed into a seeded cone jet algorithm (see Section 4.2.2), which is a basic and fast jet finder which uses a jet radius R of 0.4, and which is restricted to three iterations. The L2 can access finer calorimeter information and produce cone-like jets. The hadronic components of the jet at L2 are calibrated, which is important as the detector has a lower response to hadronic energy deposits than the EM energy deposits. The EF jet triggers were not used in the 2010 data-taking. The definition in 2011 is in Section 4.2.2.

3.4 Jets in ATLAS

The jet definition within ATLAS uses the anti-k_t algorithm, which is described in Section 2.3. This algorithm groups related energy deposits in the ATLAS calorimeters. Different input objects can be used with the anti-k_t algorithm, such as cells, towers and topoclusters and these objects can be calibrated to different energy scales. In this analysis, unless otherwise stated, the jets are defined using the anti-k_t algorithm with a distance parameter of 0.6 running over topocluster at EM scale, where topoclusters and EM scale are defined in Section 3.3.3.

Jet Energy Scale (JES)

The jet response needs to be calibrated to take into account both detector and physics responses such as dead material, particle being bent into and out of the jet, and noise threshold variation. Also, jets are found using EM-scale topoclusters and need to be calibrated due to the non-compensation of the hadronic

calorimeter which has a lower detector response to hadrons than to EM deposits. An EM+JES calibration was determined as a function of the jet p_{T} and rapidity to account for these effects.

The EM+JES calibration was done in three consecutive corrections. The first was a pile-up offset correction designed to subtract energy contributions due to additional pp interactions. The correction is presented in [38], where the average energy in towers is considered as a function of η, the number of primary vertices and the bunch spacing. The second correction was the vertex correction, which defined the origin of the jets to be the primary vertex. This correction changes the direction and p_{T} of the jet, but not its energy, and it improves the angular resolution of the jet. The original uncorrected η is defined as η_{det}. The final correction is the jet energy scale (JES) correction.

The JES correction uses fully simulated MC, "reco", jets and jets at hadron level, "truth" jets, to obtain correction factors as a function of jet energy and jet rapidity. The response of the calorimeter to jets can be defined using these fully simulated MC samples as

$$\mathcal{R}(\eta) = \frac{{p_{\mathrm{T}}}^{reco}(\eta)}{{p_{\mathrm{T}}}^{truth}(\eta)} \tag{3.7}$$

where ${p_{\mathrm{T}}}^{reco}$ is the p_{T} of the MC jet after full simulation of the detector, and ${p_{\mathrm{T}}}^{truth}$ is the p_{T} of the MC jet at hadron level. The truth and reco jets are matched using a ΔR requirement of 0.3. The correction factors are calculated as a function of the jet's detector η opposed to the vertex corrected η, as they represent calibrations for different detectors, and also as a function of the energy, as the detector responds to energy. Figure 3.6 shows the jet responses, at EM scale, as a function of detector $|\eta|$ for different jet energies. From the comparison between fully simulated MC jets and truth jets, a small correction on the jet rapidity is calculated. This is due to part of jets falling into regions with lower response, giving a η shift towards the higher responding areas. The original

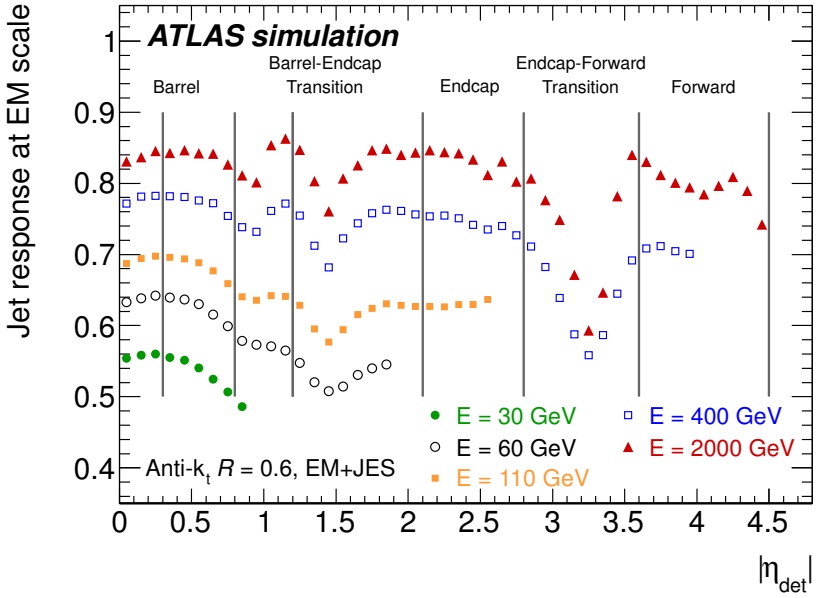

Figure 3.6: PYTHIA simulated jet EM-scale response as a function of reconstructed jet detector η for different jet energies [39]. The different evaluated regions are shown, as well as their relation to the detector geometry.

derivation of these factors can be found in [38–40].

Jet Energy Scale Uncertainty

The EM+JES method of calibration is based primarily on the ability of the MC to simulate correctly the ATLAS detector and also to model the physics effects such as energy flow out of the jet. In-situ methods are used to validate the JES calibration and assign an uncertainty. The JES uncertainty is derived from in-situ data measurements and also by varying MC settings. It is determined by combining many different components in quadrature. These are: the non-closure of the EM+JES on fully simulated MC jets; calorimeter response to isolated hadrons using test-beam information and in-situ methods; additional detector material; noise thresholds; differences compared to other MCs; uncertainties due to pile-up, and p_{T} balance of dijet events.

Figure 3.7 shows the fractional JES uncertainty for jets with $2.1 \leq |\eta| \leq 2.8$

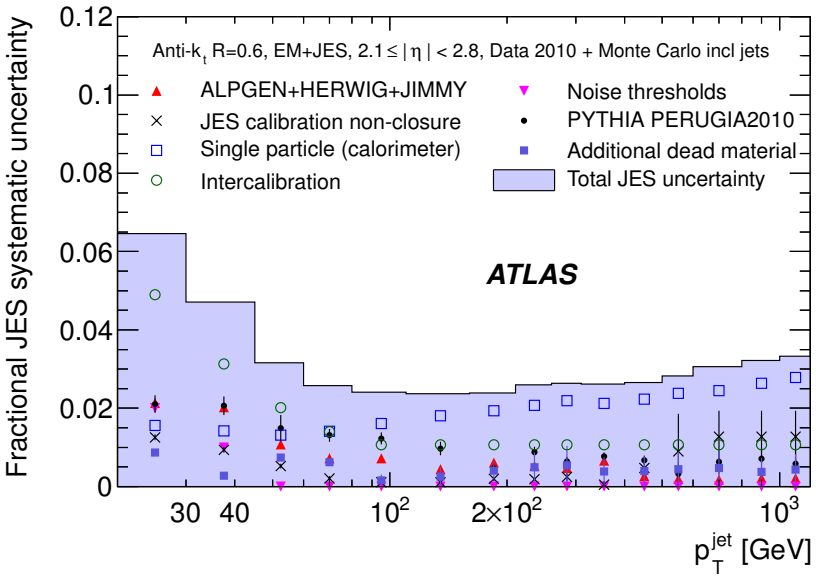

Figure 3.7: Fractional JES uncertainty for jets with $2.1 \leq |\eta| \leq 2.8$ as a function of the jet p_{T} [39].

as a function of the jet p_{T}. The dominant systematic at high p_{T} is the single particle response which comes from test-beam single pion information and the calorimeter response for a single hadron. At low p_{T}, dijet balance (labeled as "intercalibration") is the most significant uncertainty. Dijet balance is an in-situ method of extending the uncertainty in the central region to other regions of the detector, and will be discussed in more detail in Chapter 5.

Jet Energy Resolution

The jet energy resolution (JER) is a measure of the expected range of measured jet p_{T} compared to the original object. Some causes of the fluctuations in the measurement of a jet p_{T} are different hadron/EM contributions, non-average amount of additional energy from pile-up, and statistical fluctuations in the sampling technique across multiple calorimeter layers. The JER was determined using the bi-sector method and the p_{T} balance of dijet events described in [41, 42].

Jet Cleaning

Jets produced in an event need to be discriminated from "bad" background jets that come from signal spikes in cells within the HEC and EM noise in the calorimeter, cosmic rays or non-collision background. Table 3.2 shows the loose and medium cleaning requirements used to remove the bad jets where

- The jet charge fraction, $\mathbf{f_{CH}}$, is the ratio of the sum of the p_{T} of tracks associated to the jet to the calibrated jet p_{T};
- $\mathbf{f_{EM}}$ is the fraction of the jet EM scale energy that comes from EM clusters;
- $\mathbf{f_{HEC}}$ is the fraction of the jet energy that was measured in the HEC;
- The LAr quality, $\mathbf{Q_{LAr}}$, is the fraction of the jet energy coming from LAr cells with poor signal shape quality;
- The HEC quality, $\mathbf{Q_{HEC}}$, is the fraction of the jet energy coming from HEC cells with poor signal shape quality;
- **neg. E** is the sum of the negative energy cells in the jet, which is indicative of noise fluctuations;
- Jet time, $\mathbf{t}$, is the mean time between the cells in the jet and the event time;
- $\mathbf{f_{max}}$ is the maximum energy fraction in one calorimeter layer.

Jets coming from HEC spikes have most of the energy coming from a single noisy calorimeter cell, and so a $\mathrm{f_{HEC}}$ requirement is applied to ensure energy deposits outside the HEC form a significant part of the total energy. Fake jets coming from EM coherent noise are removed by cutting on the fraction of EM energy. Finally, jets from non-collision backgrounds and cosmic rays are removed using a combination of timing and energy layer requirements.

	Loose	Medium
HEC spikes	$f_{HEC} > 0.5$ & $\|Q_{HEC}\| > 0.5$ or $\|\text{neg.E}\| > 60$ GeV	$f_{HEC} > 1 - \|Q_{HEC}\|$
EM coherent noise	$f_{EM} > 0.95$ & $\|Q_{LAr}\| > 0.8$ & $\|\eta\| < 2.8$	$f_{EM} > 0.9$ & $\|Q_{LAr}\| > 0.8$ & $\|\eta\| < 2.8$
Non-collision background & cosmics	$\|t\| > 25$ ns or $f_{EM} < 0.05$ & $f_{CH} < 0.05$ & $\|\eta\| < 2$ or $f_{EM} < 0.05$ & $\|\eta\| > 2$ or $f_{max} > 0.99$ & $\|\eta\| < 2$	$\|t\| > 10$ ns or $f_{EM} < 0.05$ & $f_{CH} < 0.1$ & $\|\eta\| < 2$ or $f_{EM} > 0.95$ & $f_{CH} < 0.05$ & $\|\eta\| < 2$

Table 3.2: Loose and Medium jet cleaning definitions where Medium also includes the Loose definitions.

The loose cleaning requirements are defined to have an efficiency of greater than 99% for good jets, but a fraction of bad jets still remain. Whilst the medium cleaning requirements remove a higher proportion of bad jets, they have inefficiencies at low p_T for good jets.

While the bad jets do not come from energy deposits from the interaction, there is a subset of jets, called "ugly" jets, which are energy deposits from the interaction which have been badly measured. Ugly jets are often found in regions between detectors, "cracks" regions, where the performance of the detectors are not optimal. Two selection criteria are applied to remove ugly jets. First, the jet energy which falls into the transition between the barrel and the end-cap is required to be less that half the total jet energy. Second, the fraction of energy that comes from bad cells inside the jet is required to be less than half of the total jet energy.

Chapter 4

High Level Trigger Calorimeter Monitoring

The calorimeter high-level trigger (HLTCalo) is used to trigger on physics objects that deposit their energy in either the electromagnetic or hadronic calorimeter. As described in Section 3.3.3, the calorimeter is segmented into cells. These cells are clustered together and can be combined with inner detector tracks to define physics objects such as electrons, photons, taus, and jets.

The HLTCalo is monitored to check the performance and consistency of the triggers. This is achieved by monitoring the individual cells in the calorimeters and also by comparing the different L2 and EF triggered physics objects to the corresponding offline object. Flags are defined for each monitoring distribution, where a green flag represents the distribution is consistent with the expected distribution, and yellow and red represent a deviation from the expected distribution. When the flag is red or yellow the distribution is studied further via a web based graphical user interface to find the reason, and if necessary the associated data can then be excluded from physics analysis.

In this chapter, work done by the author on improvements to the current cell monitoring which expose hot cells, and the addition of monitoring of calorimeter

objects are discussed.

4.1 Cells

The overall HLTCalo monitoring is done on a cell by cell basis. This monitoring consists of distributions showing the number of active cells in the LAr and Tile calorimeters, the number of problematic cells and the position of these cells in the LAr and Tile calorimeters, and also the difference in cell energy between the trigger levels and offline levels.

The number of cells in the LAr and Tile calorimeters is an example of a monitoring plot that is very stable and should only change when a hot cell is masked or taken offline, allowing very tight flag definitions. Monitoring plots, such as the percentage difference in energy in the trigger and offline cells, vary significantly ($\approx 15\%$) with different running conditions, so either looser or no flag definitions are set.

The average transverse energy per cell in $\eta\phi$ distribution is important in identifying hot spots where one cell records artificially high energy in every event. Hot cells can be caused from electronic problems within the cells. Figure 4.1 shows an example of a hot spot found using the offline cell monitoring in run 201191. This resulted in the cell being masked.

4.2 Calorimeter Objects

The HLTCalo is also monitored by comparing calorimeter triggered objects (electrons, photons and jets) to the offline objects. A ΔR selection is made to match the triggered objects to the offline objects. An minimum E_{T} is required on the offline objects, which is the same as required by the analysis selection.

Figure 4.1: Average E_{T} per $\eta\phi$ bin in run 201191. A hot region is observed at $\eta = 2.5$ $\phi = 1$.

4.2.1 Electrons and Photons

The EM calorimeter component of the HLTCalo is monitored by using physics objects that are reconstructed using EM energy deposits from electrons and photons. There are differences between the L2 and EF level EM cluster finding due to the time constraints on the L2 trigger. The L2 EM clusters are found using only the second EM calorimeter layer, in which the highest energy cell is used as the cluster seed. From this cluster seed, the cluster position is formed using the cell-energy weighted η and ϕ from a grid of $\Delta\eta \times \Delta\phi = 0.075 \times 0.075$ around the seed, and the cluster energy is calculated by summing over the energy of the cells. Conversely, the EF EM clusters use a sliding-window cluster algorithm using the calorimeter towers. This reduces the effect of the hot cells, as these will be smeared by the surrounding regular cells which will not have energy deposits. The offline clusters are also found using a sliding-window algorithm,

but they have full offline cell information.

EM cluster matching

Matching the offline and trigger objects is done using ΔR. Figure 4.2 shows the ΔR distribution between the offline and all L2 EM clusters. Two peaks can be seen in (a), one at $\Delta R = 0$ which corresponds to good matching. Events often have two objects that will be back-to-back in $\Delta\phi$, which corresponds to the peak at $\Delta R \approx \pi$. The peak at $\Delta R = 0$ shown in the expanded view (b), which shows a minimum in the range ΔR from 0.03 to 0.1. There is also a peak at $\Delta R = 0.15$ which is likely due to the decay of a π_0 meson.

Figure 4.3 shows the ΔR distribution between the offline and all EF EM clusters. As observed for the L2 ΔR distribution, there are two peaks; one at $\Delta R = 0$ and one at $\Delta R \approx \pi$. The minimum observed in (b) is in the range ΔR from 0.02 to 0.1.

A ΔR matching criteria of 0.035 is used between the offline and both L2 and EF triggers as this selects the majority of the correctly matched clusters and is also the distance from the centre to the edge of the L2 cluster. In addition, the offline cluster is required to have $E_{\mathrm{T}} > 10$ GeV.

Monitored Distributions

The monitoring plots shown in Figures 4.4 – 4.6 are from run 190644 in the 2011 data-taking. Figure 4.4 shows the distribution of the offline EM cluster E_{T} versus that of (a) a L2 and (b) a EF EM cluster E_{T}. This is useful in checking the linearity of the trigger EM clusters to the offline. The L2 EM cluster E_{T} shows linearity to the offline EM cluster E_{T}, and the majority of events fall on a straight line where the E_{T} of the offline and L2 are the same. There is a significant band either side of this straight line, with more above the line. This corresponds to

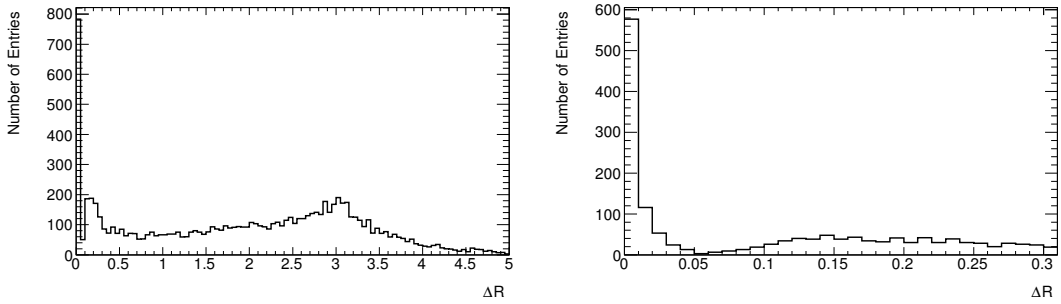

(a) (b)

Figure 4.2: ΔR distribution between the offline EM cluster and all L2 clusters in the event, shown within the range (a) $\Delta R = 0 - 5$ and (b) $\Delta R = 0 - 0.3$ from run 186049.

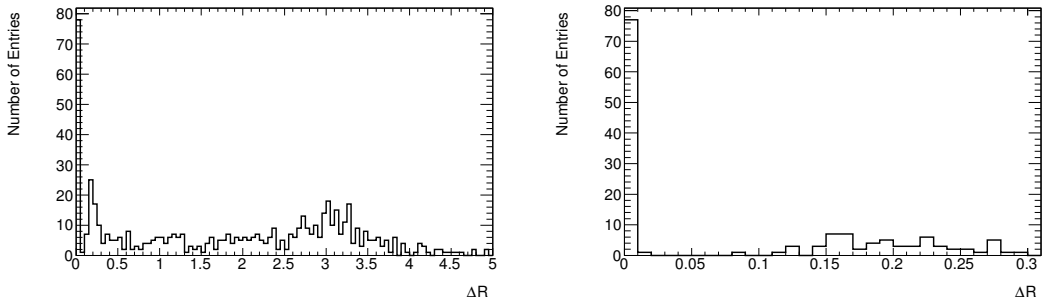

(a) (b)

Figure 4.3: ΔR distribution between the offline EM cluster and all EF clusters in the event, shown within the range (a) $\Delta R = 0 - 5$ and (b) $\Delta R = 0 - 0.3$ from run 186049.

a larger offline E_{T} than L2 EM cluster E_{T}. The EF EM cluster E_{T} also shows linearity, and again most of events fall on a straight line corresponding to the offline EF clusters having the same E_{T}. The band around the events falling on the straight line is significantly smaller than for the L2 EM clusters.

Figure 4.5 shows the distribution of E_{T} fraction,

$$f(E_{\mathrm{T}})_{Trigger} = \frac{E_{\mathrm{T}}(\text{Triggered EM cluster})}{E_{\mathrm{T}}(\text{Offline EM cluster})}, \tag{4.1}$$

as a function of η for (a) the L2 EM clusters and (b) the EF EM clusters. The E_{T} fraction for the L2 EM clusters is centred around one, with most events within 5%. The EF EM clusters' E_{T} fraction is also centred around one, but with tighter range. In both distributions there is a region at $|\eta| = 1.5$ where the fluctuations in the ratio from unity are larger. This is due to the EM deposit falling into the crack region between the EM calorimeter barrel and the EM barrel end-cap. There is an improvement in the EF due to the additional calibration done at EF level.

Figure 4.6 shows the distribution of the E_{T} resolution,

$$\sigma(E_{\mathrm{T}}) = \frac{E_{\mathrm{T}}(\text{Triggered EM cluster}) - E_{\mathrm{T}}(\text{Offline EM cluster})}{E_{\mathrm{T}}(\text{Offline EM cluster})}, \tag{4.2}$$

for (a) L2 EM clusters and (b) EF EM clusters. Both distributions have a mean $\sigma(E_{\mathrm{T}})$ of $< 1\%$. The L2 EM cluster $\sigma(E_{\mathrm{T}})$ distribution has a larger spread than that for the EF.

All the monitoring distributions are susceptible to changes in calibration or the cluster sizes. The monitoring flags can be set to compare the mean of the distribution to the expected value. The distributions in Figures 4.5 and 4.6 have flags set based on the mean of the E_{T} fraction and $\sigma(E_{\mathrm{T}})$, respectively. If these show sizable differences from the expected mean, the distribution will be yellow or red flagged automatically. Figure 4.4 can then be used to study the reason for the differences.

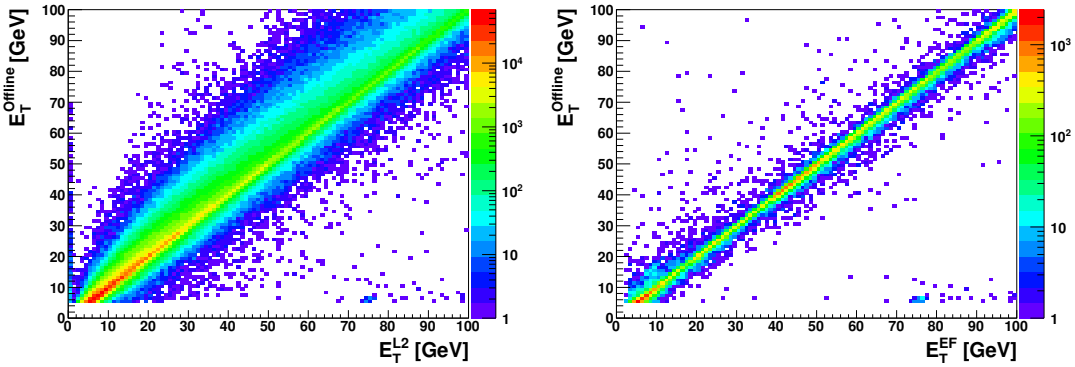

(a) (b)

Figure 4.4: E_{T} of the offline EM cluster versus the E_{T} of the closest matched (a) L2 and (b) EF EM cluster from run 190644.

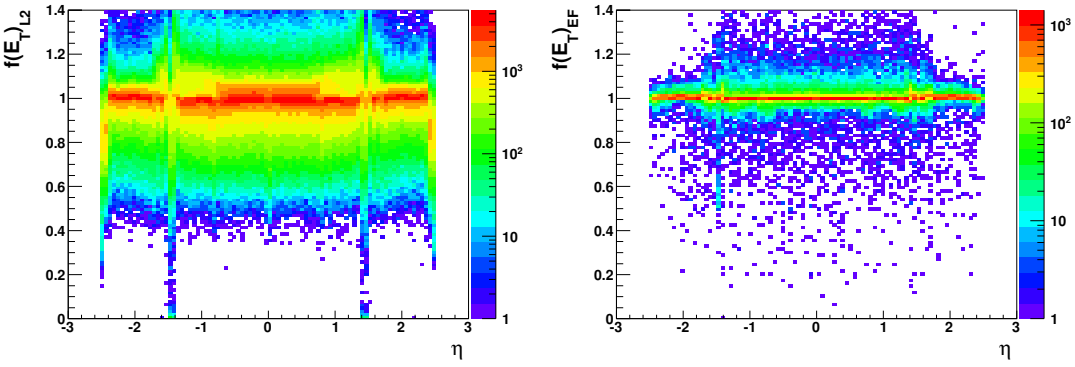

(a) (b)

Figure 4.5: E_{T} fraction of (a) the L2 and (b) the EF EM cluster to the offline EM cluster E_{T} as a function of η from run 190644.

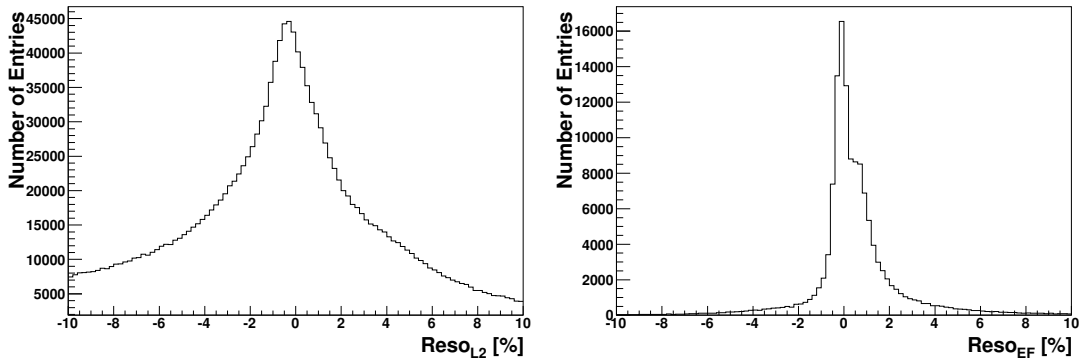

(a) (b)

Figure 4.6: Distribution of the relative difference between the E_{T} of the (a) L2 and (b) EF EM cluster, and the offline EM cluster E_{T} from run 190644.

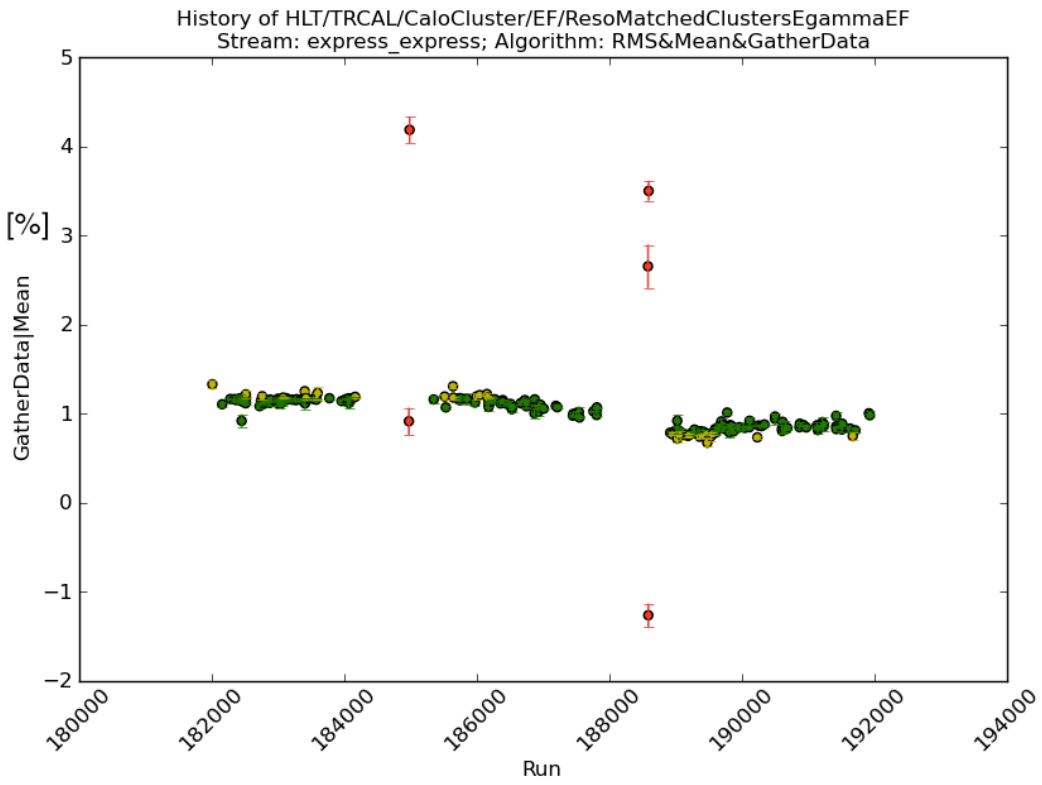

Figure 4.7: Mean EF EM cluster $\sigma(E_{\mathrm{T}})$ as a function of run number.

Figure 4.7 shows the history of the mean of $\sigma(E_{\mathrm{T}})$ for EF EM clusters. The colours of the points show the flag that was set for these runs. Flags were assigned for a given run depending on the difference of the mean to a standard mean of 0.975%. The run is flagged green if the difference is less than 0.2%, yellow if between $0.2\% - 0.4\%$ or red if greater than 0.4%. These flag values were tuned using the initial runs in the first data taking region. Most of the runs are set as green or yellow, with only a few set as red. The red flagged runs are those where there is no stable beam and some sections of the LAr calorimeter were not online during the run. The slight downward trend of the mean is due to change in the levels of pile-up and software changes.

4.2.2 Jets

Jets are used to monitor both the EM and hadronic calorimeter. These jets consist of grouping of EM and hadronic clusters. The anti-k_t jet-finding algorithm, which is described in Section 2.3, is used with an $R = 0.4$ for the offline jets. Only offline jets with a $p_{\mathrm{T}} > 20$ GeV are considered, which is the same as the analysis selection. The L2 jet-finding is done using a cone algorithm. The cone algorithm is seeded using a L1 RoI, and all deposits within the radius of the cone are combined, and a new cone centre is defined using the energy weighted position of the constituents. With the new cone defined, any new deposits within the radius are again combined, and a new cone centre is defined. This continues until the cone centre does not change.

The anti-k_t jet-finding algorithm is used for the EF jets. While using this, the EF jets run over clusters that are close to the RoI. In the 2012 data taking, calibration is applied to the EF jets to account for the non-compensating calorimeters.

Jet matching

The trigger jets are matched to offline jets using ΔR to allow them to be compared. Figure 4.8 shows the ΔR between the offline jets and all L2 jets in the event. As observed in the EM clusters, in (a) there are two peaks; one at $\Delta\mathrm{R} \approx 0$ and one at $\Delta\mathrm{R} \approx \pi$. The differences from the EM clusters are best seen in (b), the first peak is not quite at zero. This is due to the ϕ resolution of the jets shifting the $\Delta\phi$ away from zero. Figure 4.9 shows the ΔR between the offline jets and all EF jets in the event. The distributions are similar to the L2 jet ΔR distributions, with a peak just above zero, and one at $\Delta\mathrm{R} \approx \pi$.

A matching selection of $\Delta\mathrm{R} < 0.4$ is used for both the L2 and EF jets. This corresponds to the R value used in the jet-finding for the trigger and offline jets.

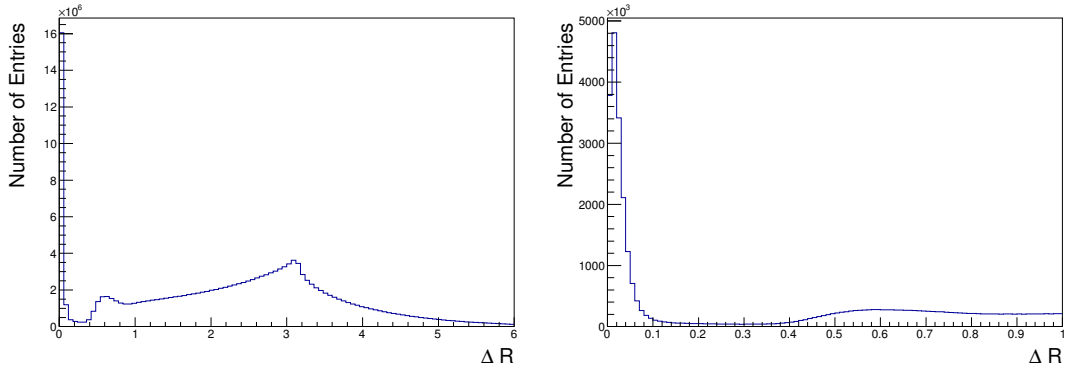

(a) (b)

Figure 4.8: ΔR distribution between the offline jet and all L2 jets in the event, shown within the range (a) $\Delta R = 0 - 6$ and (b) $\Delta R = 0 - 1$ from run 203335.

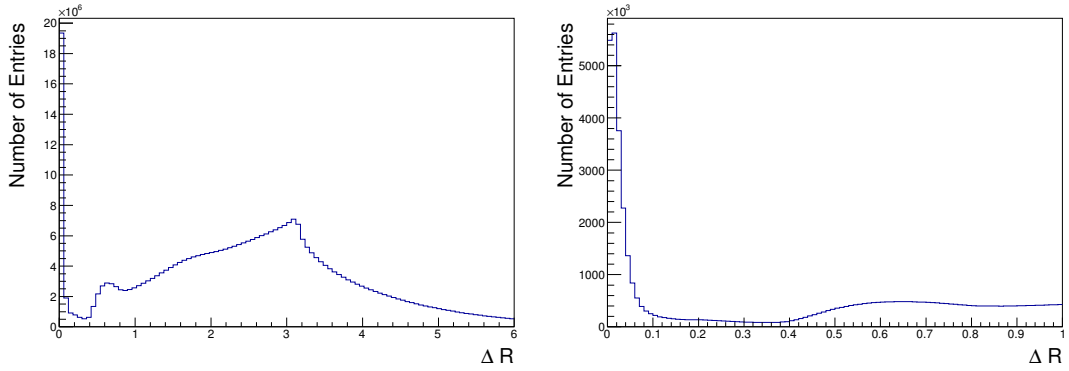

(a) (b)

Figure 4.9: ΔR distribution between the offline jet and all EF jets in the event, shown within the range (a) $\Delta R = 0 - 6$ and (b) $\Delta R = 0 - 1$ from run 203335.

Monitored Distributions

The jet monitoring uses the same distributions as the monitoring of the EM clusters. The monitoring distributions shown in Figures 4.10 - 4.12 are from run 203335, which was taken in 2012. Figure 4.10 shows the E_{T} of the offline jet versus the E_{T} of (a) the L2 and (b) the EF jets. The E_{T} comparison is used to check the linearity of the trigger jet E_{T} to that of the offline jet. The L2 trigger E_{T} shows linearity to the offline jet E_{T}, with the trigger jets E_{T} being $\approx 60\%$ of the offline jet E_{T}. This is due to the different energy scales of the jets; whilst the offline are fully calibrated, the L2 trigger jets are at EM scale. The E_{T} of the EF jets agrees well with the offline jets. This improvement is expected due to the calibration done on the EF jets. Both the EF jets and the L2 jets have good linearity to the offline jet E_{T}.

Figure 4.11 shows the E_{T} fraction (Equation 4.1) as a function of jet η for (a) the L2 jets and (b) the EF jets. The L2 jets have a mean E_{T} fraction of ≈ 0.7, whilst the EF jets have a mean E_{T} fraction closer to one. This is again explained due to the jet energy scale of the trigger jets. In both distributions, underlying differences between the trigger jets and offline jets can be seen in different regions of the detector. The jumps in $f(E_{\mathrm{T}})$ at $|\eta| \approx 1.2$ are due to the transition between the barrel and the tile calorimeters, where large fluctuations in jet p_{T} are anticipated.

Figure 4.12 shows the E_{T} resolution of (a) the L2 jets and (b) the EF jets. As seen in previous figures, the L2 jets are $\approx 70\%$ of the offline jets, due to the difference in calibration. The mean of the E_{T} resolution of the EF jets is close to zero. Problems in the detector should show up in the plot as a change in the mean.

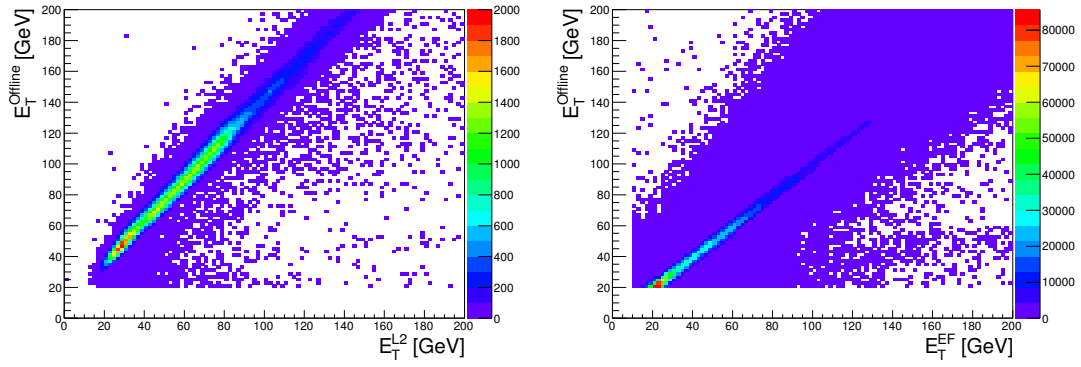

(a) (b)

Figure 4.10: E_T of the offline jet versus the E_T of the matched (a) L2 and (b) EF jet from run 203335.

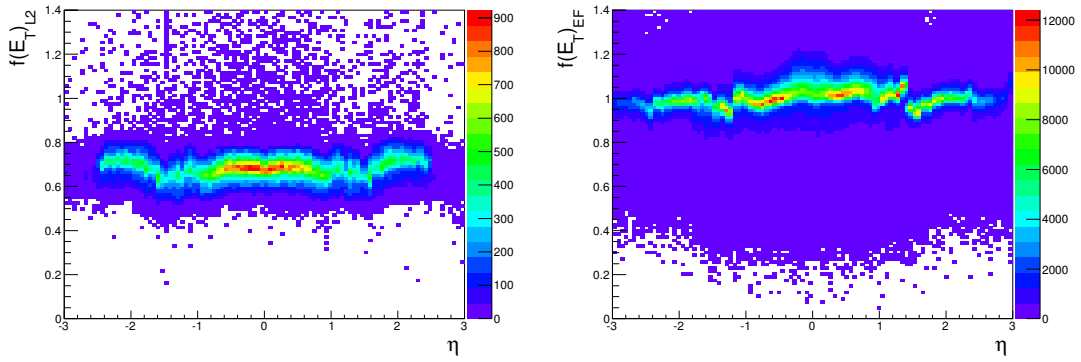

(a) (b)

Figure 4.11: E_T fraction of the (a) L2 and (b) EF jets to the offline jet E_T as a function of η from run 203335.

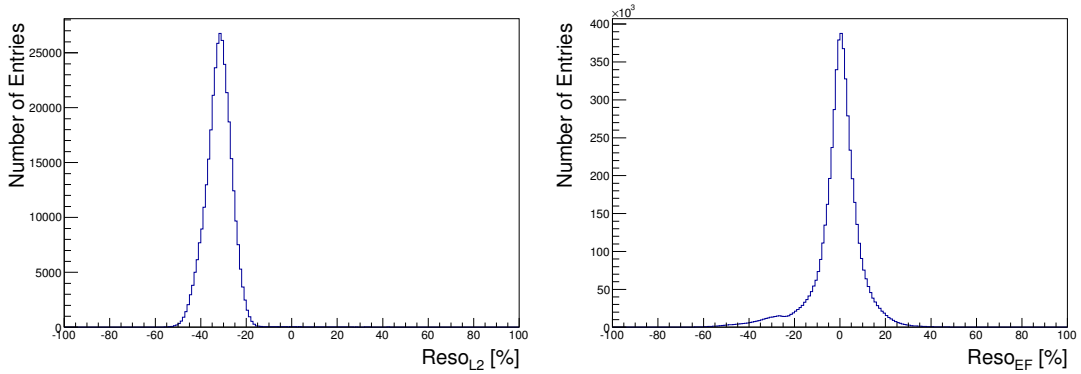

(a) (b)

Figure 4.12: E_T resolution of (a) the L2 jets and (b) the EF jets from run 203335.

4.3 Summary

Updates to the HLT cell monitoring and the addition of offline monitoring of the HLTCalo using physics objects such as jets are presented. Cells have been masked to reduce the effect from noisy cells, and the EM and jet triggers have been monitored and observed to have good stability. Data where this have not been the case have not been used for physics analyses.

Chapter 5

In-Situ Validation of ATLAS Jet Reconstruction and Calibration

The response of the calorimeter to jets is found using fully simulated MC, comparing reconstructed jets to truth jets. These correction factors are known as the JES calibration and are described in Section 3.4. To obtain the uncertainty on the JES, various MC and in-situ validations are done. This chapter describes one such in-situ method, p_{T} balancing of dijet events.

In the central region ($0 < |\eta| < 0.8$), the JES and its uncertainty are well known due to test-beam data and good knowledge of the detector geometry. The p_{T} balancing of dijet events can extend the determination of the uncertainty into the end-cap ($0.8 < |\eta| < 2.8$) and forward ($2.8 < |\eta| < 4.5$) regions. The jets in the central region, which are well understood, are used to obtain relative JES uncertainties in the end-cap and forward regions.

This method of extrapolating the uncertainty outside the central region is achieved by using the p_{T} balance of dijet events to derive a relative jet response between the two jets. In a dijet topology, it is expected that both jets should have the same transverse momentum, assuming that the jets arise from a $2 \to 2$ partonic scatter. Using this assumption, the p_{T} imbalance can be expressed using

the asymmetry $\mathcal{A}$ defined as

$$\mathcal{A} = \frac{{p_{\mathrm{T}}}^1 - {p_{\mathrm{T}}}^2}{{p_{\mathrm{T}}}^{ave}}, \tag{5.1}$$

where ${p_{\mathrm{T}}}^1$ and ${p_{\mathrm{T}}}^2$ are the transverse momentum of the two leading jets, and ${p_{\mathrm{T}}}^{ave}$ is the average p_{T} of the two jets. For imperfectly measured jets, the asymmetry would not be unity and a relative calorimeter response to a jet can be constructed using the asymmetry as,

$$\frac{{p_{\mathrm{T}}}^1}{{p_{\mathrm{T}}}^2} = \frac{2 + \langle \mathcal{A} \rangle}{2 - \langle \mathcal{A} \rangle}. \tag{5.2}$$

The assumption made is that the event comes from a $2 \rightarrow 2$ partonic scatter, without an additional hard QCD emission in the interaction. This assumption can be wrong if there are more than two hard jets, or if there is a large amount of soft quark or gluon emission outside the jets. To reduce these effects, a selection is placed on the third jet p_{T} of ${p_{\mathrm{T}}}^3 < 0.25 \times {p_{\mathrm{T}}}^{ave}$ and also requiring the leading jets to be back-to-back in azimuth with a selection of $\Delta\phi > 2.6$. These selections were optimised to reduce the bias from non $2 \rightarrow 2$ topologies, while retaining high statistics.

5.1 In-Situ Validation of Jet Calibration

Standard Method for Dijet Balance

In the standard p_{T} balance method, one of the jets is required to be in a reference region where the jet is well calibrated and understood. This jet is defined as the "reference" jet. The other jet is the "probe" jet, and is used to probe the regions outside the reference region. Given these definitions, Equations 5.1 and 5.2 become,

$$\mathcal{A} = \frac{{p_{\mathrm{T}}}^{probe} - {p_{\mathrm{T}}}^{ref}}{{p_{\mathrm{T}}}^{ave}} \qquad \text{and} \qquad \frac{{p_{\mathrm{T}}}^{\mathrm{probe}}}{{p_{\mathrm{T}}}^{\mathrm{ref}}} = \frac{2 + \mathcal{A}}{2 - \mathcal{A}} = \frac{1}{\mathrm{c}}, \tag{5.3}$$

where c is the response ratio of the probe jet to the reference jet.

Using this standard method, an asymmetry , $\mathcal{A}_{ik}$, is obtained in bins of η and ϕ. The ratio of responses, or inter-calibration factor, for the i-th η and k-th ${p_{\mathrm{T}}}^{ave}$ bin is defined as

$$\mathrm{c_{ik}} = \frac{2 - \langle \mathcal{A}_{ik} \rangle}{2 + \langle \mathcal{A}_{ik} \rangle}, \tag{5.4}$$

where $\langle \mathcal{A}_{ik} \rangle$ is the mean value of the asymmetry distribution in the bin.

Matrix Method for Dijet Balance

The matrix method differs from the standard method by not requiring a specific reference region. Instead of a probe and reference jet, there is a "left" jet and a "right" jet, where $\eta^{\mathrm{left}} < \eta^{\mathrm{right}}$. As a result Equations 5.1 and 5.2 become,

$$\mathcal{A} = \frac{{p_{\mathrm{T}}}^{\mathrm{left}} - {p_{\mathrm{T}}}^{\mathrm{right}}}{{p_{\mathrm{T}}}^{ave}} \tag{5.5}$$

and

$$\frac{{p_{\mathrm{T}}}^{\mathrm{left}}}{{p_{\mathrm{T}}}^{\mathrm{right}}} = \frac{2 + \mathcal{A}}{2 - \mathcal{A}} \tag{5.6}$$

For given values of η^{left} and η^{right}, the relative response between the two regions can be defined as

$$\mathcal{R}_{ijk} = \frac{2 - \langle \mathcal{A}_{ijk} \rangle}{2 + \langle \mathcal{A}_{ijk} \rangle} = \frac{c_{ik}^{\mathrm{left}}}{c_{jk}^{\mathrm{right}}} \tag{5.7}$$

where i, j and k are label bins in η^{left}, η^{right} and ${p_{\mathrm{T}}}^{ave}$ respectively, and $\langle \mathcal{A} \rangle$ is the mean[1] of the asymmetry distribution.

For every k-th ${p_{\mathrm{T}}}^{ave}$ bin, there exists $\frac{1}{2}N(N-1)$ relative responses, $\mathcal{R}_{ijk}$, corresponding to different η^{left} and η^{right} bins (i,j), where N is the number of bins in η. A minimisation is performed to take into account the response measurements between many regions, to extract the inter-calibration factors for a specific η

[1]The asymmetry distribution is fitted with a Gaussian function between -0.7 and 0.7, and the value of the fit is taken as the mean, unless there are low statistics, then the average of the asymmetry is taken

region. The inverse of the variance on each measured relative response, $\Delta\mathcal{R}_{ijk}$, is used to weight the equations in a minimisation equation,

$$\mathcal{M}_k = \sum_{j=1}^{N}\sum_{i=j}^{N}\left\{\frac{1}{\Delta\mathcal{R}_{ijk}}(c_{jk}\mathcal{R}_{ijk} - c_{ik})\right\}^2 + X(c_{ik}). \tag{5.8}$$

The first term in Equation 5.8 is minimised to find the values of c_{ik} that best agree with the measured $\mathcal{R}_{ijk}$. A trivial undesired solution is $c_{ik} = 0$. The second term in 5.8 is added to prevent this solution. The specific form is

$$X(c_{ik}) = K(N_{bins}^{-1}\sum_{i=1}^{N_{bins}} c_{ik} - 1)^2, \tag{5.9}$$

where K is a constant. This term is a minimum when the average correction factor is equal to unity. K is set to 10^6, and its purpose is to penalise deviations of the average away from 1. For large values of K, the correction factors found are stable. Once the minimised c_{ik} values are found, these values are rescaled such that the correction factors at $|\eta| < 1$ are equal to unity.

The advantage of this method with respect to the standard method is that each relative response is calculated using every η bin combination, which gives an increase in the statistics used, especially at larger η, when compared to the standard method which needed one of the jets to be in the central probe region.

Two and Three Bin Example of Matrix Method

To understand the matrix method, a two-bin and a three-bin case are discussed further. The equation relating the two η bins for the k-th ${p_\mathrm{T}}^{ave}$ bin is,

$$\mathcal{M}_k = c_{2k}\mathcal{R}_{12\mathrm{k}} - c_{1k}. \tag{5.10}$$

The equation is minimised when $c_{2k}\langle\mathcal{R}_{12\mathrm{k}}\rangle = c_{1k}$ with a requirement that the average value is equal to unity. Setting the first η bin to the reference region with a $c_{2k} = 1$, then

$$c_{1k} = \mathcal{R}_{12\mathrm{k}} = \frac{2 - \langle\mathcal{A}_{\mathrm{ijk}}\rangle}{2 + \langle\mathcal{A}_{\mathrm{ijk}}\rangle} \tag{5.11}$$

which is the same as Equation 5.4 used in the standard method. For a three-bin case, with η bin indices $1, 2, 3$ the relevant factors are:

$$\begin{aligned} &c_{2k}\mathcal{R}_{12\mathrm{k}} - c_{1k} \\ &c_{3k}\mathcal{R}_{13\mathrm{k}} - c_{1k} \\ &c_{3k}\mathcal{R}_{23\mathrm{k}} - c_{2k} \end{aligned} \tag{5.12}$$

and the minimisation equation is,

$$\mathcal{M}_k = \left(\frac{c_{2k}\mathcal{R}_{12\mathrm{k}} - c_{1k}}{\Delta\mathcal{R}_{12\mathrm{k}}}\right)^2 + \left(\frac{c_{3k}\mathcal{R}_{13\mathrm{k}} - c_{1k}}{\Delta\mathcal{R}_{13\mathrm{k}}}\right)^2 + \left(\frac{c_{3k}\mathcal{R}_{23\mathrm{k}} - c_{2k}}{\Delta\mathcal{R}_{23\mathrm{k}}}\right)^2 + X(c_{ik}). \tag{5.13}$$

The minimisation attempts to minimise the first three terms, while also keeping the mean correction at unity (fourth term). The variance on $\mathcal{R}$, $\Delta\mathcal{R}$, is smaller for high statistics measurements of $\mathcal{R}$. Including the variance in the minimisation, gives measurements with a low variance a higher importance in determining the values of c_{ik}.

5.2 2011 Study of Pile-up Dependence

Event Selection

The jets in the analysis are reconstructed using the anti-k_t algorithm with a distance parameter $R = 0.4$ and calibrated using the JES scheme (discussed in Section 3.4). The analysis requires that a single jet trigger has been passed. Triggers are used if they are in the plateau region of the turn-on curve, corresponding to a greater than 99% efficiency. The trigger used for a given ${p_\mathrm{T}}^{ave}$ is shown in Table 5.1. A trigger with name jX requires an EF-level trigger jet with EM scale p_T >X GeV. The data are required to be in luminosity blocks when all ATLAS sub-detectors are fully functioning.

To ensure the $2 \to 2$ scattering topology the $\Delta\phi$ between the two jets is required to be greater than 2.5 rad and events containing a third jet with p_T >

${p_{\mathrm{T}}}^{ave}$ [GeV]	Trigger
$22-30$	j10
$30-40$	j15
$40-55$	j20
$55-75$	j30
$75-100$	j40
$100-130$	j55
$130-170$	j75
$170-220$	j100
$220-300$	j135
$300-400$	j180

Table 5.1: Trigger strategy for the different dijet ${p_{\mathrm{T}}}^{ave}$.

0.25 ${p_{\mathrm{T}}}^{ave}$ are removed. The reference region that is used to do the final rescaling of the responses in the matrix method is $-0.8 < \eta < 0.8$.

Basic Asymmetry and Response Distributions

Figures 5.1 and 5.2 each show two asymmetry distributions for jets falling in (a) two central regions, $-0.8 < \eta_{left} < -0.1$ and $0.1 < \eta_{right} < 0.8$, and (b) one central region and one more forward region, $0.1 < \eta_{left} < 0.8$ and $2.1 < \eta_{right} < 2.8$. Each asymmetry distribution has been fitted with a Gaussian function from $-0.7 < \mathcal{A} < 0.7$.

Figure 5.1 shows asymmetry distributions for $30 < {p_{\mathrm{T}}}^{ave} < 40$ GeV jets. The peak of the fitted asymmetry for both jets falling in the central region is 0.006, which corresponds to a very small p_{T} imbalance of $\langle {p_{\mathrm{T}}}^{right} \rangle = 0.994 \langle {p_{\mathrm{T}}}^{left} \rangle$. The peak of the fitted asymmetry for one jet falling in the central region and the other in a forward region is 0.023, which corresponds to a p_{T} imbalance of $\langle {p_{\mathrm{T}}}^{right} \rangle = 0.98 \langle {p_{\mathrm{T}}}^{left} \rangle$.

Figure 5.2 shows asymmetry distributions for $55 < {p_{\mathrm{T}}}^{ave} < 75$ GeV jets. The peak of the fitted asymmetry for both jets falling in the central region is 0.003, which corresponds to very small p_{T} imbalance of $\langle {p_{\mathrm{T}}}^{right} \rangle = 0.997 \langle {p_{\mathrm{T}}}^{left} \rangle$.

The peak of the fitted asymmetry for one jet falling in the central region and the other in a forward region is 0.007, which corresponds to a p_{T} imbalance of $\langle {p_{\mathrm{T}}}^{right} \rangle = 0.993 \langle {p_{\mathrm{T}}}^{left} \rangle$.

The width in the asymmetry distributions arises due to the jet energy resolution of the two jets and the peak value of the fitted asymmetry relates to the relative responses of the two regions. In the distributions for both the low and high ${p_{\mathrm{T}}}^{ave}$ jets, the case where both jets fall into central regions has a lower p_{T} imbalance than the case where one jet falls into a forward region. When both jets fall into the barrel region they are better calibrated, as the barrel region is well understood (through test beam information and single hadron response) and has little dead material. However, when one jet is further forward, it falls into the end-cap region of the calorimeter and the difference observed could be due to the differing abilities to calibrate the different parts of the detector. The spread of asymmetry is smaller for higher ${p_{\mathrm{T}}}^{ave}$ jets, which is due to the improved resolution for higher p_{T} jets.

Figures 5.3 and 5.4 show the the response matrices, which are used by the minimisation, for jets in the range $30 < {p_{\mathrm{T}}}^{ave} < 40$ GeV and $55 < {p_{\mathrm{T}}}^{ave} < 75$ GeV, respectively. The low ${p_{\mathrm{T}}}^{ave}$ jets have a larger range of relative responses than the high ${p_{\mathrm{T}}}^{ave}$ jets, with some bins deviating from unity by up to 6%. In both response matrices the higher η bins have a larger spread of responses than the more central bins.

Figure 5.5 shows the relative response as a function of detector η for $22 < {p_{\mathrm{T}}}^{ave} < 30$ GeV jets, $30 < {p_{\mathrm{T}}}^{ave} < 40$ GeV jets, and $55 < {p_{\mathrm{T}}}^{ave} < 75$ GeV jets. The largest relative response occurs for low ${p_{\mathrm{T}}}^{ave}$. There is a relative response of about 1.02 at $|\eta| = 1$ which corresponds to the crack region between the tile barrel and tile extended barrel. This crack can be seen in the jet energy EM-scale response in Figure 3.6. For low p_{T} jets, the calibration has over-calibrated the jets

in this crack region. For the medium and high jet p_{T} ranges shown, the relative response for $|\eta| < 1$ is very close to unity. The response at higher η deviates away from unity, and as the jet p_{T} increases this deviation reduces.

Effect of Pile-up on Dijet Balance

The p_{T} balance of dijets events can be used to construct a correction factor or used to ascertain aspects of the JES uncertainty [39]. In this section it is used as a cross-check of JES uncertainty components from pile-up. This is done by calculating the relative response for events with different levels of pile-up.

Two estimators of the amount of pile-up used are the number of primary vertices, $\mathrm{N_{PV}}$, and the mean number of interactions per bunch crossing, μ. Figure 5.6 shows (a) the $\mathrm{N_{PV}}$ distribution and (b) the μ distributions. $\mathrm{N_{PV}}$ and μ cuts are chosen to select events with different amount of pile-up. For the $\mathrm{N_{PV}}$ cuts, three slices are chosen such that each has good statistics, but also has differences in the average $\mathrm{N_{PV}}$ per slice. Three $\mathrm{N_{PV}}$ regions are defined to select different pile-up conditions, $0 \leq \mathrm{N_{PV}} \leq 2$, $3 \leq \mathrm{N_{PV}} \leq 6$, and $\mathrm{N_{PV}} \geq 7$, with an average $\mathrm{N_{PV}}$ of 2.48, 4.48 and 7.71, respectively. For the μ cuts, two slices are chosen, one that includes the peak, and one that includes the tail, both of with have good statistics. Two μ regions are defined, $0 \leq \mu \leq 7$ and $\mu > 7$, with an average μ of 5.33 and 9.94, respectively. Data points which have no cuts on μ or $\mathrm{N_{PV}}$ are also shown for comparative purposes. These have an average $\mathrm{N_{PV}}$ and μ of 5.19 and 6.48, respectively.

Figures 5.7, 5.8 and 5.9 show the relative response as a function of detector η for jets with $22 < {p_{\mathrm{T}}}^{ave} < 30$ GeV, $30 < {p_{\mathrm{T}}}^{ave} < 40$ GeV and $55 < {p_{\mathrm{T}}}^{ave} < 75$ GeV, respectively, for different $\mathrm{N_{PV}}$ ranges. For the $22 < {p_{\mathrm{T}}}^{ave} < 30$ GeV jets, the relative response in the forward bins is lower for jets in the low pile-up conditions than the jets using the full data. The medium has a higher relative

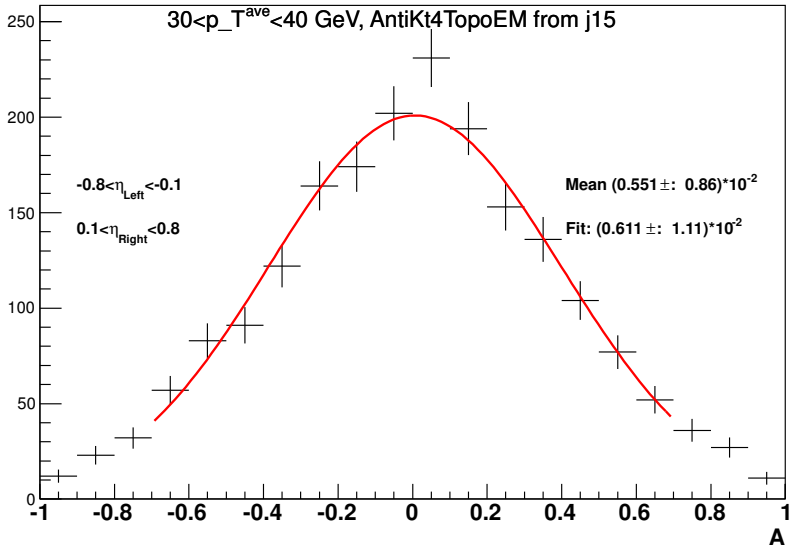

(a)

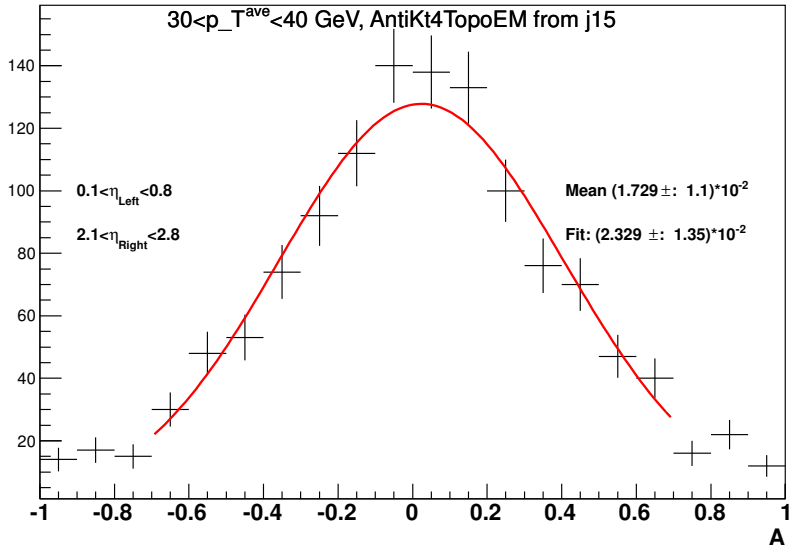

(b)

Figure 5.1: Asymmetry distribution for jets with $30 < {p_{\mathrm{T}}}^{ave} < 40$ GeV with (a) $-0.8 < \eta_{left} < -0.1$ and $0.1 < \eta_{right} < 0.8$ and (b) $0.1 < \eta_{left} < 0.8$ and $2.1 < \eta_{right} < 2.8$. The distribution is fitted using a Gaussian function between $-0.7 < \mathrm{A} < 0.7$ and the fit result and error is shown as is the mean and error on the mean.

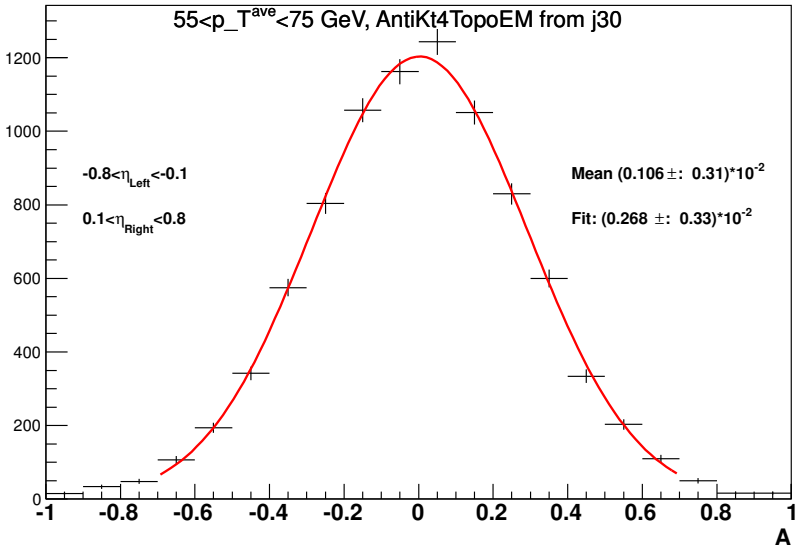

(a)

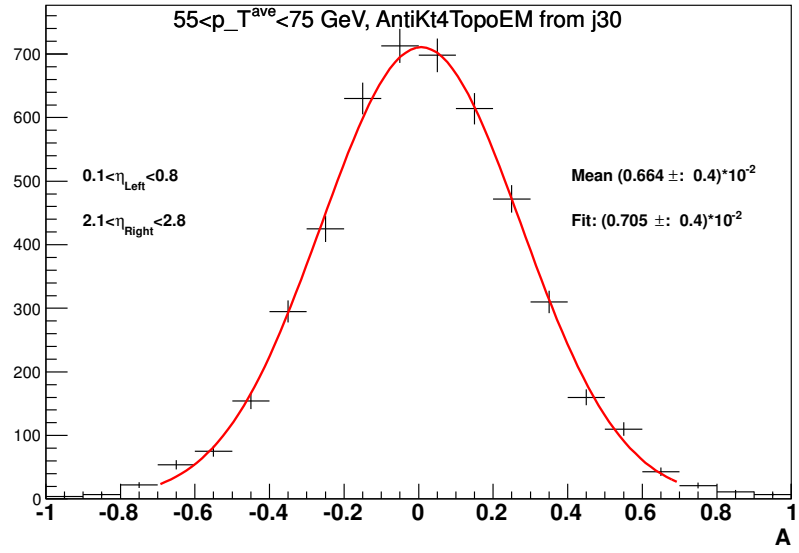

(b)

Figure 5.2: Asymmetry distribution for jets with $55 < p_{\mathrm{T}}{}^{ave} < 75$ GeV with (a) $-0.8 < \eta_{left} < -0.1$ and $0.1 < \eta_{right} < 0.8$ and (b) $0.1 < \eta_{left} < 0.8$ and $2.1 < \eta_{right} < 2.8$. The distribution is fitted using a Gaussian function between $-0.7 < \mathrm{A} < 0.7$ and the fit result and error is shown as is the mean and error on the mean.

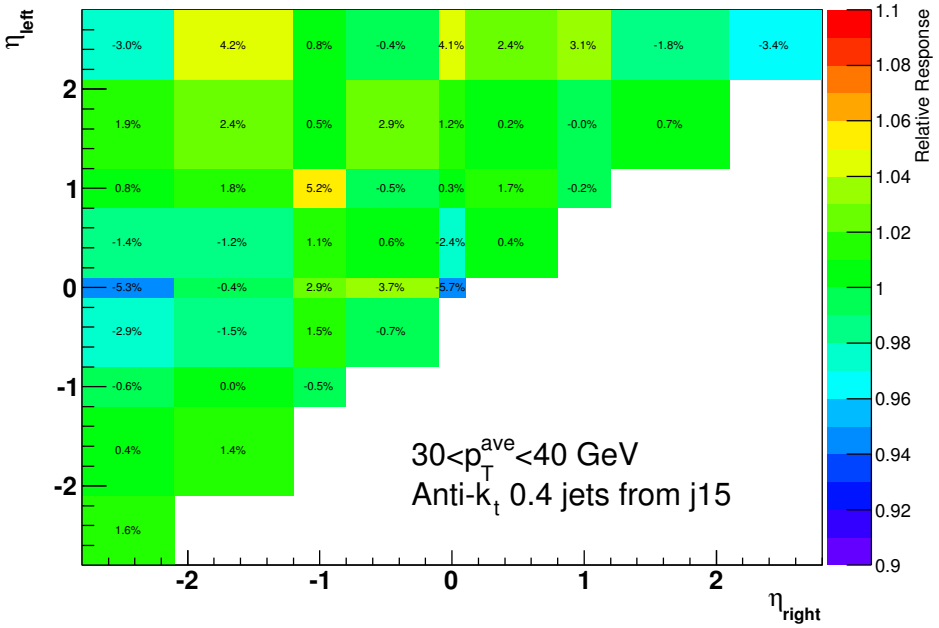

Figure 5.3: Response matrix for $30 < {p_T}^{ave} < 40$ GeV for jets which passed the j15 trigger. The text in the bins corresponds to the percentage difference between the response and unity.

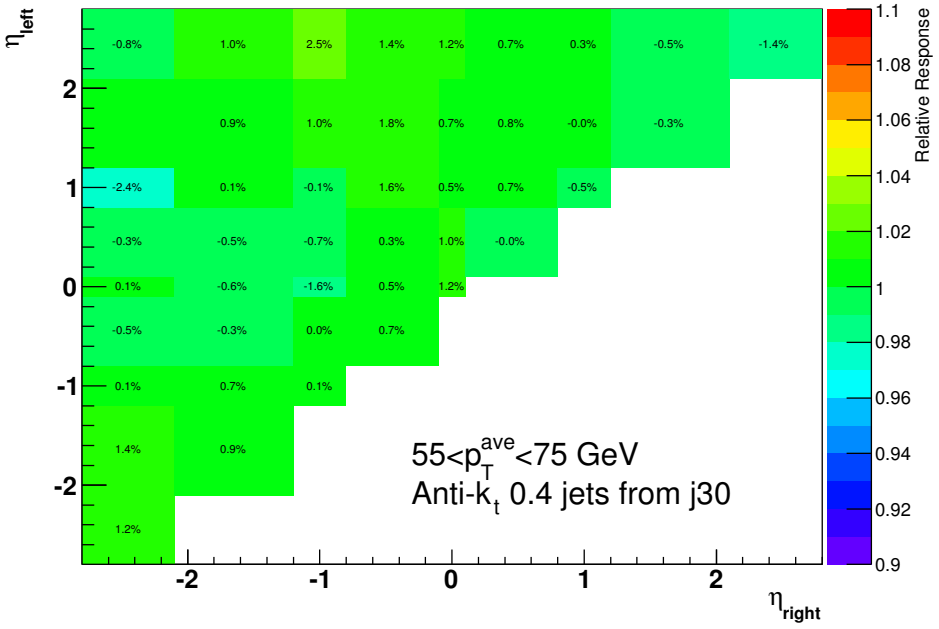

Figure 5.4: Response matrix for $55 < {p_T}^{ave} < 75$ GeV for jets which passed the j30 trigger. The text in the bins corresponds to the percentage difference between the response and unity.

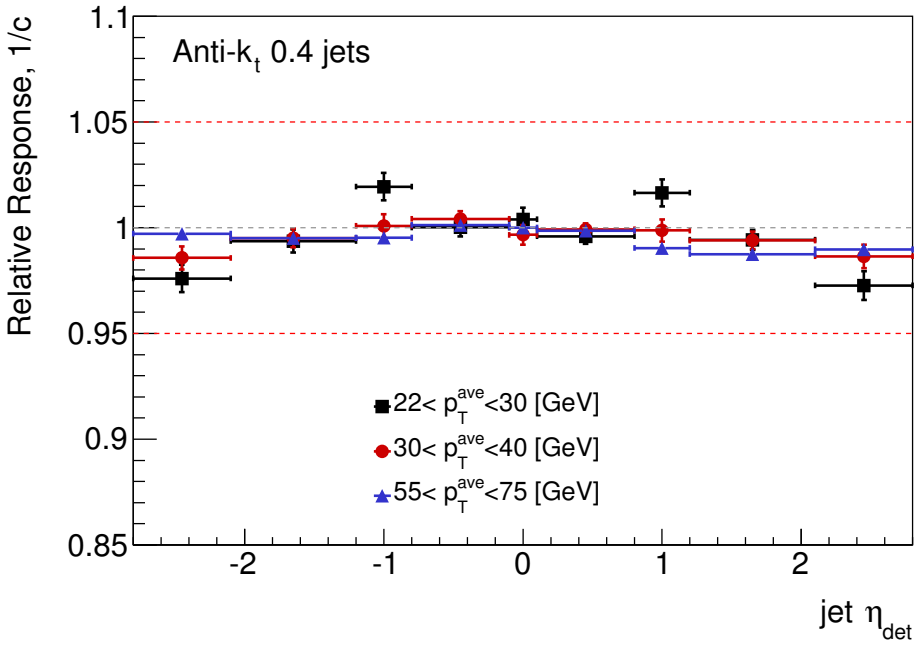

Figure 5.5: Relative response as a function of detector η for jets with $22 < p_{\mathrm{T}}{}^{ave} < 30$ GeV, $30 < p_{\mathrm{T}}{}^{ave} < 40$ GeV and $55 < p_{\mathrm{T}}{}^{ave} < 75$ GeV.

response in the bins outside the reference region. The spread of the three different $\mathrm{N_{PV}}$ points is contained within $\approx 4\%$ and there is no systematic difference in spread as a function of η. For the $30 < p_{\mathrm{T}}{}^{ave} < 40$ GeV jets, the spread has decreased to within $\approx 2\%$. In the forward bins at negative η, the low pile-up and high pile-up have a higher and lower response than the average, respectively, however this is probably just fluctuations as there is no pathological effect. For the $55 < p_{\mathrm{T}}{}^{ave} < 75$ GeV jets, the spread is within $\approx 1\%$, and there is no obvious trend in the differences between the different pile-up conditions.

The observation that the low $p_{\mathrm{T}}{}^{ave}$ jets are affected more, is not unexpected, as pile-up can be considered to add a fixed amount of additional energy per additional proton-proton interaction. This additional energy will be a larger fraction of a low p_{T} jet than of a high p_{T} jet at the same rapidity, and so the

net effect will be larger. It might be expected that the jets in the lower pile-up conditions should have a lower relative response than jets in a higher pile-up condition, however the EM+JES calibration does a pile-up offset correction, which should account for this.

Figures 5.10, 5.11 and 5.12 show the relative response as a function of detector η for jets with $22 < {p_{\mathrm{T}}}^{ave} < 30$ GeV, $30 < {p_{\mathrm{T}}}^{ave} < 40$ GeV and $55 < {p_{\mathrm{T}}}^{ave} < 75$ GeV respectively for different μ ranges. For the $22 < {p_{\mathrm{T}}}^{ave} < 30$ GeV jets, the spread is $\approx 3\%$ for $-2.8 \leq \eta \leq -2$ range, but for most bins it is within $1-2\%$. In most of the bins the low pile-up sample has a responses slightly higher than the response from the high pile-up samples. For the $30 < {p_{\mathrm{T}}}^{ave} < 40$ GeV jets, the relative responses are closer to unity than for the lower ${p_{\mathrm{T}}}^{ave}$ jets. The spread is consistently 2% with approximately equal number of bins where the low pile-up sample is above the high pile-up sample, than the reverse. For the $55 < {p_{\mathrm{T}}}^{ave} < 75$ jets, the spread is $< 1\%$ for all but one bin, and the relative response is close to one. As with the assessment of the pile-up using the $\mathrm{N_{PV}}$, the spread shows a general downwards trend for higher ${p_{\mathrm{T}}}^{ave}$, though the jets with $30 < {p_{\mathrm{T}}}^{ave} < 40$ GeV have a marginally higher spread than $22 < {p_{\mathrm{T}}}^{ave} < 30$ GeV, but without the larger fluctuations.

The observed effects from $\mathrm{N_{PV}}$ and μ are $3-4\%$ for low ${p_{\mathrm{T}}}^{ave}$ jets, and reduce to 1% for jets with $55 < {p_{\mathrm{T}}}^{ave} < 75$. These spreads of values for the relative response show agreement to the JES uncertainty due to pile-up using the method described in [43] and combined to the JES uncertainty in [44].

5.3 2010 Forward Jet Validation

In 2010, the dijet p_{T} balance method was not used to recalibrate the jets, but was used to assess the uncertainty on the JES calibration factors. However, the relative jet response [45] shows a difference in the forward region for MC

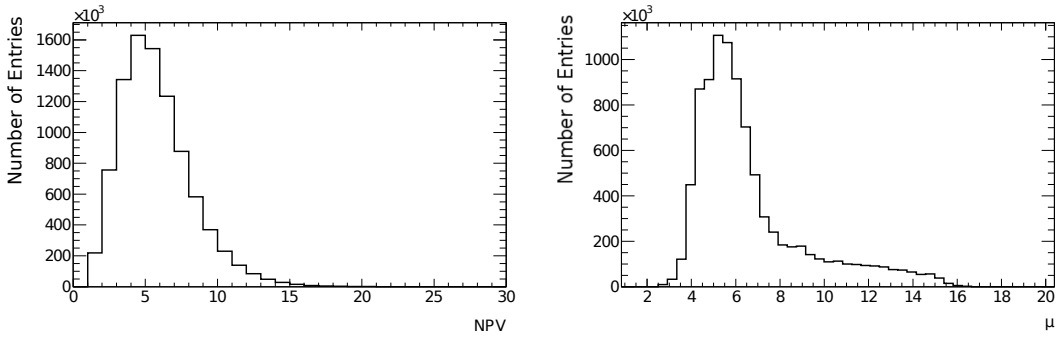

(a) (b)

Figure 5.6: (a) The N_{PV} distribution and (b) the μ distribution for 2011 data.

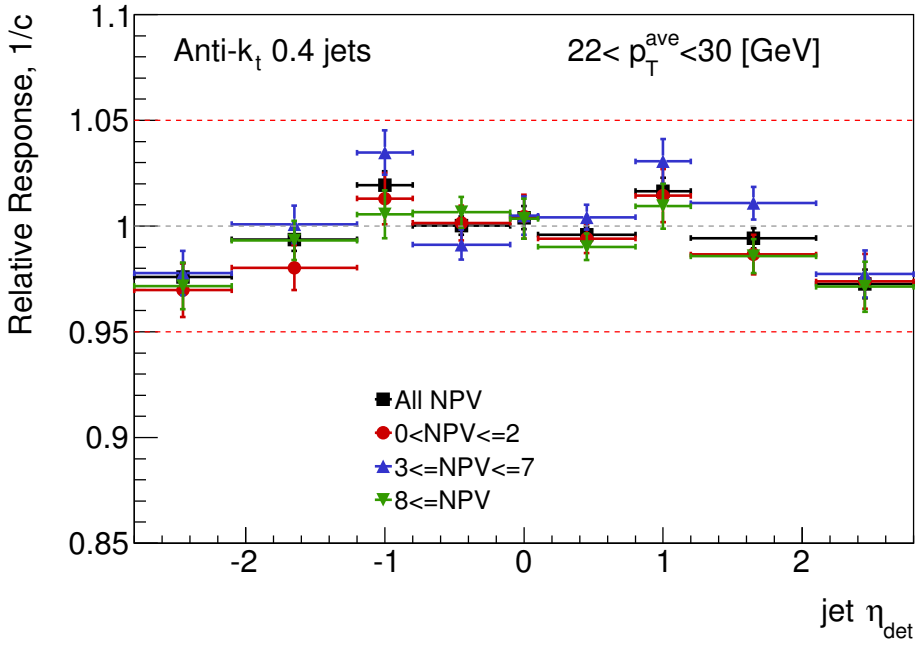

Figure 5.7: Relative response as a function of detector η for jets with $22 < p_T{}^{ave} < 30$ GeV. Relative responses are shown for events with $0 \leq N_{PV} \leq 2$, $3 \leq N_{PV} \leq 6$, $N_{PV} \geq 7$ and all N_{PV}.

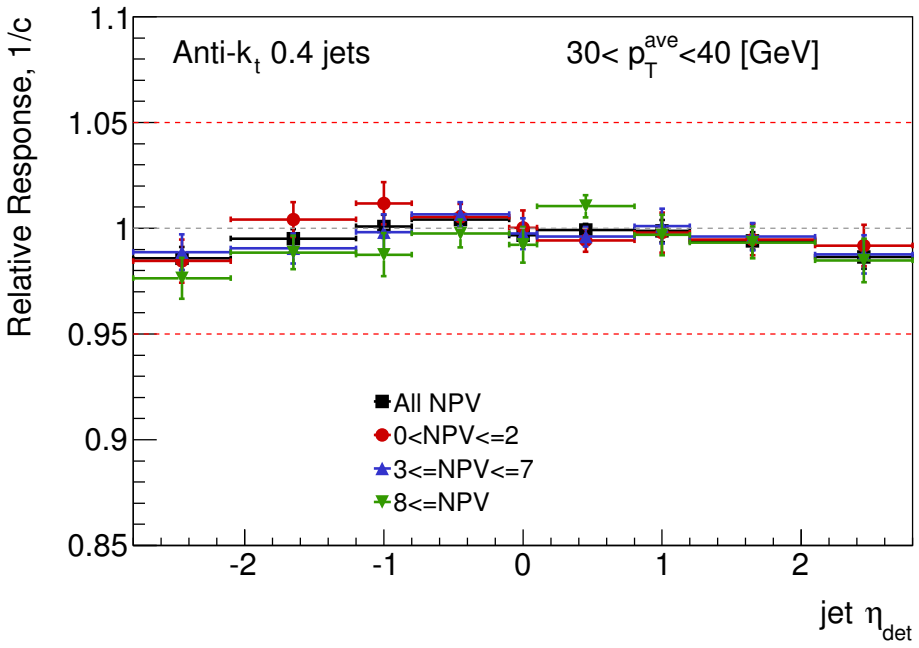

Figure 5.8: Relative response as a function of detector η for jets with $30 < p_{\mathrm{T}}{}^{ave} < 40$ GeV. Relative responses are shown for events with $0 \leq \mathrm{N_{PV}} \leq 2$, $3 \leq \mathrm{N_{PV}} \leq 6$, $\mathrm{N_{PV}} \geq 7$ and all $\mathrm{N_{PV}}$.

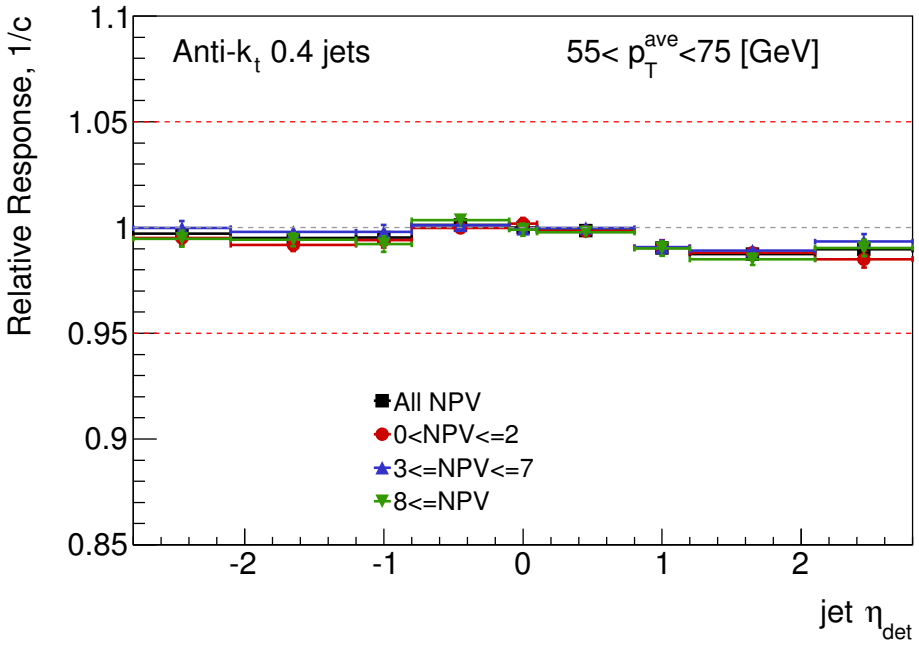

Figure 5.9: Relative response as a function of detector η for jets with $55 < p_{\mathrm{T}}{}^{ave} < 75$ GeV. Relative responses are shown for events with $0 \leq \mathrm{N_{PV}} \leq 2$, $3 \leq \mathrm{N_{PV}} \leq 6$, $\mathrm{N_{PV}} \geq 7$ and all $\mathrm{N_{PV}}$.

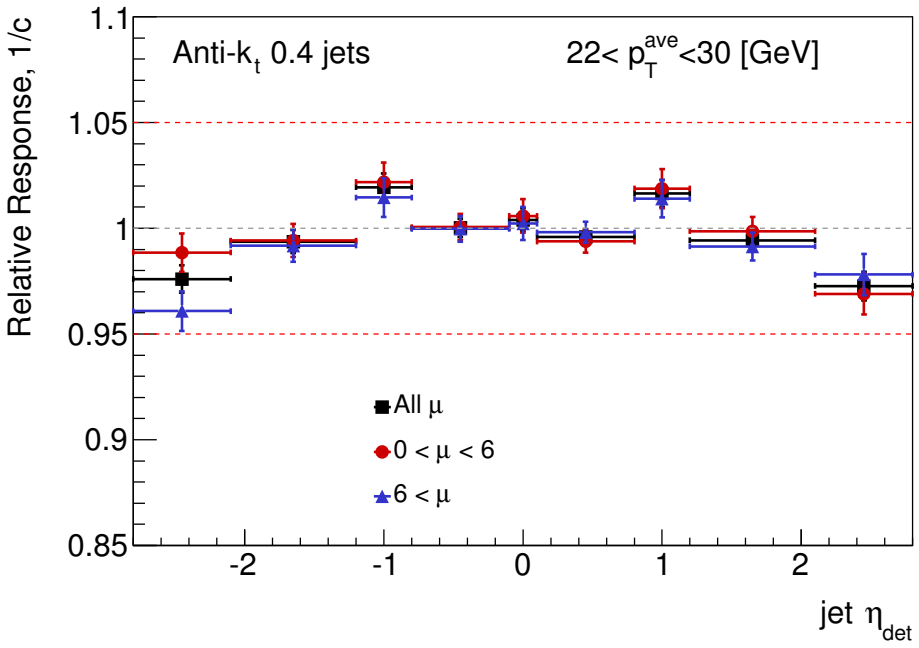

Figure 5.10: Relative response as a function of detector η for jets with $22 < {p_T}^{ave} < 30$ GeV. Relative responses are shown for events with $0 \leq \mu \leq 6$, $\mu \geq 6$ and all μ.

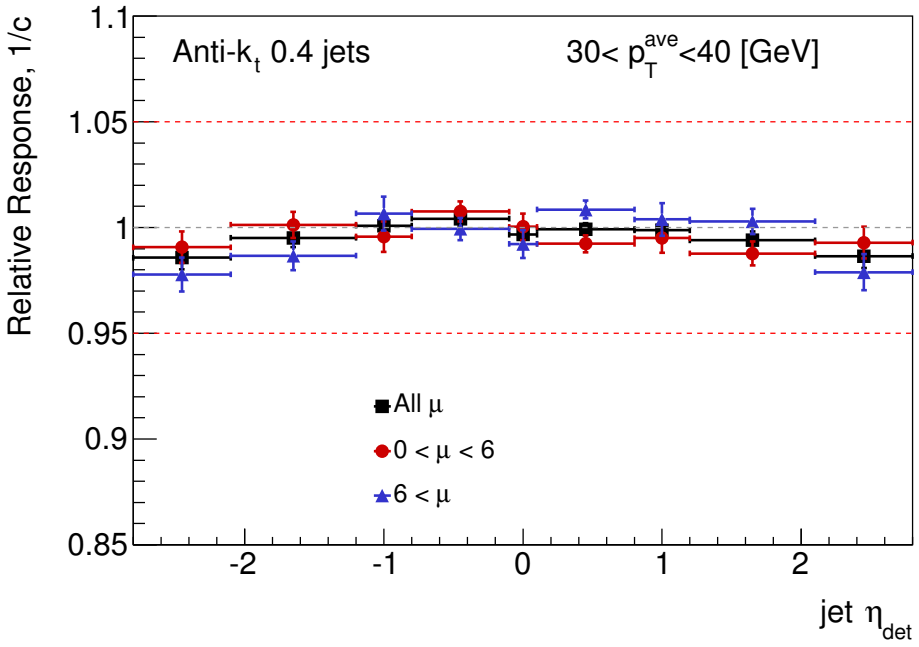

Figure 5.11: Relative response as a function of detector η for jets with $30 < {p_T}^{ave} < 40$ GeV. Relative responses are shown for events with $0 \leq \mu \leq 6$, $\mu \geq 6$ and all μ.

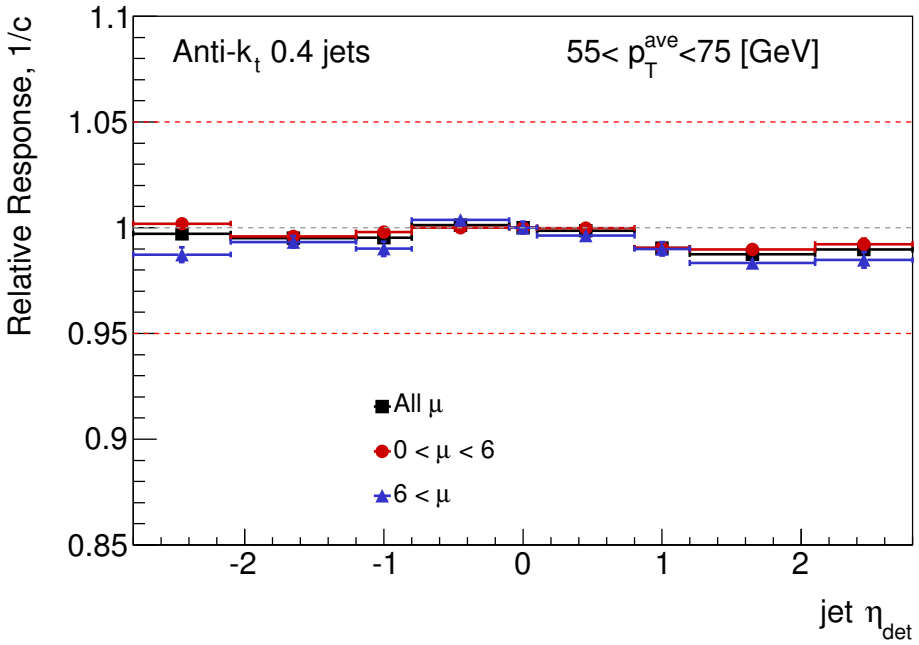

Figure 5.12: Relative response as a function of detector η for jets with $55 < {p_{\mathrm{T}}}^{ave} < 75$ GeV. Relative responses are shown for events with $0 \leq \mu \leq 6$, $\mu \geq 6$ and all μ.

and data. The difference between the data and MC jet responses could either originate from physics or the detector effects described in Section 3.4. Until the source of the differences is determined, these relative response factors should not be used to calibrate the jets for physics analysis. However, they are used to test the closure of the calibration and to see if the difference between data and MC can be resolved.

Using the ratio of the relative response factors from the MC and the data, the residual correction,

$$\mathcal{C}_{\mathrm{in-situ}} = \frac{\mathrm{c_{MC}}}{\mathrm{c_{Data}}} \tag{5.14}$$

is calculated as a function of jet p_{T} and η, where $1/\mathrm{c_{MC}}$ and $1/\mathrm{c_{Data}}$ are the relative response factors for MC and data, respectively.

Figure 5.13 shows the jet η distribution for (a) $p_{\mathrm{T}} > 30$ GeV from the Min

Bias trigger and (b) p_{T}> 50 GeV from the calorimeter trigger stream. The in-situ calibrated data has a much better agreement with the MC than the uncorrected data in both plots. There are still differences in the forward region, but overall the differences are smaller than 10%.

Figure 5.14 shows (a) the jet energy and (b) the p_{T} distributions for jets in the region $3.2 < |\eta| < 4.5$ for $p_{\mathrm{T}}>$ 20 GeV. The energy distribution shows improvements in agreement between the MC after the data has been calibrated. The energy distributions is affected by the kinematic selection in both p_{T} and η. The change in slope at E$\approx$ 900 GeV corresponds to where jets with $\eta = 4.2$ first contribute to the distribution. The p_{T} distribution shows smaller differences for the in-situ calibrated data.

These results show that calibration brings the data into closer agreement with the MC, giving confidence to the method and the results. This confidence resulted in the decision to use the dijet p_{T} balance method to calibrate the jets in the 2011 sample. These plots were published in an ATLAS conference note [45].

5.4 Forward Jet Properties

The internal structure of jets in the forward region were examined using 2010 data to assess how well the MC simulation reproduces the data. The transverse size of the jet is quantified using the jet width,

$$\text{Width} = \frac{\sum(r^{\text{cluster}} \times {E_{\mathrm{T}}}^{\text{cluster}})}{\sum {E_{\mathrm{T}}}^{\text{cluster}}}, \tag{5.15}$$

where the sums are over all clusters within the jet, and r^{cluster} is the distance, ΔR, of each cluster from the jet centre, with the maximum being the jet radius R. Another important jet observable is the electromagnetic fraction (EMF), which is the fraction of the total jet energy (at EM scale) coming from electromagnetic clusters.

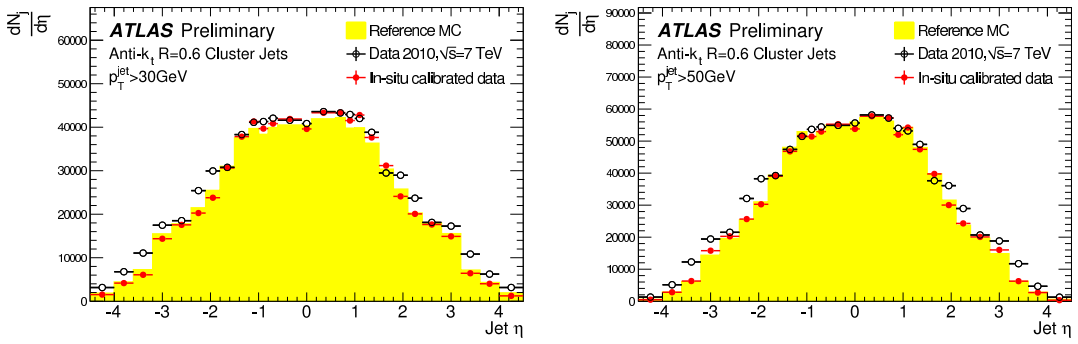

(a) (b)

Figure 5.13: η distribution for jets with (a) $p_{\mathrm{T}} > 30$ GeV from the Min Bias trigger and (b) $p_{\mathrm{T}} > 50$ GeV from the calorimeter trigger stream. Uncorrected data (open black circles) and corrected data (red circles) are shown along with the reference MC.

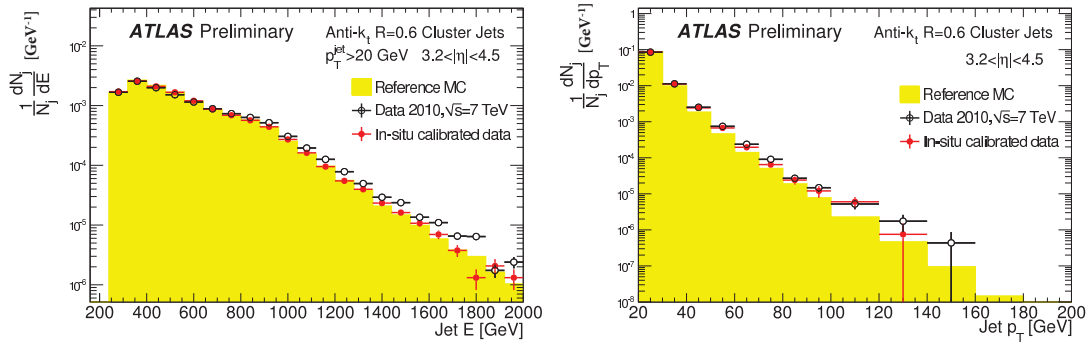

(c) (d)

Figure 5.14: (a) Jet energy and (b) jet p_{T} for the region $3.2 < |\eta| < 4.5$. Uncorrected data (open black circles) and corrected data (red circles) are shown along with the reference MC.

Physics List	Hadron Energy Range (GeV)		
	Low	Medium	High
QGSP		$0-25$ LEP	>12 QGSP
QGSP_BERT	$0-9.9$ BERT	$9.5-25$ LEP	>12 QGSP
FTFP_BERT	$0-5$ BERT		>4 FTF

Table 5.2: Hadron interaction models for different sets of physics models for various hadron energies. Taken from Table 6 in [46].

Figure 5.15 (a) shows the jet width for jets in the forward region. Figure 5.15 (b) shows the EMF for jets in the forward region. The data are compared to PYTHIA using three different sets which use different calorimeter interaction models. The three sets of physics models used, QGSP, QGSP_BERT, and FTFP_BERT are discussed in [46]. These sets define different aspects of modelling the interactions of hadrons with matter and are shown in Table 5.2.

The QGSP [47] set contains the quark gluon string model, which is a phenomenological model describing the parton production arising from collisions between hadrons and nucleons, for high energy hadrons, and uses a low energy parameterisation model (LEP), which is based on extrapolating measured reaction cross-sections for the low energy hadrons. The QGSP_BERT set still uses QGSP at high hadronic energy, but only uses LEP at medium energies. For low energy hadrons, the Bertini nucleon-nucleon scattering model (BERT) [48] is used. This is an alternative model for the low energy interaction of hadrons in the nucleon medium. FTFP_BERT uses the Fritiof fragmentation model (FTF) [49] to model the high energy interactions. In regions where there is overlap between the different models, there is linear interpolation between them.

By comparing the standard PYTHIA set, QGSP_BERT, to QGSP and FTFP_BERT, the effects of removing the BERT model and also changing from the QGS model to the FTF model can be seen.

None of the sets of physics models manage to describe accurately the data, and the width is consistently higher in data than in the simulations. These differences

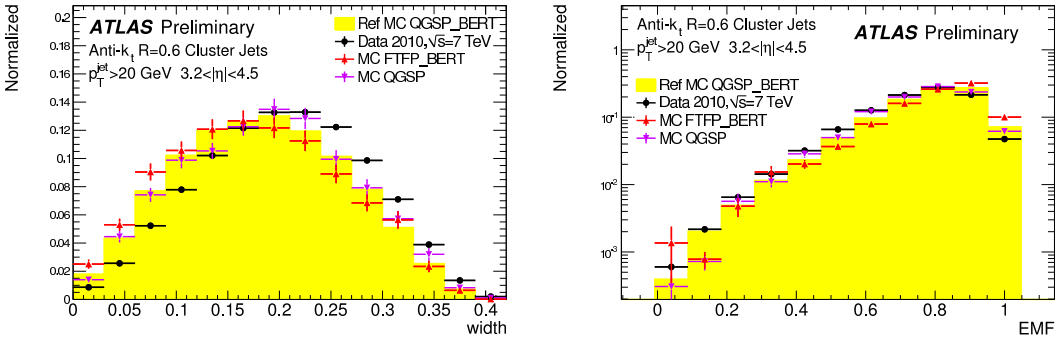

(a) (b)

Figure 5.15: (a) Jet width and (b) jet EMF for jets with p_{T}> 20 GeV and in the region $3.2 < |\eta| < 4.5$. The 2010 data is compared to standard PYTHIA with the different sets of physics models, QGSP_BERT (yellow filled), FTFP_BERT (red circles) and QGSP (purple circles).

have also been observed for central jets, though with smaller magnitude [50]. As concluded in [46], the set of physics models chosen as default at ATLAS produced narrower and shorter showers than data, but gave the best agreement with the data for the pion response. These results have been published in an ATLAS conference note [45].

Chapter 6

Measurement of Dijet Production with a Veto on Additional Central Jet Activity

The study into dijet production with a jet veto is presented. These observables are compared for a dijet rapidity separation of up to $\Delta y = 6$, and $50 \leq \overline{p_{\mathrm{T}}} < 500$ GeV. The data are compared to POWHEG with both the PYTHIA parton shower (POWHEG + PYTHIA) and the HERWIG parton shower (POWHEG + HERWIG), and also to the HEJ generator. The data are also compared to PYTHIA and HERWIG++. A description of these generators can be found in Section 2.4.

Measurements of dijet production with a veto on additional activity have been made at both HERA [51–53] and the Tevatron [54–58]. However, they differed from this measurement by vetoing on very low energy deposits. Using this veto, they were able to study dijet production with color-singlet exchange.

The topology and event selection are outlined in Section 6.1 and 6.2, respectively. In Section 6.3, the selected data will be compared to the simulated PYTHIA

sample. In Section 6.4, the robustness of the event selection will be examined. Section 6.5 outlines the work done by other members of the analysis team that is required to get the final measurements, which are presented in Section 6.6 and published in [1].

6.1 Topology Selection

The jets used in this analysis are reconstructed using the anti-k_t algorithm with a radius parameter $R = 0.6$, as described in Section 2.3. Only jets with $p_{\mathrm{T}} > 20$ GeV and $|y| < 4.4$ are used, as these are the regions that have a well defined jet energy scale and jet cleaning criteria, as discussed in Section 3.4.

The analysis uses two different dijet selection criteria, "Leading p_{T} Dijet Selection" and "Forward/Backward Selection", to define two boundary jets. In the leading dijet p_{T} selection the boundary jets are the two highest p_{T} jets in the event, whereas in the forward/backward selection the two boundary jets are the most forward (positive rapidity) and most backward (negative rapidity) jets in the event. Once the boundary jets have been defined, an additional cut is applied to the average transverse momentum, $\overline{p_{\mathrm{T}}}$, of the boundary jets of $\overline{p_{\mathrm{T}}} > 50$ GeV. This ensures that the dijets are in a high efficiency trigger region [59]. These cuts define the inclusive event sample for the analysis.

Two variables are investigated; the gap fraction and the mean number of jets in the rapidity interval between the boundary jets. The gap fraction, f_{gap}, defined in Equation 2.9, can be measured by,

$$f_{\mathrm{gap}}(Q_0) = \frac{\sigma_0}{\sigma} = \frac{N(Q_0)}{N}, \tag{6.1}$$

where $N(Q_0)$ is the number of events that do not contain a jet with $p_{\mathrm{T}} > Q_0$ in the rapidity interval between the boundary jets, and N is the number of events in the inclusive sample. The trigger acceptance and luminosity biases are assumed to

cancel in the ratio. The nominal choice of the jet veto scale is $Q_0 = 20$ GeV. The mean number of jets in the rapidity interval is defined for jets with $p_{\mathrm{T}} > 20$ GeV.

Both the gap fraction and the mean number of jets are measured as a function of dijet rapidity region, Δy, for multiple slices in $\overline{p_{\mathrm{T}}}$, and also as a function of $\overline{p_{\mathrm{T}}}$ for multiple slices in Δy. The gap fraction is also measured as a fraction of the veto scale, Q_0.

6.2 Event selection

6.2.1 Data Samples

The analysis is performed on pp collision data with a centre-of-mass energy of 7 TeV recorded between April and October 2010 using the ATLAS detector. Data are only used if they were collected during stable beam conditions with good data quality. The data quality is assessed by the ATLAS performance working groups by checking that all the parts of the detector and trigger were performing normally, and the physics objects (for instance jets and muons) are being correctly reconstructed. This is achieved by the application of a "good runs list" (GRL) which is a list of runs and the luminosity blocks in which the data quality and beam conditions have been declared adequate by the relevant performance groups.

6.2.2 Trigger Strategy

The trigger strategy uses the ATLAS jet triggers to select events. For a given dijet $\overline{p_{\mathrm{T}}}$, a specific trigger is required to have fired for the event to be included in the analysis. The trigger depends on the data period the event was collected in.

During the data periods B-D, only the level 1 (L1) jet triggers are used for selecting events. During periods E-I, the level 2 (L2) jet triggers are also used.

The L1 and L2 (named EF) jet triggers have names of the format L1_JX, where X is the EM transverse energy threshold. The jet triggers used only inputs from $|\eta| < 3.2$ to build trigger jets.

Table 6.1 shows the trigger requirement for different $\bar{p_T}$ regions and data periods.

$\overline{p_{\mathrm{T}}}$ [GeV]	Period B-D	Period E-F	Period G-I
50 - 70	L1_J5	EF_j20_jetNoCut	EF_j20_jetNoEF
70 - 90	L1_J10	EF_j30_jetNoCut	EF_j30_jetNoEF
90 - 120	L1_J15	EF_j35_jetNoCut	EF_j35_jetNoEF
120 - 150	L1_J30	EF_j50_jetNoCut	EF_j50_jetNoEF
150 - 180	L1_J55	EF_j75_jetNoCut	EF_j75_jetNoEF
180 - 210	L1_J75	EF_j95_jetNoCut	EF_j95_jetNoEF
210 - 7000	L1_J95	EF_L1J95_NoAlg	EF_L1J95_NoAlg

Table 6.1: L1 and L2 jet triggers used to select events are shown for different dijet $\overline{p_{\mathrm{T}}}$ regions and data periods.

6.2.3 Noise and Pile-up Rejection

An event is rejected if any fake jet with $p_{\mathrm{T}} > 20$ GeV is found. Fake jets are defined as "bad" jets, which are related to noisy calorimeters, cosmic rays or beam-background, or "ugly" jets that are energy deposits from the proton-proton interaction, but have been poorly measured (often by falling into transitions between different detectors). The ugly jet cleaning criteria and the loose and medium bad jet cleaning criteria are defined in Section 3.4.

The medium jet cleaning requirement removes a large proportion of bad jets, but is inefficient for good jets. The loose jet cleaning requirement has an efficiency of $> 99\%$ for good jets, but some bad jets remain. The effects of the jet cleaning selection and the justification for using the loose bad jet requirement are shown in Section 6.4.2.

Events are only used if the number of reconstructed primary vertices is equal to one. This requirement reduces the impact of in-time pile-up. In-time pile-up

is defined as multiple proton-proton interactions in the same bunch crossing and results in additional primary vertices. The one vertex requirement is necessary to remove the impact of extra energy deposits in the rapidity region between the boundary jets, which can degrade the gap by either producing a new jet, or by increasing the p_{T} of an existing jet to greater than Q_0. The residual effect of pile-up is studied in Section 6.4.1.

6.3 Control Plots

This section presents the selected data compared to the reconstructed PYTHIA sample, to check that the PYTHIA sample approximately agrees with data. This is necessary if the MC is to be used for systematic studies and unfolding.

Figure 6.1 shows the normalised Δy distribution for (a) $70 < \overline{p_{\mathrm{T}}} < 90$ GeV, (b) $90 < \overline{p_{\mathrm{T}}} < 120$ GeV and (c) $180 < \overline{p_{\mathrm{T}}} < 210$ GeV slices. The MC and data shape agree, with differences of less than 10%. Figure 6.2 shows the normalised ${p_{\mathrm{T}}}^{veto}$ distribution, where ${p_{\mathrm{T}}}^{veto}$ is the p_{T} of the highest jet in the rapidity region bounded by the dijet system, for two different slices in Δy and $\overline{p_{\mathrm{T}}}$. The shape of the PYTHIA prediction has adequate agreement with data in both regions, with fluctuations of about 20%. The main differences are at higher p_{T} where the statistical uncertainty is higher. Figure 6.3 shows slices of the gap fraction against Δy and $\overline{p_{\mathrm{T}}}$. As a function of Δy, PYTHIA describes the data well, only deviating by $\approx$ 10% at higher Δy. As a function of $\overline{p_{\mathrm{T}}}$, PYTHIA describes the data very well for $\overline{p_{\mathrm{T}}} < 250$ GeV, after that the gap fraction for PYTHIA is $\approx$ 10% high. This regions where PYTHIA and the data agree best correspond to the regions in Figure 2.5 that should be covered by a fixed order calculations, i.e. small $log(Q/Q_0)$ and small Δy. Outside these regions, the parton shower is required to describe the additional emissions and doesn't perform as well. Overall, the three figures demonstrate reasonable agreement between the

data and the reconstructed PYTHIA sample. This was true of other control plots and the forward/backward dijet selection. Overall, there is confidence that the PYTHIA sample can be used for systematic studies and for correcting detector effects. These control plots are also published in [1].

6.4 Systematic Uncertainties

6.4.1 Jet Cleaning

The effect of jet cleaning is investigated by examining the change in the gap fraction and the inclusive distribution when using a tighter cleaning definition. The two cleaning selections used are loose and medium, which are defined in Section 3.4. The medium cleaning selection removes more bad jets than the loose cleaning selection, however it has inefficiencies for good jets at low p_{T}. The loose cleaning selection has $> 99\%$ efficiency for good jets.

Figure 6.4 shows two slices in $\overline{p_{\mathrm{T}}}$ of the inclusive distribution in Δy for the leading p_{T} dijet selection with both the loose and medium cleaning selections applied. There is $\approx 2\,\%$ reduction in statistics using the medium cleaning selection, but the shape of the distribution seems to be unchanged. For the leading p_{T} dijet selection, the gap fraction is shown as a function of $\overline{p_{\mathrm{T}}}$ in Figure 6.5 and as a function of Δy in Figure 6.6 with the two different jet cleaning definitions. The difference in the gap fraction between the two cleaning definitions is small ($< 1\%$) and within the statistical uncertainty of the samples, and more statistics are gained with the loose bad jet definition. Similar order effects are observed with the forward/backward selection. Given that there is little bias and the improvement in statistics, this is used for the remaining analysis.

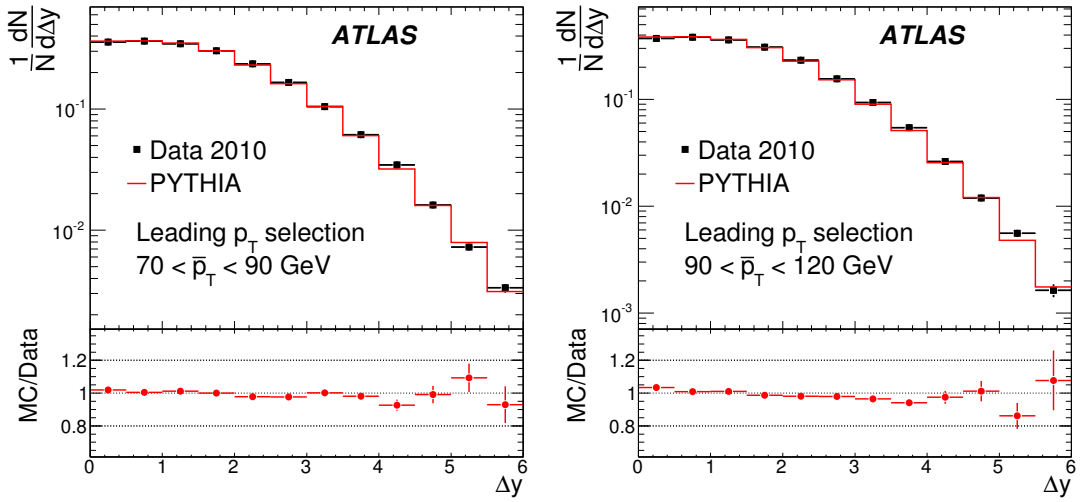

(a)

(b)

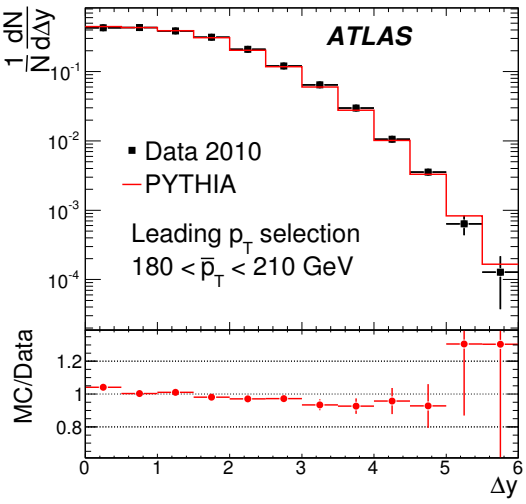

(c)

Figure 6.1: Fraction of events for each Δy bin for the 2010 data and the reconstructed PYTHIA sample for leading p_{T} dijet selection. Shown are (a) $70 < \overline{p_{\mathrm{T}}} < 90$ GeV, (b) $90 < \overline{p_{\mathrm{T}}} < 120$ GeV and (c) $210 < \overline{p_{\mathrm{T}}} < 240$ GeV slices.

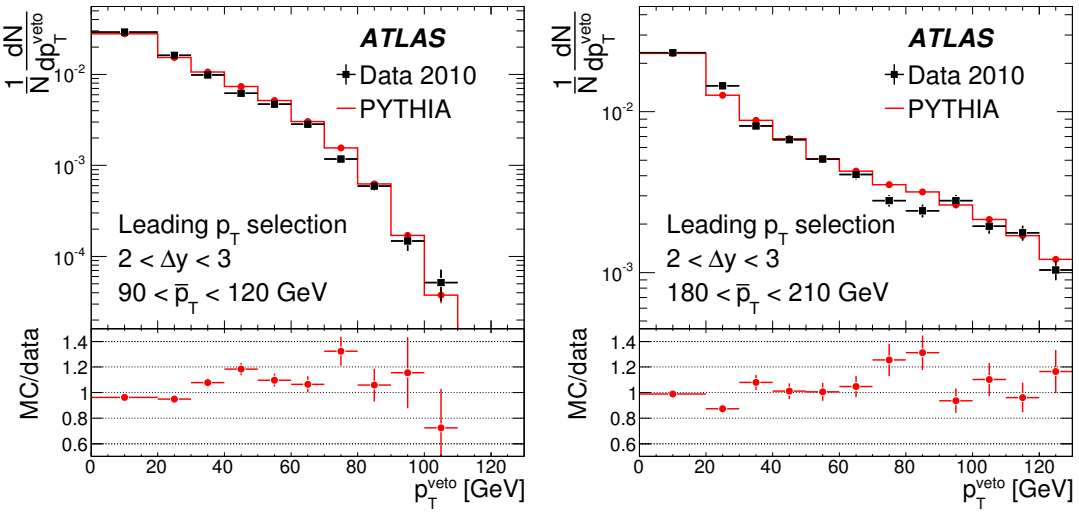

(a) (b)

Figure 6.2: Fraction of events for each p_T^{veto} bin for the 2010 data and the reconstructed PYTHIA sample, where $p_T{}^{veto}$ is the p_T of the highest jet in the rapidity region bounded by the dijet. Shown are (a) $90 < \overline{p_T} < 120$ GeV and $2 < \Delta y < 3$, and (b) $180 < \overline{p_T} < 210$ GeV and $2 < \Delta y < 3$ slices.

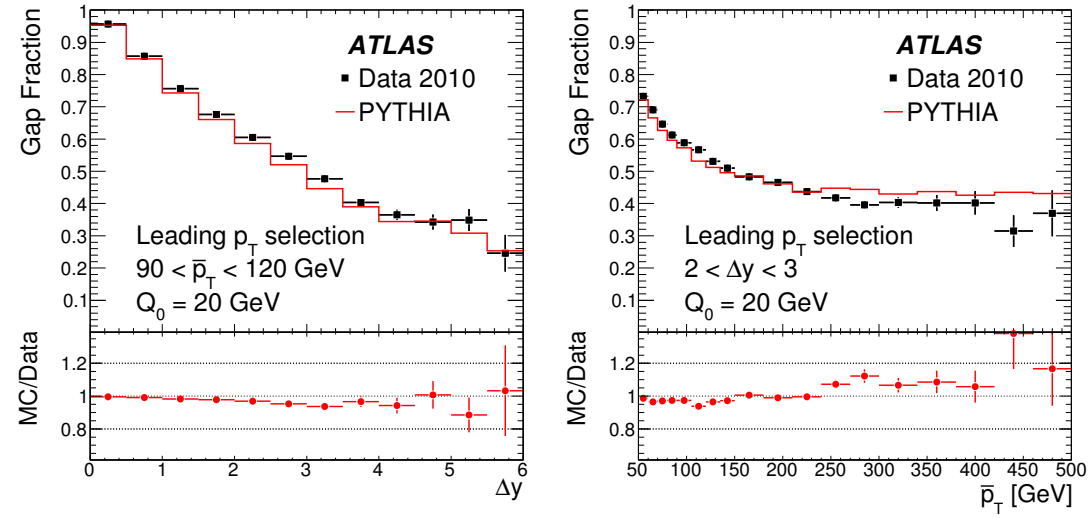

(a) (b)

Figure 6.3: Gap fraction against (a) Δy for the $90 < \overline{p_T} < 120$ GeV slice and (b) $\overline{p_T}$ for the $2 < \Delta y < 3$ slice, for the 2010 data and the PYTHIA sample for the leading p_T dijet selection.

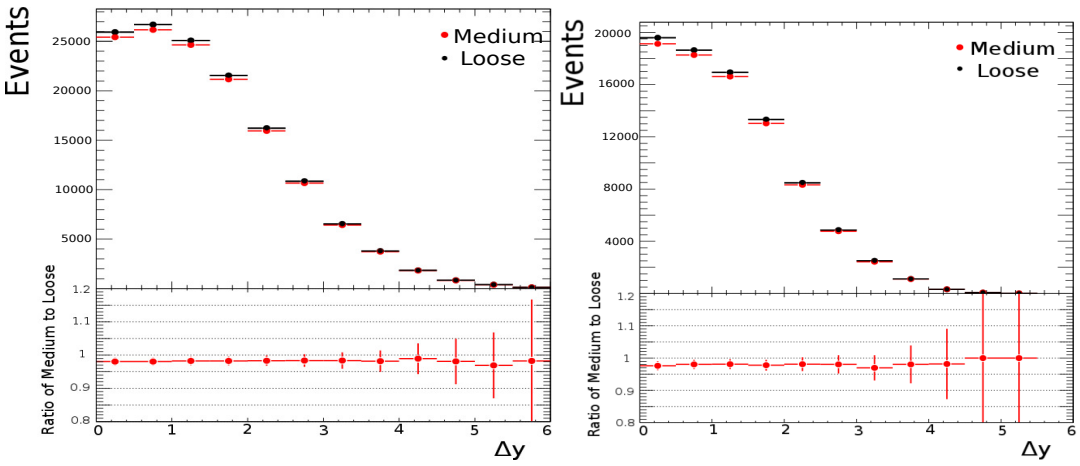

(a) (b)

Figure 6.4: Number of events for each Δy bin for medium and loose jet cleaning definitions for the leading p_{T} dijet selection. Shown are (a) $90 < \overline{p_{\mathrm{T}}} < 120$ GeV and (b) $210 < \overline{p_{\mathrm{T}}} < 240$ GeV slices. The ratio of the medium cleaning to loose cleaning is shown below the distribution. The error bars on the ratio assume uncorrelated samples, and so do not represent the statistical uncertainty in the bins.

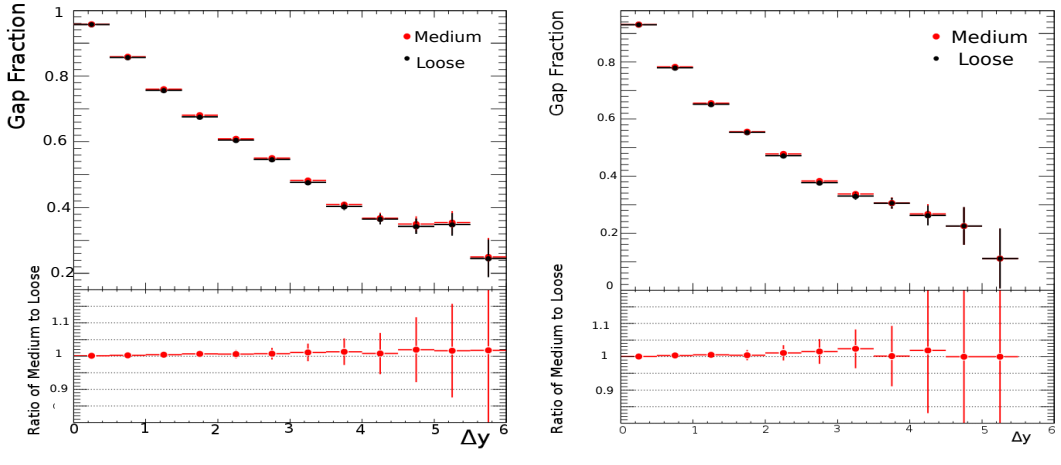

(a) (b)

Figure 6.5: Gap fraction for each Δy bin for medium and loose jet cleaning definitions for the leading p_{T} dijet selection. Shown are (a) $90 < \overline{p_{\mathrm{T}}} < 120$ GeV and (b) $210 < \overline{p_{\mathrm{T}}} < 240$ GeV slices. The ratio of the medium cleaning to loose cleaning is shown below the distribution. The error bars on the ratio assume uncorrelated samples, and so do not represent the statistical uncertainty in the bins.

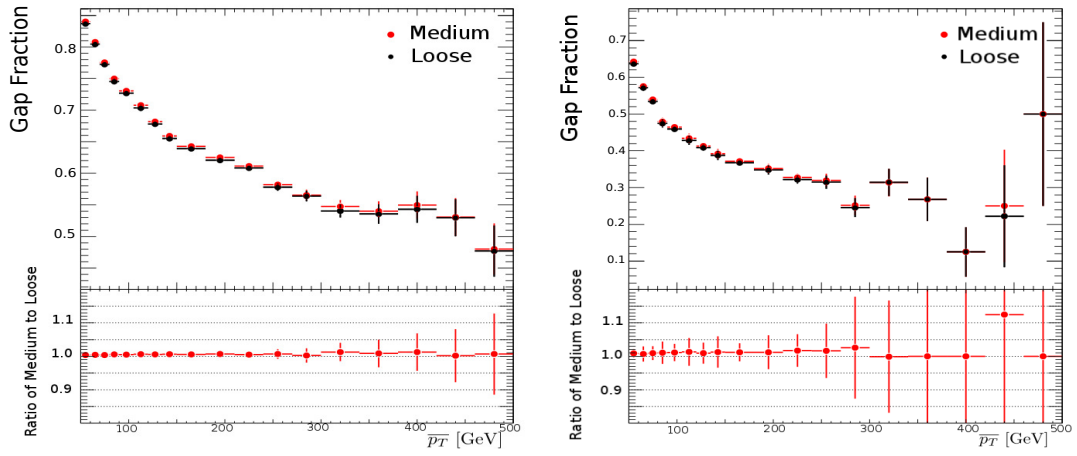

(a) (b)

Figure 6.6: Gap fraction for each $\overline{p_{\mathrm{T}}}$ bin for medium and loose jet cleaning definitions for the leading p_{T} dijet selection. Shown are (a) $1 < \Delta y < 2$ and (b) $3 < \Delta y < 4$ slices. The ratio of the medium cleaning to loose cleaning is shown below the distribution. The error bars on the ratio assume uncorrelated samples, and so do not represent the statistical uncertainty in the bins.

6.4.2 Pile-up

Two effects from pile-up are studied; in-time pile-up and out-of-time (OOT) pile-up. In-time pile-up is additional proton-proton interactions in the event and is dependent on the number of primary vertices. Out-of-time pile-up is additional energy coming from previous bunch collisions and depends on both the number of primary vertices of the previous bunches and the bunch spacing. Both have the effect of adding additional energy to the event, which can affect the gap fraction.

Requiring one primary vertex will reduce the effect of in-time pile-up. The effect of the OOT pile-up and the residual in-time pile-up are assessed by comparing the average gap fraction for different pile-up conditions. Table 6.2 shows that the average number of primary vertices for different periods increases throughout 2010 data taking. The main changes in the bunch spacing are in period E, where it was partially reduced, and in period G, where bunch trains with 150 ns bunch spacing were introduced.

The data periods are combined into two different bunch spacing conditions. In periods B-D the bunch spacing was large, and so the effect of OOT pile-up is expected to be small. In periods E-I, the bunch spacing was smaller, especially from period G onwards. It is expected that the effect of OOT pile-up will be larger in this period. The effect of OOT pile-up is assessed by considering the average gap fraction for different slices in Δy and $\overline{p_{\mathrm{T}}}$ as a function of data period. The periods B-D and E-I are separately fitted with a constant, and the differences between these fits are used to assess the effect.

To assess the residual effect from in-time pile-up, the average gap fraction for different slices in Δy and $\overline{p_{\mathrm{T}}}$ as a function of data period is fitted with

$$y = A + Bx, \tag{6.2}$$

where x is the data period. If there is no period dependence, the gradient B is consistent with zero.

Figures 6.7 - 6.9 show the average gap fraction as a function of period for various Δy and $\overline{p_{\mathrm{T}}}$ slices with fits to the two different OOT pile-up conditions, periods B-D and E-I, with a simple $y = A$ fit. Figure 6.7 shows this for a low $\overline{p_{\mathrm{T}}}$ range of 60–70 GeV for (a) $1 < \Delta y < 2$, (b) $2 < \Delta y < 3$ and (c) $3 < \Delta y < 5$. The fit for the periods EFGHI is level with the period BCD for the lowest Δy range, 0.2 above for the medium Δy range and 0.1 below for the Δy range. For this $\overline{p_{\mathrm{T}}}$ range no trend is observed. Figures 6.8 and 6.9 show a similar lack of trend and difference within 0.2. These results would indicate that there is no significant effect from OOT pile-up.

Table 6.3 shows the result of fitting the function in Equation 6.2 to the various Δy and $\overline{p_{\mathrm{T}}}$ slices. The fits from the period-dependent function show that the gradient of the line, B, is consistent, within statistical uncertainties, with zero for almost all slices. These two methods have shown that after the primary vertex cut, the effect of pile-up is negligible.

Period	$\langle N_{PV} \rangle$
B	1.07
C	1.06
D	1.57
E	1.89
F	2.18
G	2.46
H	2.33
I	2.78

Table 6.2: Average number of vertices ($\langle N_{PV} \rangle$) for the different data taking periods.

Δy	$\overline{p_{\mathrm{T}}}$	$\bar{f}_{gap}$	$y = A + Bx$		
	GeV	Periods B-D	A	$B/10^{-3}$	χ^2/NDF
1-2	60-70	0.80	0.81±0.005	-2.5±3.0	1.30
	70-90	0.76	0.76±0.005	-0.6±1.8	0.78
	90-120	0.72	0.72±0.006	-0.7±2.5	0.87
	120-150	0.67	0.67±0.010	-0.9±2.8	1.30
	150-180	0.63	0.62±0.013	3.7±2.8	1.30
2-3	60-70	0.69	0.68±0.008	9.5±4.5	1.10
	70-90	0.63	0.64±0.007	-1.1±2.7	0.49
	90-120	0.58	0.57±0.009	5.8±3.6	0.94
	120-150	0.53	0.53±0.015	-1.8±4.1	0.75
	150-180	0.49	0.46±0.019	4.3±4.1	1.70
3-5	60-70	0.55	0.54±0.011	9.4±6.3	1.60
	70-90	0.50	0.50±0.010	-1.1±3.8	0.32
	90-120	0.43	0.44±0.014	-2.3±5.3	0.60
	120-150	0.39	0.38±0.023	0.5±6.3	0.68
	150-180	0.35	0.32±0.029	7.6±6.3	1.60

Table 6.3: The results from fits to the period dependent function in Equation 6.2 for various slices of Δy and $\overline{p_{\mathrm{T}}}$.

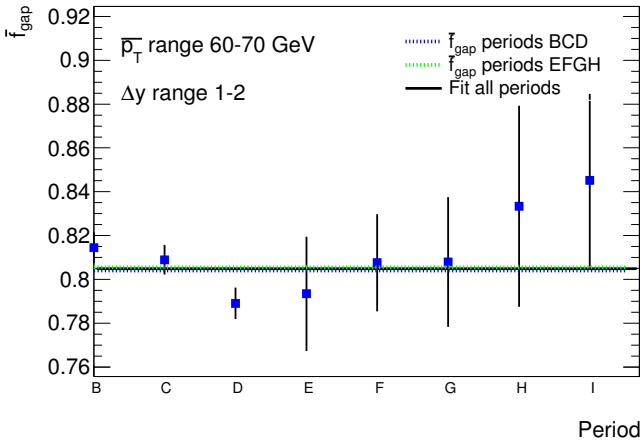

(a)

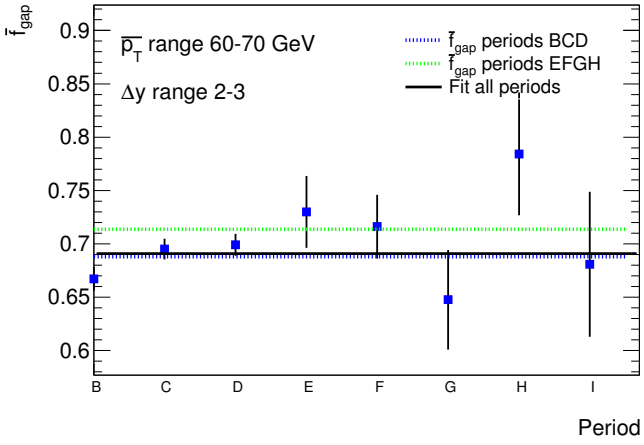

(b)

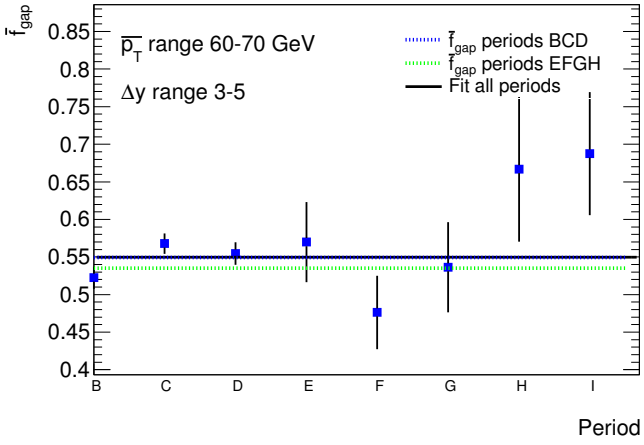

(c)

Figure 6.7: Average gap fraction with $60 < \overline{p_T} < 70$ GeV and (a) $1 < \Delta y < 2$, (b) $2 < \Delta y < 3$ and (c) $3 < \Delta y < 5$. Each set of average gap fractions have been fitted with three constants; one for periods B-D, one for periods E-I and one for all periods.

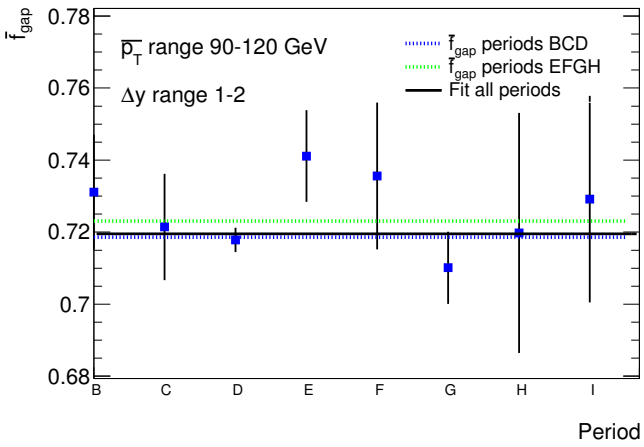

(a)

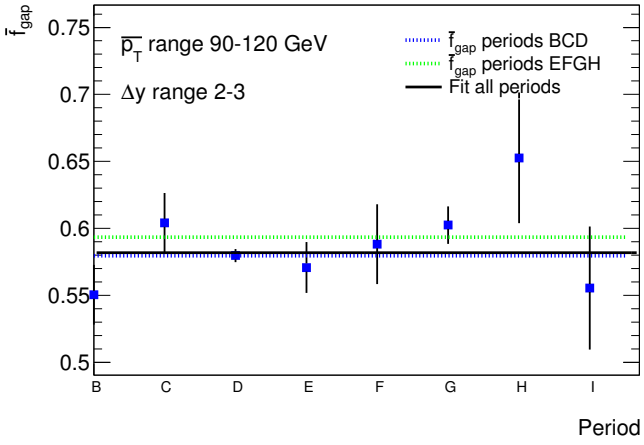

(b)

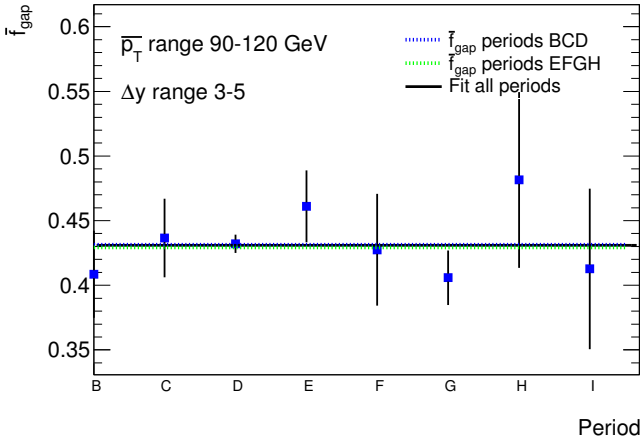

(c)

Figure 6.8: Average gap fraction with $90 < \overline{p_{\mathrm{T}}} < 120$ GeV and (a) $1 < \Delta y < 2$, (b) $2 < \Delta y < 3$ and (c) $3 < \Delta y < 5$. Each set of average gap fractions have been fitted with three constants; one for periods B-D, one for periods E-I and one for all periods.

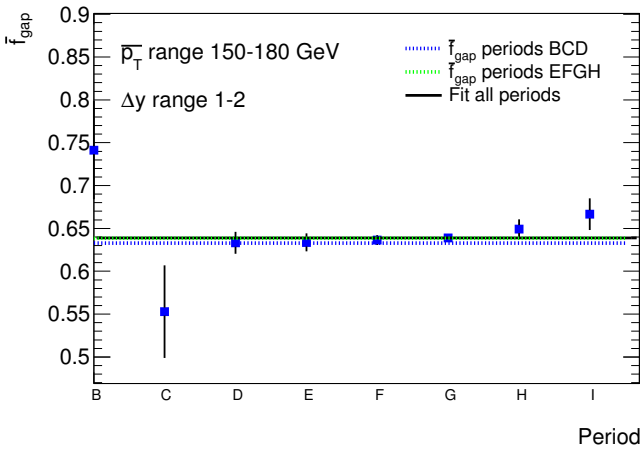

(a)

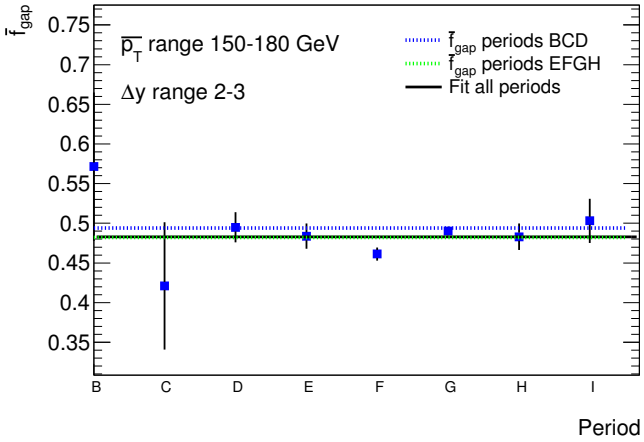

(b)

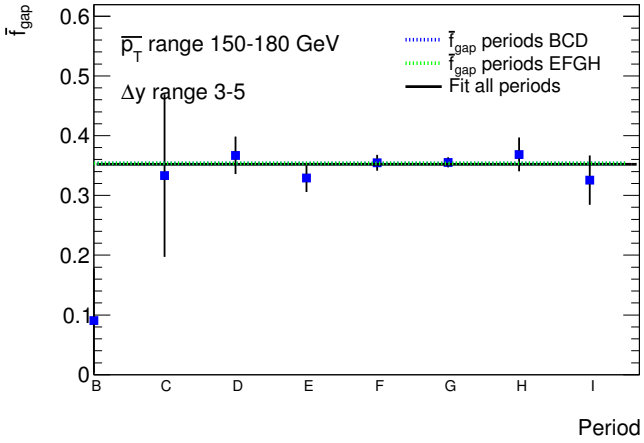

(c)

Figure 6.9: Average gap fraction with $150 < \overline{p_{\mathrm{T}}} < 180$ GeV and (a) $1 < \Delta y < 2$, (b) $2 < \Delta y < 3$ and (c) $3 < \Delta y < 5$. Each set of average gap fractions have been fitted with three constants; one for periods B-D, one for periods E-I and one for all periods.

6.5 Overview of Other Analysis Components

This section will review the unfolding of the data to hadron level and the combination of the main systematic uncertainties in this analysis will then be discussed.

Unfolding was required to produce measurements that are independent of detector effect and selection effects. This allowed the corrected data to be compared to generators and theoretical predictions which do not simulate the ATLAS detector. The data was unfolded to hadron level by using bin-by-bin unfolding. This was done by looking at the high statistics PYTHIA samples, and for each bin in the final distributions a correction factor was found from the ratio of the hadron level value to the detector level value. The correction factors were typically less than 10% [60].

The systematic uncertainties from various sources were considered by the other analysers [60]. They were:

Jet Energy Scale (JES) uncertainty varies depending on the Δy bin. It can be as large at 5-10% and is a significant source of uncertainty.

Unfolding uncertainty comes mainly from the limited statistics of the PYTHIA sample used to obtain the unfolding factors. It is a significant source of uncertainty with values as large as 5%.

Cosmic and beam backgrounds event rates were estimated using triggers during non-filled bunch crossings. The rate of such events was found to be very small compared to the rate of signal events, and the effect is taken to be negligible.

Trigger Bias was estimated by comparing the gap fraction and jet multiplicity distributions with the analysis trigger strategy to the distributions obtained using the minimum bias stream and was found to be negligible in all regions.

6.6 Corrected Data

In this section, the final plots that were shown in the publication are discussed. The plots shown are from the leading p_{T} dijet selection and the forward/backwards selection and show the gap fraction as a function of Δy, $\overline{p_{\mathrm{T}}}$ and Q_0, and also the mean number of jets in the rapidity interval as a function of Δy and $\overline{p_{\mathrm{T}}}$. When Δy and $\overline{p_{\mathrm{T}}}$ are studied, Q_0 is always at a fixed value of 20 GeV. The data are sliced into different regions. The gap fraction and mean number of jets versus Δy distributions are shown for seven different $\overline{p_{\mathrm{T}}}$ ranges, and it is shown versus $\overline{p_{\mathrm{T}}}$ for five different Δy ranges. Each slice is offset to allow the data to be shown on one plot. The ratio of the theory predictions to data is shown next to each plot.

On each plot, the black points are the data points with statistical uncertainty bars, with the yellow bands indicating the systematic uncertainty from both the JES and unfolding. The red and blue dotted lines are the POWHEG + PYTHIA and POWHEG + HERWIG predictions respectively, and the blue band is the HEJ prediction with a theoretical uncertainty.

Figures 6.10 and 6.11 show the gap fraction and the ratio of theory to data as a function of Δy and $\overline{p_{\mathrm{T}}}$, respectively, for different $\overline{p_{\mathrm{T}}}$ and Δy slices for the leading p_{T} dijet selection. The gap fraction from the data reduces as a function of $\overline{p_{\mathrm{T}}}$ and Δy. When the rapidity region between the dijets is small, the phase space for emission is small. When the Δy or the $\overline{p_{\mathrm{T}}}$ of the dijets increases, the phase space available for emission increase, and so the gap fraction decreases. For the highest $\overline{p_{\mathrm{T}}}$ range, the gap fraction starts to level off. This feature could be due to PDF effects, where both of the jets have high p_{T}, and so the probability of having another jet in the event is low. HEJ agrees well with the data for the complete range in Δy for low $\overline{p_{\mathrm{T}}}$. However, for $\overline{p_{\mathrm{T}}}$ slices $150 \leq \overline{p_{\mathrm{T}}} < 180$ GeV and above, HEJ starts to overestimate the gap fraction. This deviation is shown more clearly as a function of $\overline{p_{\mathrm{T}}}$. HEJ deviates from the data for $\overline{p_{\mathrm{T}}} > 140$ GeV

for all but the highest Δy slices, in which there are significant uncertainties. As described in Section 2.4, HEJ is designed to produce hard wide angle emissions that are rapidity ordered. Therefore, is it not unexpected that it should do better when $Q_0 \approx \overline{p_{\mathrm{T}}}$, and to do worse when $Q_0 << \overline{p_{\mathrm{T}}}$.

POWHEG + PYTHIA and POWHEG + HERWIG give significantly different gap fractions as a function of Δy and $\overline{p_{\mathrm{T}}}$. POWHEG + PYTHIA gives the best overall description of the data. POWHEG + PYTHIA agrees with the data at all $\overline{p_{\mathrm{T}}}$ slices for low Δy, however it starts to deviate for $\Delta y > 3.5$. This can also be seen for the gap fraction as a function of $\overline{p_{\mathrm{T}}}$ for the different Δy slices. For the slices, $1 \leq \Delta y < 2$, $2 \leq \Delta y < 3$, and $3 \leq \Delta y < 4$, the agreement is very good throughout $\overline{p_{\mathrm{T}}}$, with only deviations away from the data at large Δy which correspond to statistical fluctuations. However, for the other Δy slices POWHEG + PYTHIA gives too low a gap fraction. Conversely, POWHEG + HERWIG only agrees with the data only in the lowest of Δy bins, it deviates for $\Delta y > 1$ for all slices of $\overline{p_{\mathrm{T}}}$. In the gap fraction against $\overline{p_{\mathrm{T}}}$ for different Δy slices distributions, POWHEG + HERWIG does not agree well with the data and underestimates the gap fraction for all considered regions of phase space. The difference between POWHEG + PYTHIA and POWHEG + HERWIG is an indication of the uncertainty in current calculations of parton showers.

Figure 6.12 shows the gap fraction as a function of Q_0 for different slices in Δy and $\overline{p_{\mathrm{T}}}$ for the leading p_{T} dijet selection. For a low Q_0 value, the gap fraction is at a minimum, as any increase in Q_0 will reduce the number of events with a jet above Q_0. When the Q_0 increases the gap fraction increases, which is expected as the probability of getting a very high p_{T} emission is lower. POWHEG + HERWIG underestimates the data for all but the highest Q_0 bins, indicating that there is too much emission from the POWHEG + HERWIG parton shower. The gap fraction as a function of Q_0 for the slice $2 \leq \Delta y < 3$ and $70 \leq p_{\mathrm{T}} < 90$ GeV in

data is well described by both HEJ and POWHEG + PYTHIA. For the other slices, at low Q_0 HEJ overestimates the gap fraction, but improves as $Q_0 \approx \overline{p_{\mathrm{T}}}$, which is expected as HEJ generates partons with similar p_{T}. Neither POWHEG + PYTHIA or HEJ agrees well with the gap fraction when both Δy and Q_0 is large.

Figures 6.13 and 6.14 are the mean number of jets in the rapidity interval between the boundary jets as a function of Δy and $\overline{p_{\mathrm{T}}}$, respectively, for slices in $\overline{p_{\mathrm{T}}}$ and Δy for the leading p_{T} dijet selection. This is an alternative method of probing the activity between the boundary jets. The gap fraction is only concerned with the leading jet in the rapidity region, but the average number of jets considers all jet in that region with a $p_{\mathrm{T}} > 20$ GeV. As with the gap fraction, POWHEG + PYTHIA agrees best with the data. POWHEG + HERWIG consistently gives too much activity in the rapidity region, which helps to explain why the POWHEG + HERWIG gap fraction is below the data. Except at very low $\overline{p_{\mathrm{T}}}$, HEJ has too little activity in the rapidity region. Comparing to the gap fraction slices, in which it agrees with data, would indicate that HEJ describes only the highest p_{T} emission between the dijet well.

Figures 6.15 and 6.16 show the gap fraction and the ratio of theory to data as a function of Δy and $\overline{p_{\mathrm{T}}}$, respectively, for different $\overline{p_{\mathrm{T}}}$ and Δy slices for the forward/backward dijet selection. For this selection, there are often imbalances in the p_{T} of the boundary jets, especially at larger $\overline{p_{\mathrm{T}}}$. All three model comparisons show similar difference to the data. The gap fraction from HEJ as a function of Δy falls below the data for low $\overline{p_{\mathrm{T}}}$ slices. It has been suggested in [17] that this is due to the importance of soft emission from the dijets.

Figure 6.17 shows the gap fraction as a function of Q_0 for different slices in Δy and $\overline{p_{\mathrm{T}}}$ for the forward/backward dijet selection. In the leading p_{T} dijet selection, the maximum p_{T} of a jet in the rapidity region between the dijet system is the p_{T}

of the subleading jet (which has a maximum p_{T} of $\overline{p_{\mathrm{T}}}$). Above the $\overline{p_{\mathrm{T}}}$ of the jet, the gap fraction must be one. However, for the forward/backward dijet selection, the p_{T} of a jet in the rapidity region between the dijet system is less affected by the $\overline{p_{\mathrm{T}}}$. The gap fraction does not rise as quickly as in the previous selection. The POWHEG + PYTHIA shows similar agreement to the data as for the previous selection. HEJ does not agree well with the data, and especially for the higher Δy slices, it has a consistently low gap fraction throughout Q_0.

Figure 6.18 shows the gap fraction as a function of Δy and $\overline{p_{\mathrm{T}}}$ respectively for different $\overline{p_{\mathrm{T}}}$ and Δy slices for the forward/backward dijet selection, but the Q_0 is set to the $\overline{p_{\mathrm{T}}}$ of the event. This shows how the gap fraction is affected by emissions which are harder than the $\overline{p_{\mathrm{T}}}$ of the dijets. POWHEG + PYTHIA and POWHEG + HERWIG both overlap the data. This would indicate that this definition of the gap fraction is less dependent on the modelling of the parton shower, hadronisation and underlying event. The new definition of the jet veto does not improve the HEJ agreement with the data.

Since publishing the results of this analysis, several papers [17, 61–65] have compared their theoretical predictions to the ATLAS data. Reference [65] uses an all-order resummation in $\ln(p_{\mathrm{T}}/Q_0)$ terms to compare to the data, observing a large theoretical uncertainty. The conclusion of the paper is: "The message is clear: the accuracy of the ATLAS data already demands better theoretical calculations". The CMS collaboration has measured the fraction of events with exactly two jets to events with two or more jets [66]. This is equivalent to the inverse of the gap fraction for the forward-backward selection, and while it cannot be quantitatively compared, they agree qualitatively.

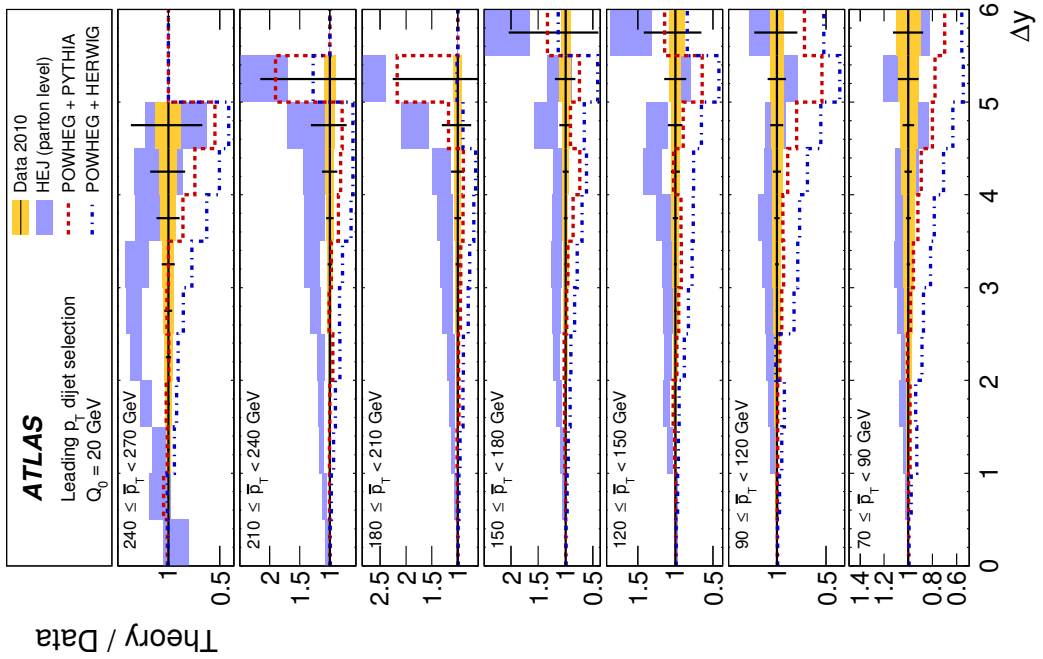

(b)

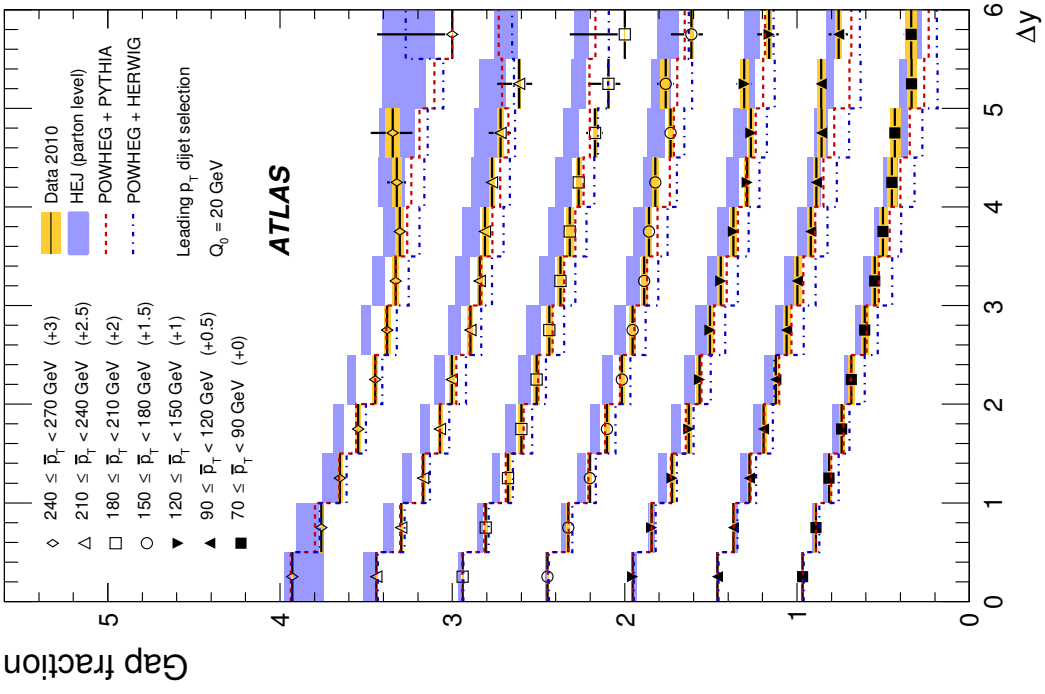

(a)

Figure 6.10: (a) Gap fraction as a function of Δy for various $\overline{p_{\mathrm{T}}}$ slices for the leading p_{T} dijet selection. (b) Ratio of the gap fractions between the theoretical predictions and the data as a function of Δy.

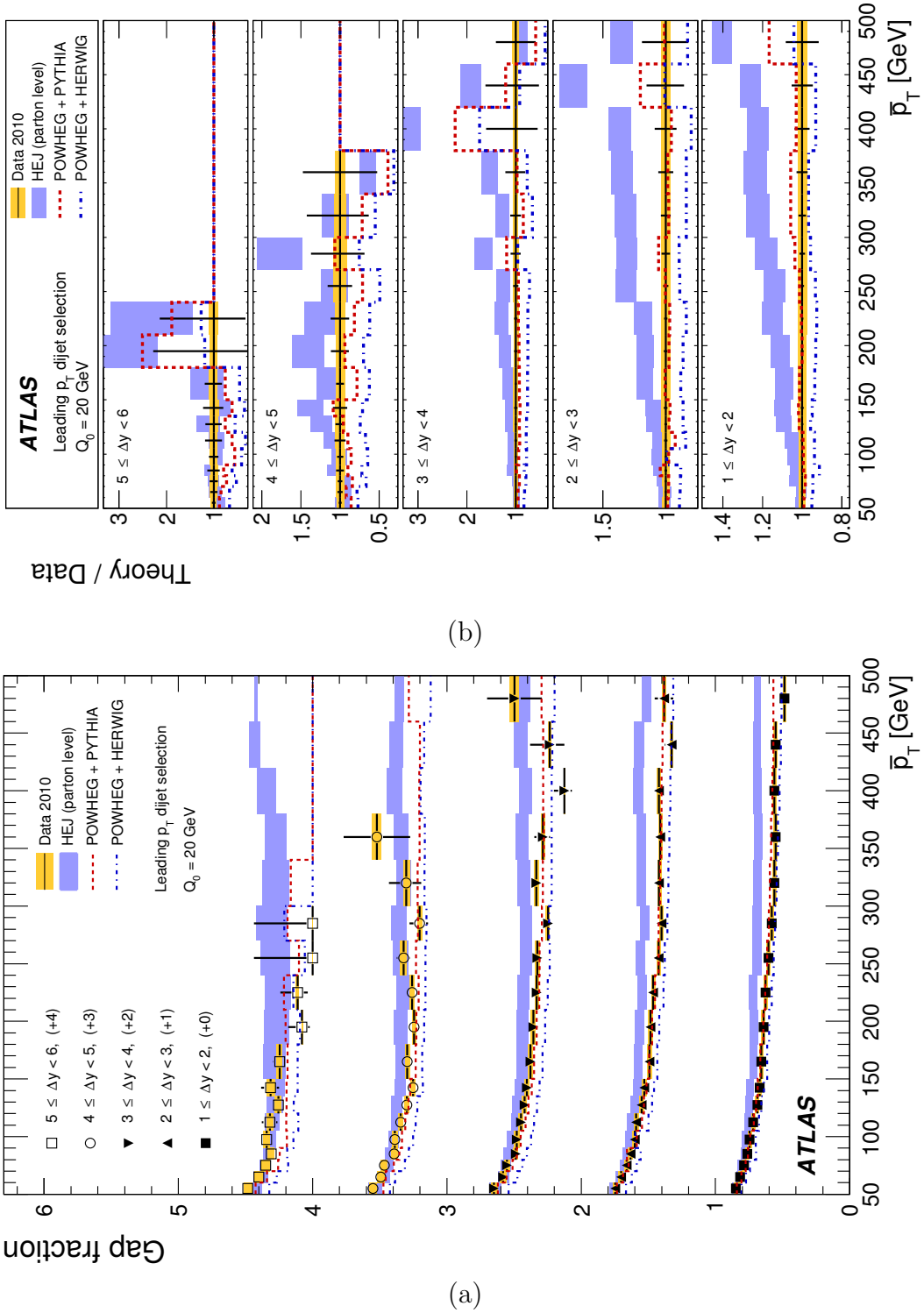

Figure 6.11: (a) Gap fraction as a function of $\overline{p_{\mathrm{T}}}$ for various Δy slices for the leading p_{T} dijet selection. (b) Ratio of the gap fractions between the theoretical predictions and the data as a function of $\overline{p_{\mathrm{T}}}$.

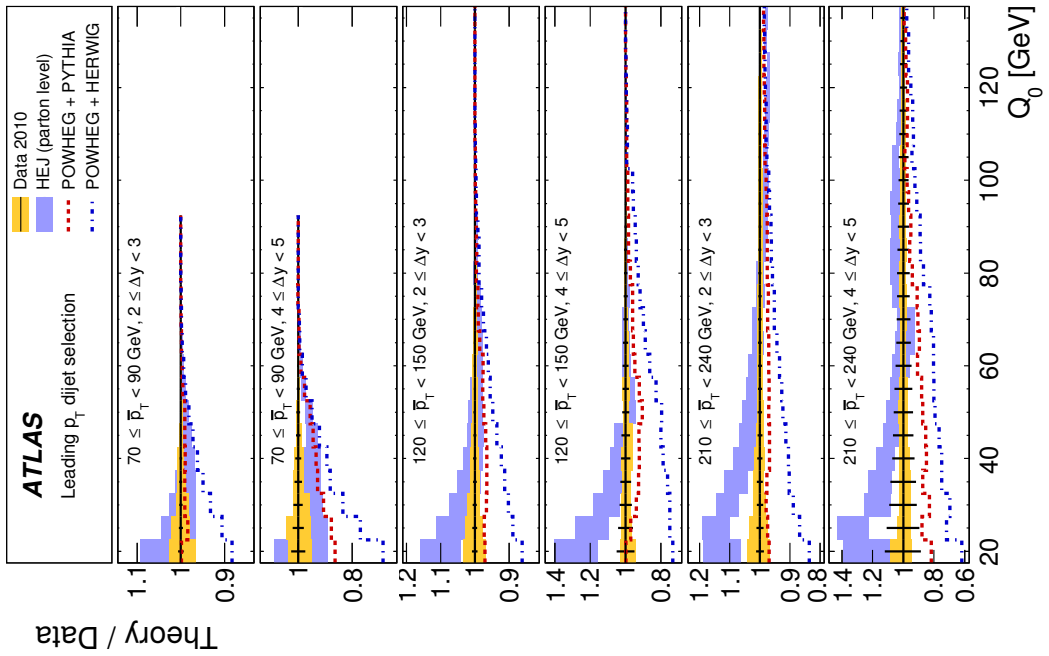

(b)

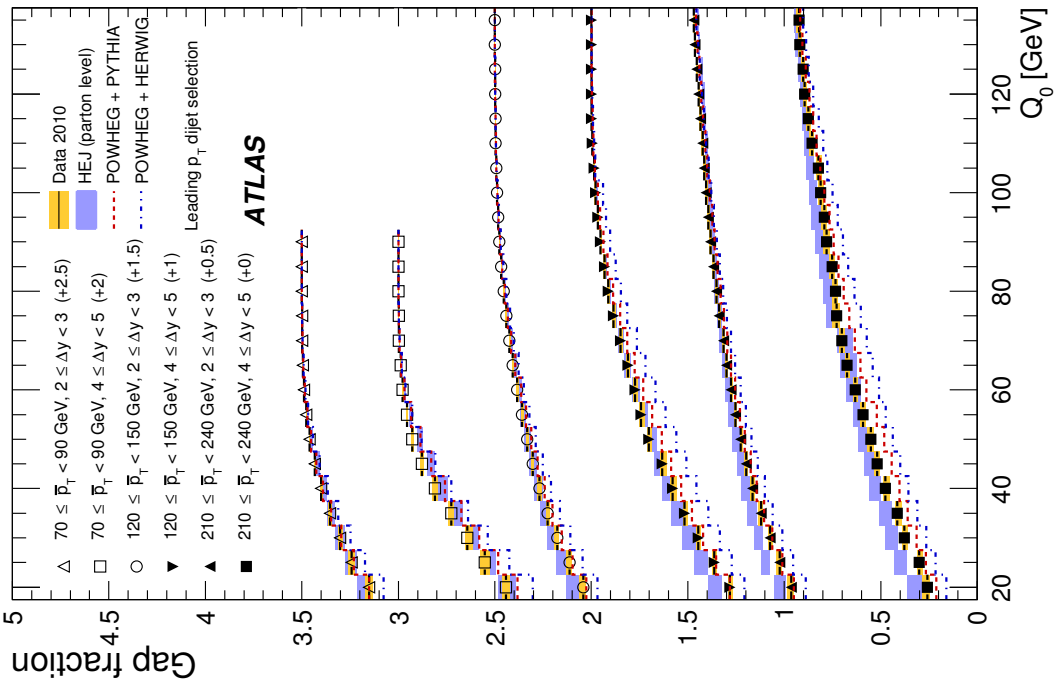

(a)

Figure 6.12: (a) Gap fraction as a function of Q_0 for various Δy and $\overline{p_T}$ slices for the leading p_T dijet selection. (b) Ratio between the theoretical predictions and data.

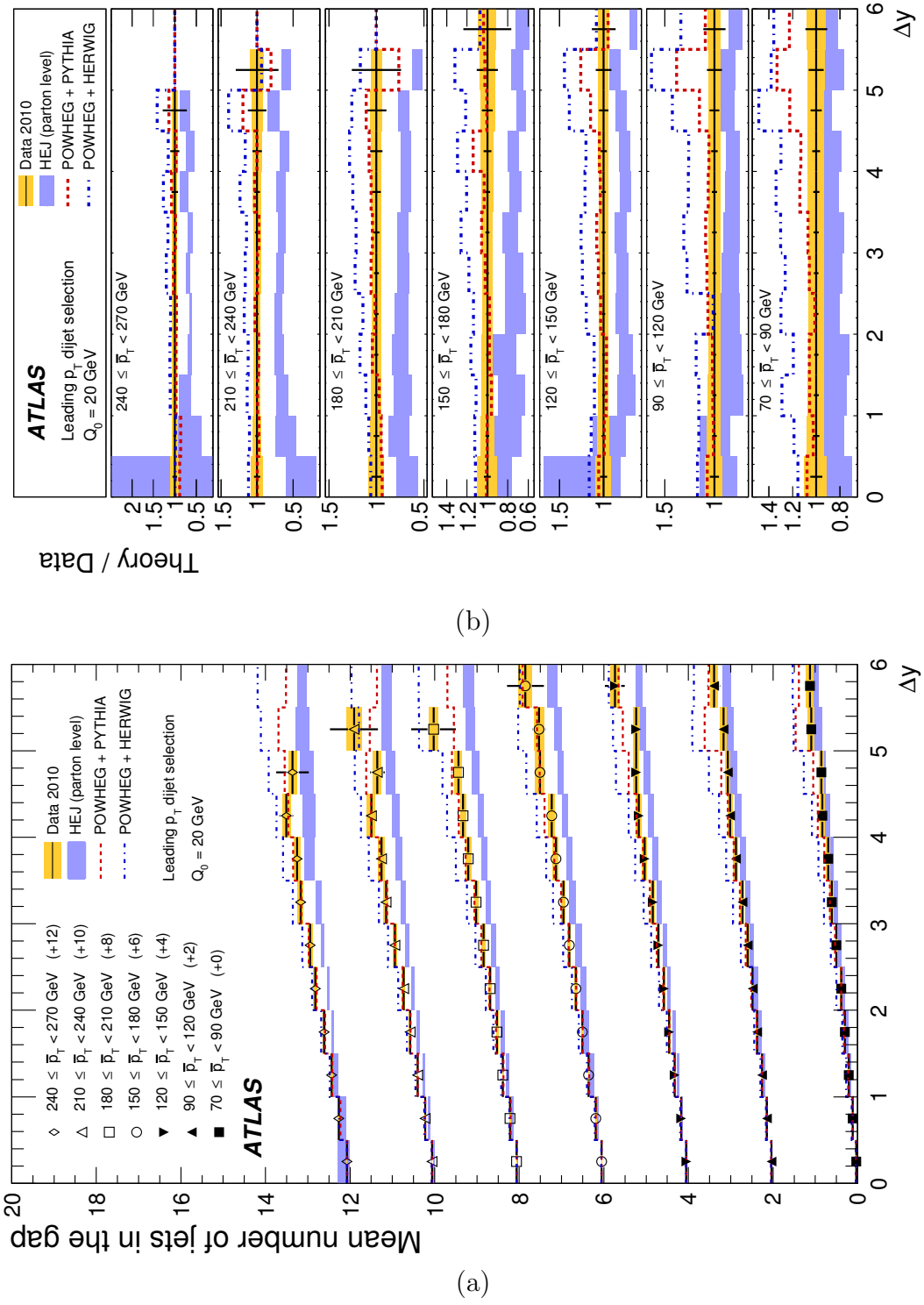

Figure 6.13: (a) Mean number of jets in the rapidity region bounded by the dijet system as a function of Δy for various $\overline{p_{\mathrm{T}}}$ slices for the leading p_{T} dijet selection. (b) Ratio of the mean number of jets between the theoretical predictions and the data as a function of Δy.

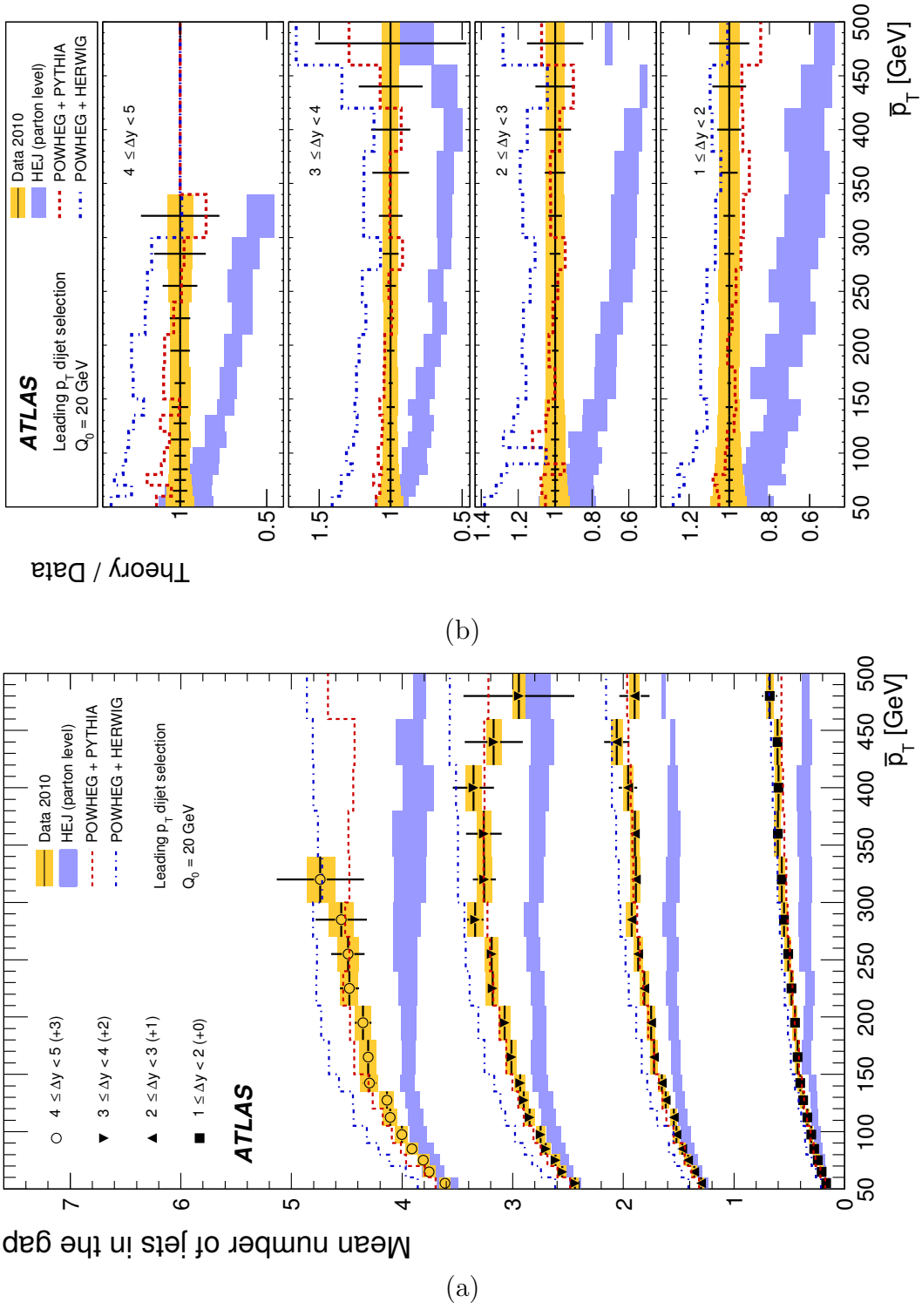

Figure 6.14: (a) Mean number of jets in the rapidity region bounded by the dijet system as a function of $\overline{p_T}$ for various Δy slices for the leading p_T dijet selection. (b) Ratio of the mean number of jets between the theoretical predictions and the data as a function of $\overline{p_T}$.

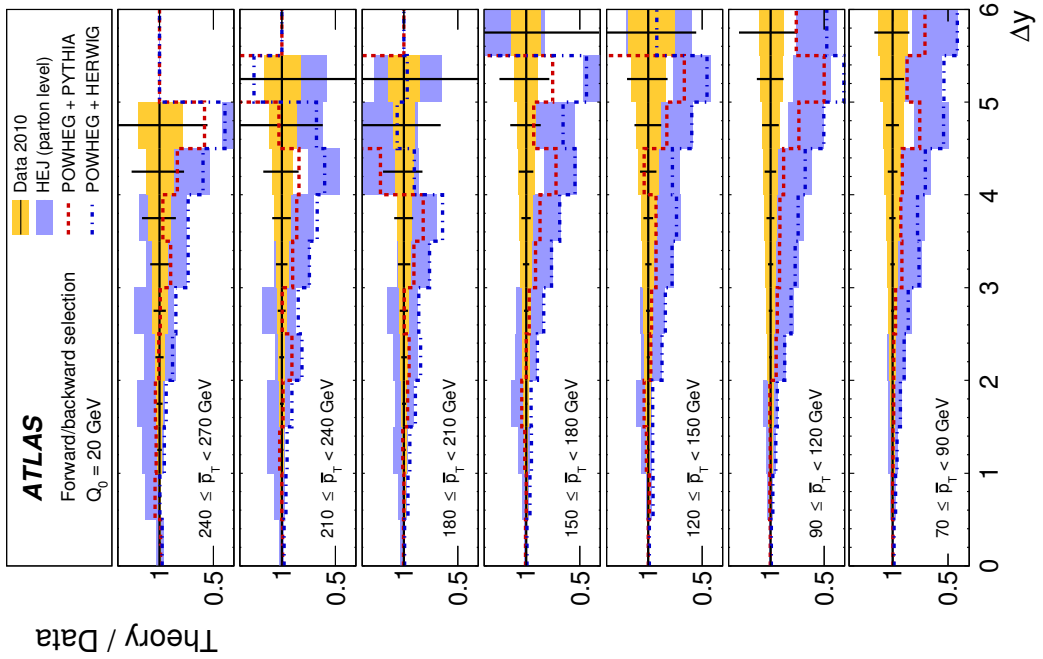

(b)

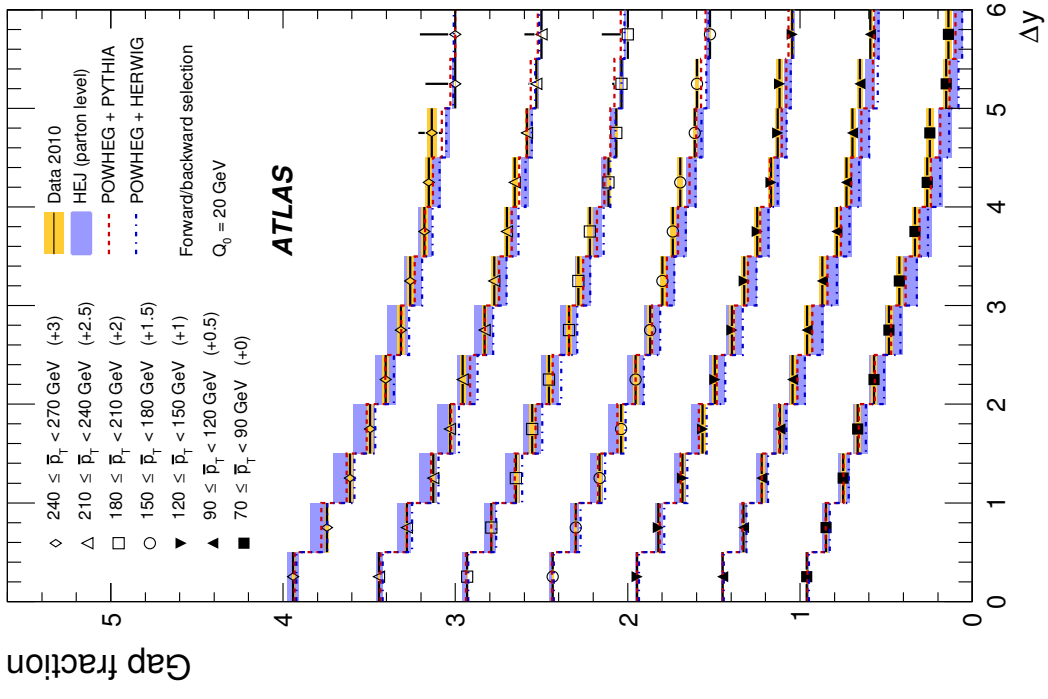

(a)

Figure 6.15: (a) Gap fraction as a function of Δy for various $\overline{p_{\mathrm{T}}}$ slices for the forward backward selection. (b) Ratio of the gap fractions between the theoretical predictions and the data as a function of Δy.

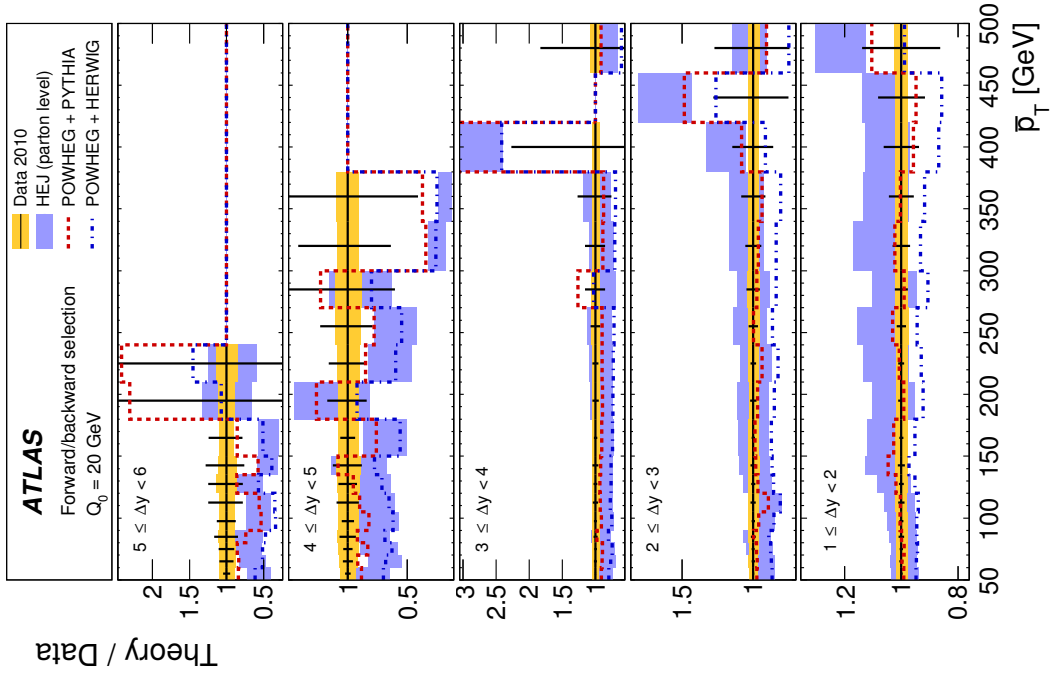

(b)

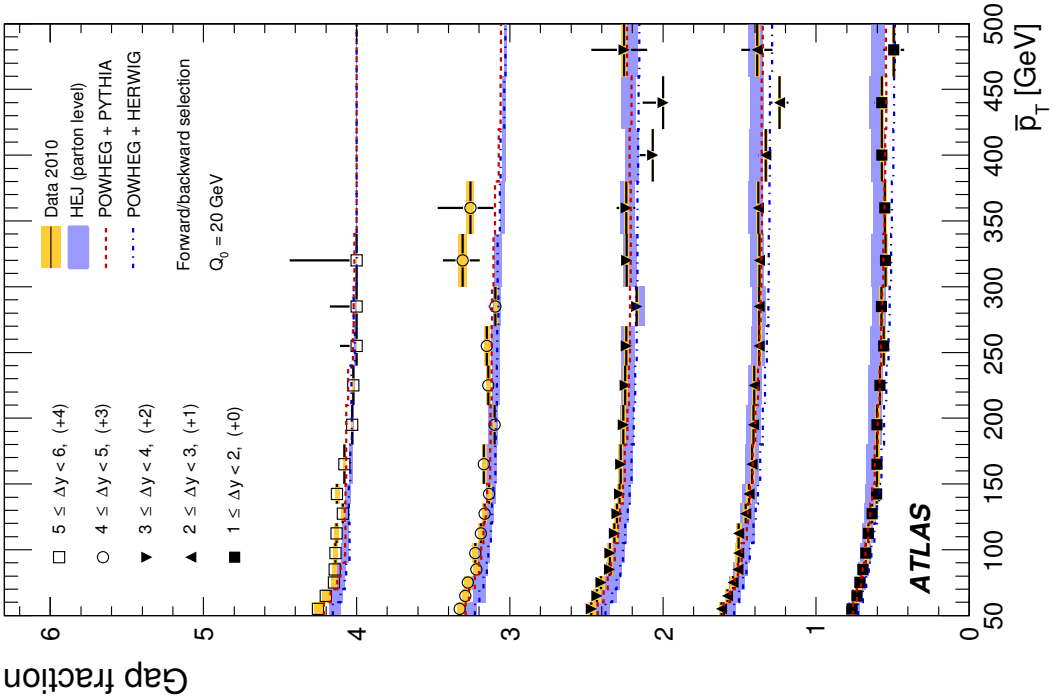

(a)

Figure 6.16: (a) Gap fraction as a function of $\overline{p_T}$ for various Δy slices for the forward backward selection. (b) Ratio of the gap fractions between the theoretical predictions and the data as a function of $\overline{p_T}$.

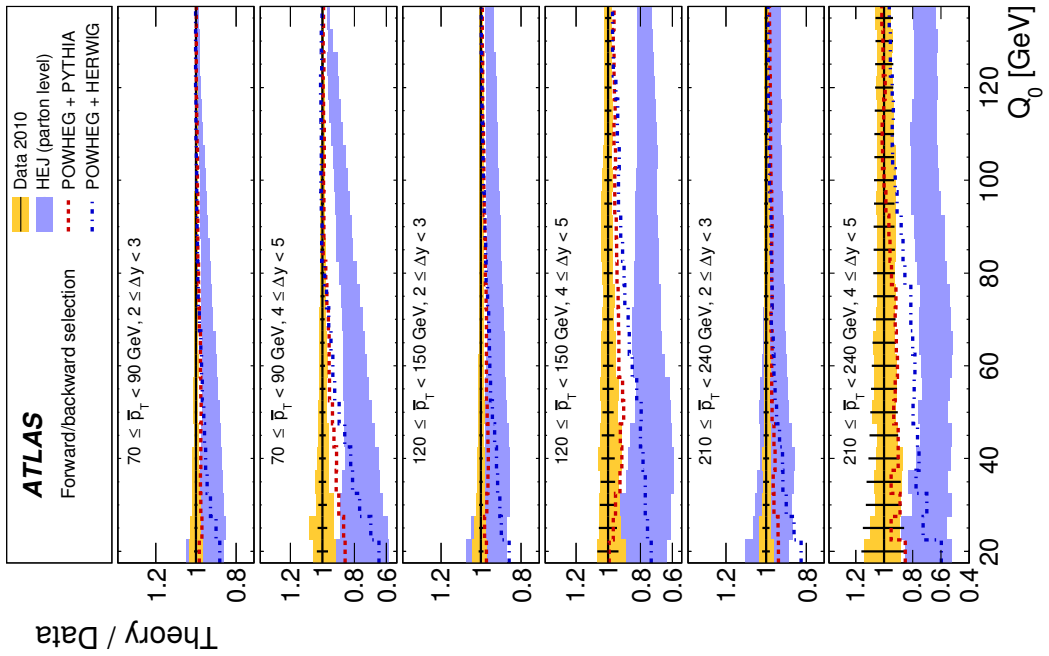

(b)

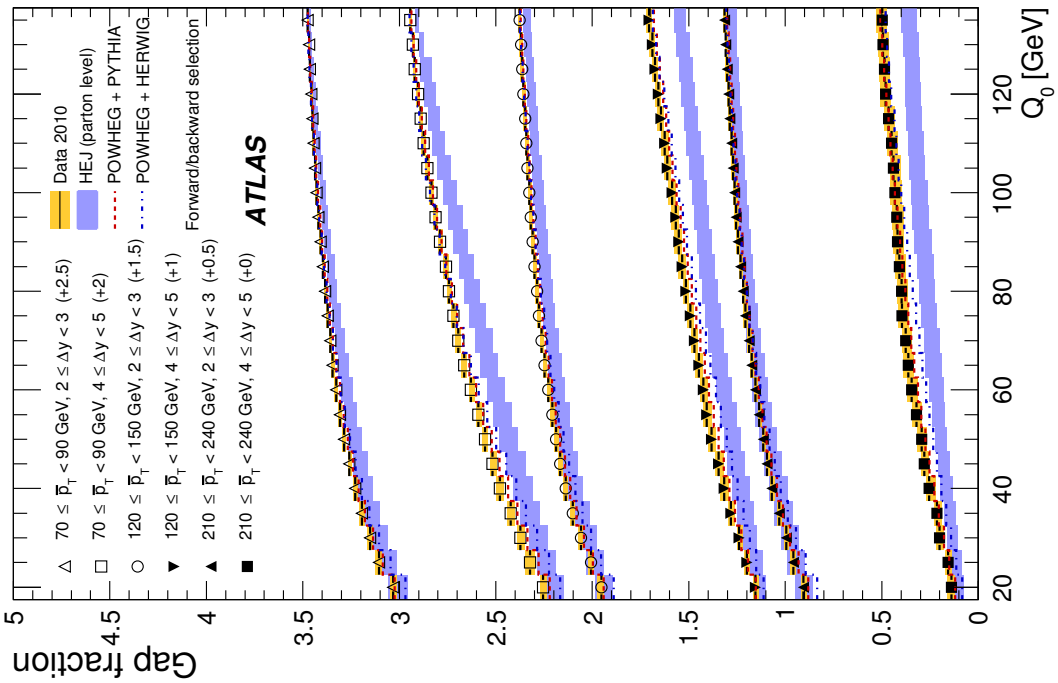

(a)

Figure 6.17: (a) Gap fraction as a function of Q_0 for various Δy and $\overline{p_{\mathrm{T}}}$ slices for the forward backward selection. (b) Ratio of the gap fractions between the theoretical predictions and the data as a function of Q_0.

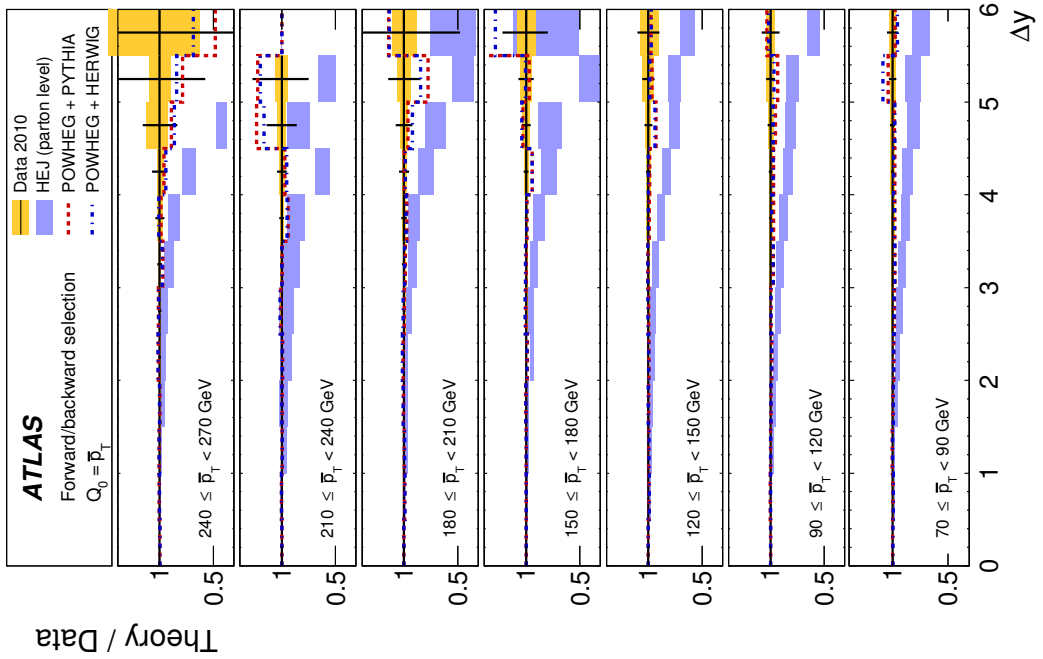

(b)

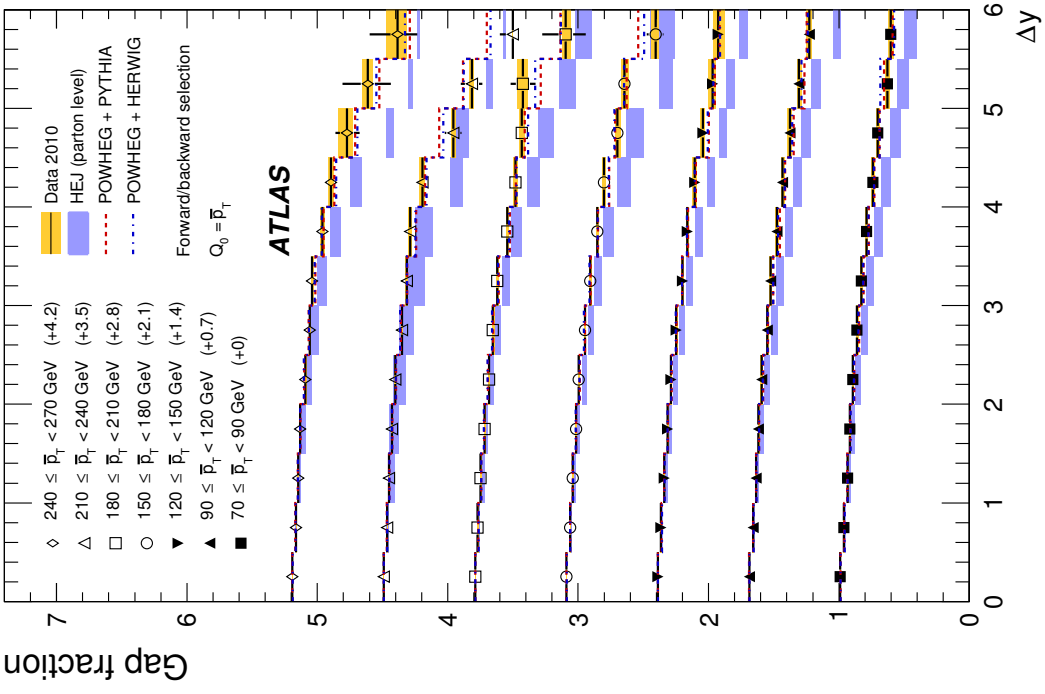

(a)

Figure 6.18: (a) Gap fraction as a function of Δy for various $\overline{p_{\mathrm{T}}}$ slices for the forward backward selection with veto scale set as $\overline{p_{\mathrm{T}}}$. (b) Ratio of the gap fractions between the theoretical predictions and the data as a function of Δy.

Chapter 7

Dijets with a Jet Veto and Azimuthal Decorrelations at Very Large Rapidity Separations

The first LHC measurement of dijet production with a jet veto (documented in Chapter 6 and [1]) examined the gap fraction in slices $\overline{p_{\mathrm{T}}}$ up to $\Delta y = 6$. This cut-off in Δy is necessary because the analysis uses a central jet trigger strategy in which the trigger fires if a jet is within $|y| < 2.8$. There is a relatively small number of events at large Δy and the statistical uncertainties are large. The data are compared to theory predictions by HEJ and POWHEG.

The analysis is extended to probe the gap fraction at a larger Δy region. This larger Δy region is again studied using the 2010 data, but using a new dijet trigger strategy that allows measurements up to $\Delta y = 8$, which is the boundary of the detector. In addition, the effect of quark/gluon emission from the dijet system is studied using the azimuthal decorrelation between the jets that make up the dijet system. The previous ATLAS measurement of azimuthal decorrelation was carried out using jets with $|y| < 0.8$ [67]. Measurements of the azimuthal

decorrelation using a normalised dijet cross section were reported by CMS and D0 collaborations [68, 69].

7.1 Topology Selection

The jets used in this analysis are reconstructed from EM scale calorimeter clusters with the anti$-k_T$ algorithm, described in Section 2.3, using $R = 0.6$. As for the previous analysis, jets that have $p_{\mathrm{T}} > 20$ GeV and $|y| < 4.4$ are used, as these have a well defined jet energy scale and jet cleaning cuts. The dijet system is defined by the two leading jets in the event, with cuts on the transverse momentum of the leading and sub-leading jets of $p_{\mathrm{T}} > 60$ GeV and $p_{\mathrm{T}} > 50$ GeV, respectively.

The observables studied can be divided into azimuthal decorrelation observables, and jet veto observables. The jet veto observables are the same as defined in the previous chapter, where the gap fraction, f_{gap}, is defined by,

$$f_{\mathrm{gap}} = \frac{N(Q_0)}{N}, \tag{7.1}$$

where $N(Q_0)$ is the number of gap events that do not contain a jet with $p_{\mathrm{T}} > Q_0$ in the rapidity interval between the boundary jets and N is the inclusive number of events. The gap fraction is studied as a function of Δy and Q_0. The mean number of jets, $\bar{N}$, found in the rapidity region between the dijets that have $p_{\mathrm{T}} > Q_0$ is also studied. The azimuthal decorrelation variables are

$$\frac{d\sigma}{d\Delta\phi},\ \langle\cos(\pi - \Delta\phi)\rangle \text{ and } \langle\cos(2\Delta\phi)\rangle. \tag{7.2}$$

The cross-section as a function of $\Delta\phi$ is measured in slices of Δy. The decorrelation variables, ($\langle\cos(\pi - \Delta\phi)\rangle$ and $\langle\cos(2\Delta\phi)\rangle$), are studied as a function of Δy. All decorrelation variables are studied separately for inclusive and gap events (those that survived a jet veto). The standard jet veto scale that is used to define gap events is $Q_0 = 20$ GeV.

7.2 Event selection

7.2.1 Data Samples and Basic Event Selection

The analysis is performed using pp collisions at $\sqrt{s} = 7$ TeV, recorded between April and October 2010 using the ATLAS detector. Stable beam conditions and good data quality is required; the data quality was assessed by the ATLAS performance working groups by checking that all the parts of the detector and trigger were performing normally, and the physics objects (for instance jets and muons) were being correctly reconstructed. Events are rejected if there is any jet with $p_T > 20$ GeV that is found as either bad or ugly as described in Section 3.4. Events are also rejected if the number of reconstructed primary vertices is not equal to one.

7.2.2 Trigger Strategy

For each of the two leading offline jets, a specific trigger chain is assigned depending on the rapidity y and p_{T} of the offline jet as well as the run number. Tables 7.1, 7.2 and 7.3 show the trigger chains assigned to jets in the central ($|y| < 2.9$), forward transition ($3.3 \leq |y| < 3.6$) and forward trigger regions ($3.6 \leq |y| < 4.4$), respectively. If a jet falls into the region $2.9 \leq |y| < 3.3$, the offline jet is matched to the closest L1 trigger jet using $\Delta\mathrm{R} = \sqrt{(\Delta\phi)^2 + (\Delta\eta)^2}$. It is defined as a central (forward) jet if it is closest to a trigger jet that fired a central (forward) jet trigger, and the trigger chain is subsequently defined using Table 7.1 (Table 7.2). Either of the trigger chains associated with the leading jets are required to fire for the event to pass.

This trigger strategy has previously been used in the measurement of the dijet cross-section [9]. In most regions of phase space, the trigger efficiency for each considered jet is 100%. However, there are two regions in which that is not the

case. The first is the crack region, $1.3 \leq |y| \leq 1.6$, between the barrel and end-cap calorimeter. The second is in the positive FCAL region in which there is a dead trigger tower that reduces the trigger efficiency for jets with $|y| > 3.1$. For each jet that falls into one of these regions, the event is weighted by

$$W_{eff} = \frac{\mathcal{P}_{lead}}{\epsilon_{lead}} + \frac{\mathcal{P}_{sublead}}{\epsilon_{sublead}} - \frac{\mathcal{P}_{lead}\mathcal{P}_{sublead}}{\epsilon_{lead}\epsilon_{sublead}} \tag{7.3}$$

where $\mathcal{P}_{lead}$ and $\mathcal{P}_{sublead}$ is 1 if the event passed the leading and subleading trigger chain, else it is zero, and ϵ_{lead} and $\epsilon_{sublead}$ are their p_{T} dependent efficiencies for the leading and subleading jets. The efficiencies are taken from the analysis in [9].

During data taking, prescales are applied to the jet trigger to preferentially select events with higher p_{T} jets; only the highest p_{T} trigger is unprescaled. The end result is a flattening of the jet p_{T} spectrum. To retrieve the original distribution, the events are weighted by the inverse of an effective luminosity for each trigger combination. The effective luminosity is calculated by

$$\mathcal{L}_{eff} = \sum_{LB} \frac{\mathcal{L}_{LB}}{P^{L}_{LB}P^{SL}_{LB}/(P^{L}_{LB} + P^{SL}_{LB} - 1)} \tag{7.4}$$

where P^{L}_{LB} and P^{SL}_{LB} are the prescales for a given luminosity for the trigger chain associated with the leading and subleading jet, respectively, and $\mathcal{L}_{LB}$ is the luminosity for the luminosity block.

The effective luminosities were calculated in [9] for all pile-up conditions. In this analysis, a single vertex cut is applied, which effectively reduces the luminosity $\mathcal{L}_{LB}$ in Equation 7.4 by a factor f_L. A single vertex correction is derived for this analysis, defined as

$$f_L = \frac{N_{SV}}{N_{ALL}}, \tag{7.5}$$

where N_{SV} is the number of events with only one vertex and N_{ALL} is the total number of events, for every trigger combination. The effective luminosity, $\mathcal{L}_{eff}$, is then weighted by f_L^{-1} to return the correct luminosity for the measurement.

p_{T} [GeV]	Period A-C	Period D-F	Period G-I
20–42.5	L1_MBTS_1	L1_MBTS_1	EF_mbMbts_1_eff
42.5–70	L1_J5	L1_J5	EF_j20_jetNoEF
70–97.5	L1_J15	L1_J15	EF_j35_jetNoEF
97.5–152.5	L1_J30	L1_J30	EF_j50_jetNoEF
152.5–197.5	L1_J55	L1_J55	EF_j75_jetNoEF
197.5–217.5	L1_J55	L1_J55	EF_j95_jetNoEF
217.5+	L1_J55	L1_J55	EF_L1J95_NoAlg

Table 7.1: Trigger chains used for central trigger region, $|y| < 2.9$, for jet p_{T} and period.

p_{T} [GeV]	Period A-D	Period E-F	Period G-I
20–42.5	L1_MBTS_1	L1_MBTS_1	EF_mbMbts_1_eff
42.5–62.5	L1_MBTS_1	L1_FJ10	EF_mbMbts_1_eff
62.5–72.5	L1_MBTS_1	L1_FJ10	EF_fj30_jetNoEF
72.5–95	L1_MBTS_1	L1_FJ30	EF_fj30_jetNoEF
95–160	L1_MBTS_1	L1_FJ30	EF_fj50_jetNoEF
160+	L1_MBTS_1	L1_FJ30	EF_fj75_jetNoEF

Table 7.2: Trigger chains used for transition trigger region, $3.3 \leq |y| < 3.6$, for jet p_{T} and period.

p_{T} [GeV]	Period A-D	Period E-F	Period G-I
20–42.5	L1_MBTS_1	L1_FJ10	EF_mbMbts_1_eff
42.5–50	L1_MBTS_1	L1_FJ10	EF_fj30_jetNoEF
50–67.5	L1_MBTS_1	L1_FJ30	EF_fj30_jetNoEF
67.5–100	L1_MBTS_1	L1_FJ30	EF_fj50_jetNoEF
100+	L1_MBTS_1	L1_FJ30	EF_fj75_jetNoEF

Table 7.3: Trigger chains used for forward trigger region, $3.6 \leq |y| < 4.4$, for jet p_{T} and period.

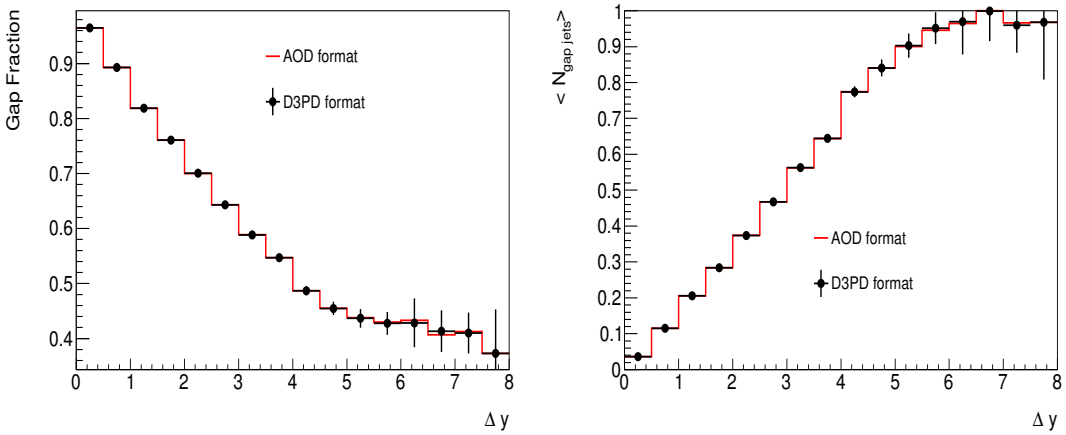

Figure 7.1: (a) Gap fraction and (b) average number of jets in the rapidity region as a function of dijet separation, Δy, for 2010 uncorrected data from the AOD (red) and D3PD (black) data formats.

7.3 Closure of Event Selection

To check the event selection, two separate implementations of the analysis were performed by the Manchester and UCL groups. One of these analyses was carried out using the ATLAS AOD data format, whilst the other used the ATLAS D3PD format. Figure 7.1 shows (a) the gap fraction and (b) the average number of jets in the rapidity region as a function of Δy. Both plots show very good agreement between the AOD and D3PD implementations of the analysis. The small disagreements arise from the data compression algorithms that store the data information. This affects mainly the jet energies and the effect is much smaller than the JES uncertainty.

7.4 Systematic Uncertainty

In this section, the systematic uncertainties from the jet cleaning cuts, jet energy scale uncertainty, jet energy resolution and jet ϕ resolution are assessed. These uncertainties are added in quadrature with other uncertainties calculated by other members of the analysis team to form the final uncertainty.

7.4.1 Jet Energy Scale Uncertainty

The effect of the uncertainty in the JES, explained in Section 3.4, is studied using the reconstructed PYTHIA samples. Each jet, which is at the central value of the JES by default, is shifted up and down by 1 standard deviation of the uncertainty on the JES. The events are then passed through the event selection and three sets of the final distributions are made corresponding to nominal JES, JES shifted up and JES shift down. The JES uncertainty band was found by taking the ratio of the shifted distribution to the nominal distribution.

Figures 7.2 - 7.5 show the JES uncertainty bands for the final distributions. The JES uncertainty shifting has two main effects that will apply differently in different distributions, one shifting the leading jet energy, and the other shifting the non-leading jets. The shift in the leading jets energy has the effect of moving events across the p_{T} cuts at 60 GeV and 50 GeV. This results in more events for JES shifted up and less events for JES shifted down. The effect of shifting the p_{T} of the non-leading jets is mainly due to the shifting of the highest p_{T} jet in the rapidity region bounded by the dijet system. This will affect distributions that probe non-leading jets, such as gap fraction or average number of jets.

The JES uncertainty band for the gap fraction as a function of Δy is shown in Figure 7.2 (a), and is small for low Δy, but increases at larger Δy. The effect of shifting up the JES for the leading jets is to include dijet events that have a lower $\overline{p_{\mathrm{T}}}$. As seen in the previous analysis (Figure 6.11), dijets with lower $\overline{p_{\mathrm{T}}}$ have a higher gap fraction, and so the effect of the upwards shift is to increase the gap fraction. Shifting up the JES of the non-leading jets increase the probability that there is a jet with $p_{\mathrm{T}} > Q_0$ in the rapidity region, and so decreases the gap fraction. At low Δy the the effect is small and the two effects cancel. At higher Δy the leading jets are more likely to be at a higher rapidity where the JES uncertainty is higher, the effects no longer cancel and the gap fraction increases.

Figure 7.2 (b) shows the JES uncertainty band for the average number of jets in the rapidity region and the overall uncertainty is approximately constant at $\pm 10\%$.

Figure 7.3 shows the JES uncertainty bands for $d\sigma/d\Delta\phi$ for both the inclusive and gap events, for the different Δy ranges. The uncertainty bands for $d\sigma/d\Delta\phi$ are significantly larger than for other distributions, with $20-30\%$ uncertainty for the $2 < \Delta y < 3$ and $4 < \Delta y < 5$, and up to 50% uncertainty for $7 < \Delta y < 8$ in the lowest $\Delta\phi$ bin. The reason that shifting the JES affects the $d\sigma/d\Delta\phi$ more than the gap fraction or average number of jets is due to the steepness of the curves in $\overline{p_{\mathrm{T}}}$. The shape of gap fraction and average number of jets against $\overline{p_{\mathrm{T}}}$ is relatively shallow compared to the steeply falling cross-section against $\overline{p_{\mathrm{T}}}$, and so there is more migration across the p_{T} cut causing the JES smearing to have larger effect on the cross-section. For the $2 < \Delta y < 3$ and $4 < \Delta y < 5$ ranges, the JES uncertainty band increases marginally for lower $\Delta\phi$. For the $7 < \Delta y < 8$ range the JES uncertainty band has a larger increase for low $\Delta\phi$.

The $\langle\cos(\pi - \Delta\phi)\rangle$ and $\langle\cos(2\Delta\phi)\rangle$ JES uncertainty bands are shown as a function of Δy in Figure 7.4 (a) and (b), respectively. The JES uncertainty affects the inclusive events more than the gap events in both the distributions, and in the inclusive events the effect grows as a function of dijet rapidity separation. The maximum effect of the JES uncertainty on the $\langle\cos(\pi - \Delta\phi)\rangle$ is around 2% for the inclusive events, and less than 0.5% for the gap events. For the $\langle\cos(2\Delta\phi)\rangle$ distributions the maximum effect from the JES uncertainty is around 4% for the inclusive events, and less than 1% for the gap events. The shape of the inclusive JES uncertainties for $\langle\cos(\pi - \Delta\phi)\rangle$ and $\langle\cos(2\Delta\phi)\rangle$ can be understood from the JES uncertainty on the $d\sigma/d\Delta\phi$. When the JES is smeared up in $d\sigma/d\Delta\phi$, for the low Δy slices the shape does not change very much. However, in the larger Δy slices the distribution now has more low $\Delta\phi$ dijets. The effect of this on the

$\langle\cos(\pi - \Delta\phi)\rangle$ and $\langle\cos(2\Delta\phi)\rangle$ is that at low Δy there should be little change, but at large Δy the change should be larger.

Figure 7.5 shows the JES uncertainty bands for the gap fraction as a function of the jet veto scale, Q_0, for (a) $2 < \Delta y < 3$, (b) $4 < \Delta y < 5$, and (c) $7 < \Delta y < 8$. The uncertainty bands increase for larger Δy. The maximum uncertainty for the $2 < \Delta y < 3$, $4 < \Delta y < 5$, and $7 < \Delta y < 8$ slices is $\approx 3\%$, $\approx 6\%$ and $\approx 8\%$, respectively. The uncertainty bands are largest at low Q_0 and reduce to zero for larger Q_0. At large values of Q_0 the gap fraction is 1, and there are few jets with p_{T} close to Q_0, and so the shifted third jet is unlikely to go above the Q_0 and change the gap fraction. Conversely, at low Q_0 the gap fraction will not be 1, and there will be many jets with a p_{T} near the Q_0 cut, thus the shifted third jet p_{T} can move across Q_0 changing the gap fraction.

7.4.2 Jet Energy Resolution

The effect from the jet energy resolution (JER) is assessed by smearing the energy in every jet in an event using a Gaussian function with the width given by the measured JER, as described in Section 3.4, which depends on the jet p_{T} and η. The analysis is then repeated using the smeared jets and the ratios of the final plots were used to see the effect compared to the unsmeared sample. The smearing procedure is repeated ten times and an average of all curves is the final effect of JER. This averaging reduced the effect of statistical fluctuations in some bins. The reconstructed PYTHIA sample is used due to the larger statistics compared to data. This method assesses the effect of an increase in JER. Reducing the JER is not possible, so a symmetric uncertainty band is constructed from the results of the increased JER.

Figures 7.6 – 7.8 show the ratios of the final distributions from the smeared jets and from the nominal jets. The ratio for the gap fraction, mean number of

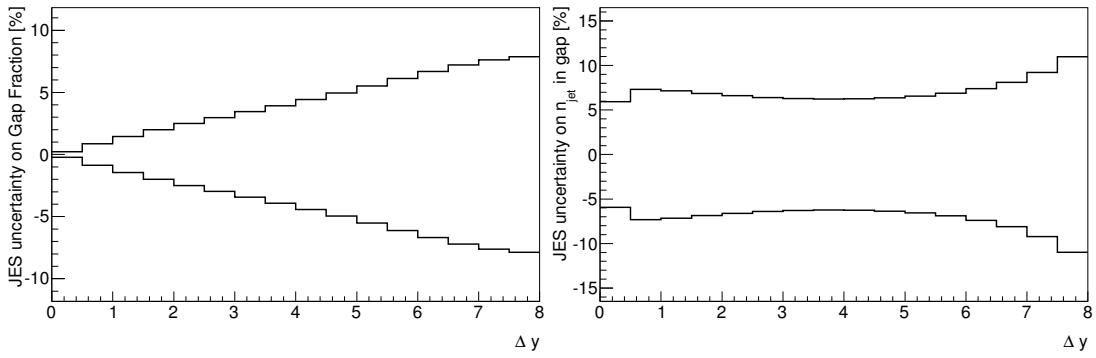

(a) (b)

Figure 7.2: The uncertainty on the (a) gap fraction and (b) mean number of jets in the rapidity interval due to the JES uncertainty as a function of dijet rapidity separation.

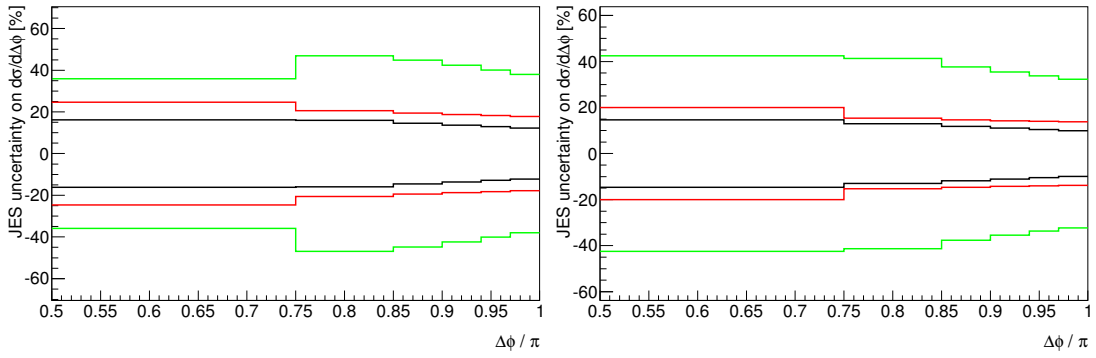

(a) (b)

Figure 7.3: The uncertainty on $d\sigma/d\Delta\phi$ due to the JES uncertainty for (a) inclusive events and (b) gap events. Three dijets rapidity separation slices are shown, $2 < \Delta y < 3$ in black, $4 < \Delta y < 5$ in red and $7 < \Delta y < 8$ in green.

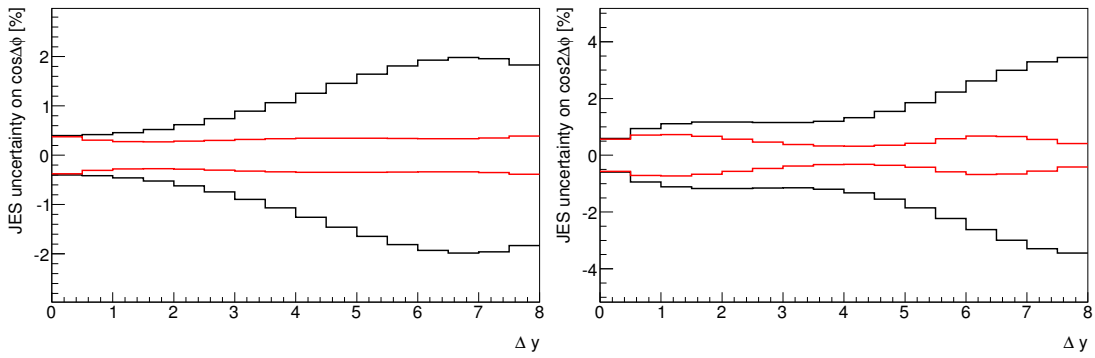

(a) (b)

Figure 7.4: The shape uncertainty on (a) $\langle\cos(\pi - \Delta\phi)\rangle$ and (b) $\langle\cos(2\Delta\phi)\rangle$ distributions due to the JES uncertainty as a function of dijet rapidity separation. The gap events are plotted in red and the inclusive events in black.

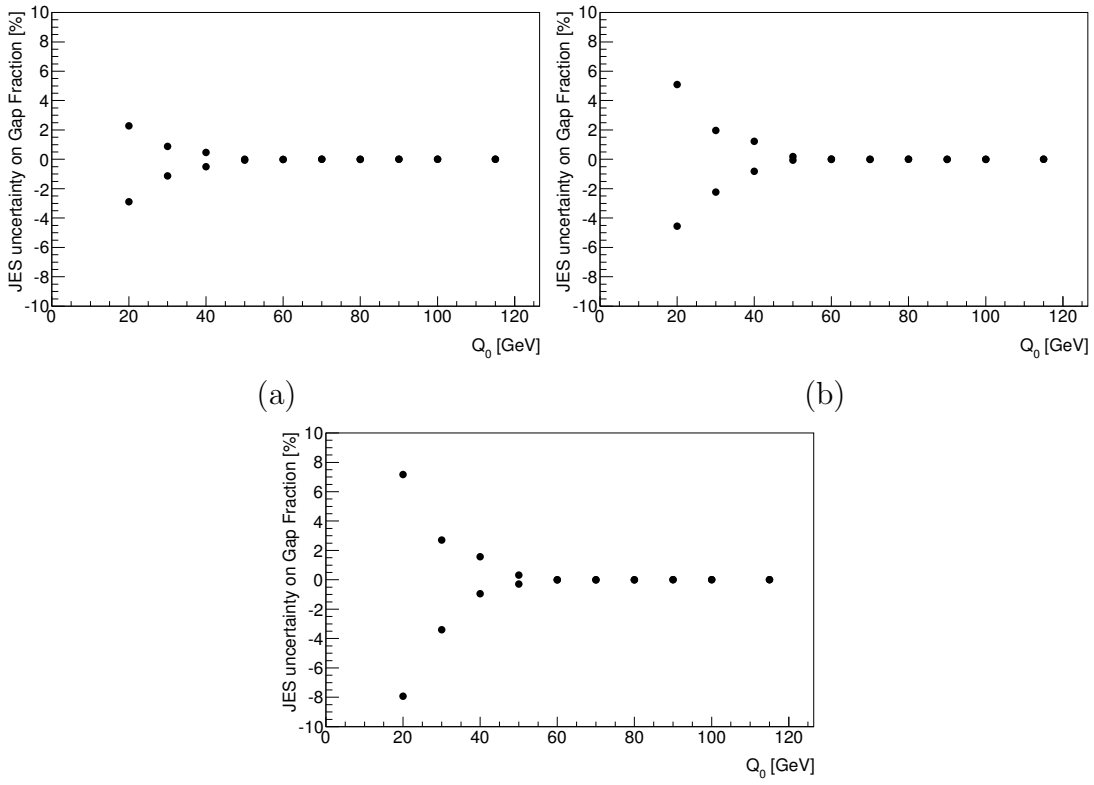

(a) (b)

(c)

Figure 7.5: The uncertainty on the gap fraction due to the JES uncertainty as a function of Q_0 for dijet rapidity separation (a) $2 < \Delta y < 3$, (b) $4 < \Delta y < 5$, and (c) $7 < \Delta y < 8$.

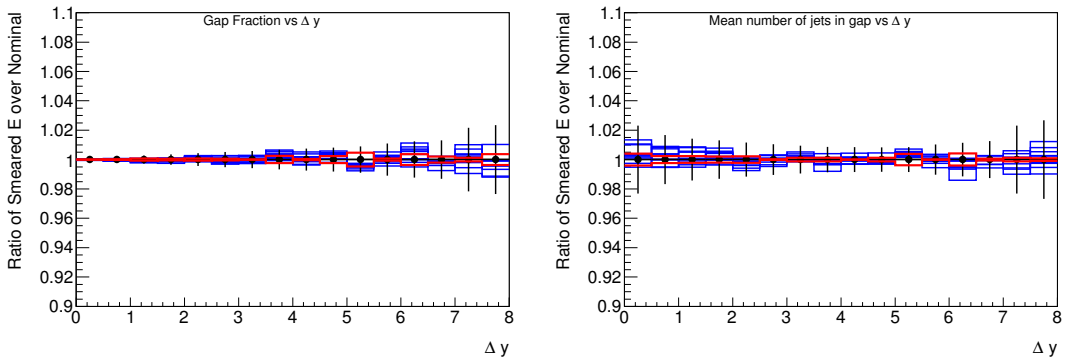

(a) (b)

Figure 7.6: The ratio of (a) the gap fraction and (b) the mean number of jets in the rapidity region between the dijet as a function of Δy for the nominal reconstructed PYTHIA sample compared to energy-smeared sample. The blue histograms represent the ten implementations of the increased JER, the two red histograms show the uncertainty band found from the average of the blue histograms, and the black points show the PYTHIA statistical uncertainties.

jets, $\cos(\pi - \Delta\phi)$ and $\cos(2\Delta\phi)$ as a function of Δy all show variations of less than 1%. The effect of the JER smearing on the gap fraction as a function of Q_0 has been found to be less than 0.5%. The ratio for the $d\sigma/d\Delta\phi$ for $2 < \Delta y < 3$ and $4 < \Delta y < 5$ using the gap and inclusive sample show variations of less than 2% except in the initial $\Delta\phi$ bin, where the statistical uncertainty is large. The effect of the JER smearing on $d\sigma/d\Delta\phi$ for $7 < \Delta y < 8$ using the inclusive sample is of the order of 2%. For the gap sample, the effect of the JER smearing can get large, especially in the low $\Delta\phi$ bins. Ignoring the two lowest $\Delta\phi$ bins, which do not have any data events in them, the uncertainty does not exceed 2%.

7.4.3 Jet ϕ Resolution

The effect of the jet ϕ resolution is assessed by smearing every jet's ϕ in the event by a Gaussian function, with the width found by comparing the ϕ of truth and reconstructed jets, which is calculated by another member of the analysis team. This method is an overestimate of the ϕ resolution uncertainty (ie 100%

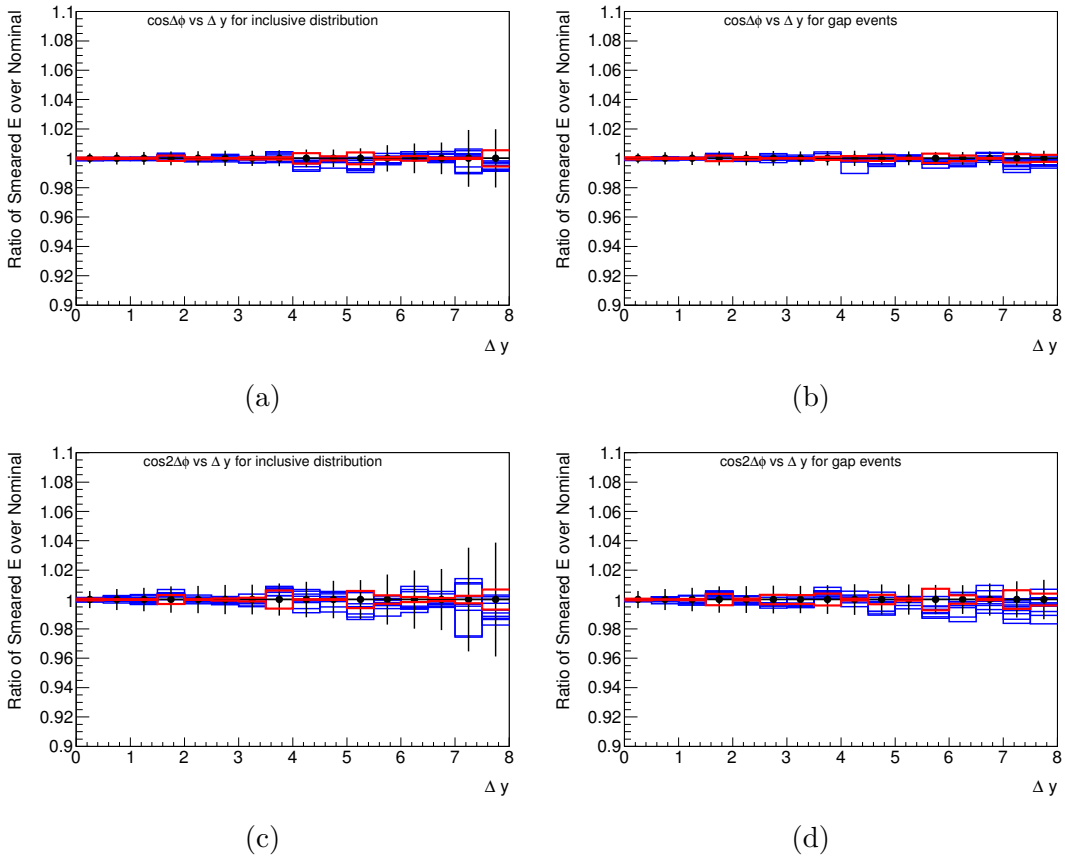

Figure 7.7: The ratio of the energy-smeared reconstructed PYTHIA sample to the nominal reconstructed PYTHIA sample of (a,b) $\langle\cos(\pi - \Delta\phi)\rangle$ and (c,d) $\langle\cos(2\Delta\phi)\rangle$ as a function of Δy using the (a,c) inclusive and (b,d) gap samples. The blue histograms represent the ten implementations of the increased JER, the two red histograms show the uncertainty band found from the average of the blue histograms, and the black points show the PYTHIA statistical uncertainties.

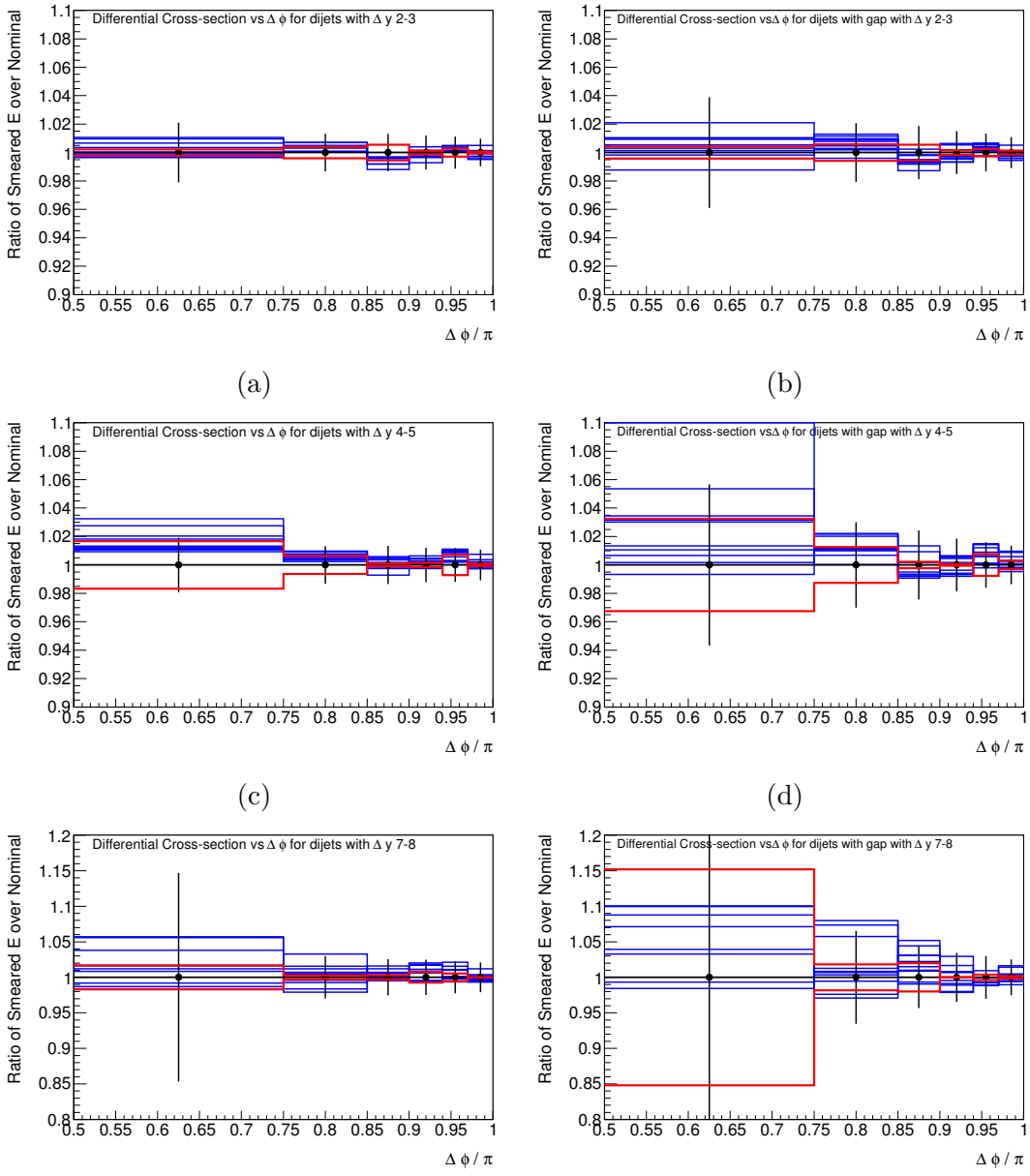

Figure 7.8: The ratio of the energy-smeared reconstructed PYTHIA sample to the nominal reconstructed PYTHIA sample of the $d\sigma/d\Delta\phi$ distribution for (a,b) $2 < \Delta y < 3$, (c,d) $5 < \Delta y < 6$ and (e,f) $7 < \Delta y < 8$ using the (a,c,e) inclusive and (b,d,f) gap samples. The blue histograms represent the ten implementations of the increased JER, the two red histograms show the uncertainty band found from the average of the blue histograms, and the black points show the PYTHIA statistical uncertainties.

uncertainty), but a data-driven method is not available in the forward region. The effect is assessed in the same way as in Section 7.4.2, using multiple smears and taking the average to reduce fluctuations. As no cuts are dependent on ϕ, only distributions that are ϕ–dependent are affected.

Figures 7.9 – 7.10 show the ratio of the final distributions of the jets smeared by the Gaussian function to the nominal jets. The effect of the increased ϕ smearing on $\langle\cos(\pi - \Delta\phi)\rangle$, for both the gap and inclusive samples, is a reduction of about 1% at low Δy. At larger Δy the effect becomes small. The same change is observed in $\langle\cos(2\Delta\phi)\rangle$, however the reduction at low Δy is about 2%.

In all the $d\sigma/d\Delta\phi$ ratios, the highest $\Delta\phi$ bin loses events that migrate into the other $\Delta\phi$ bins. This is due to the boundary of $\Delta\phi$ at π, and the steeply falling $\Delta\phi$ distribution. The uncertainty due to the ϕ resolution is around 5%, 3% and 2% for $2 < \Delta y < 3$, $4 < \Delta y < 5$ and $7 < \Delta y < 8$, respectively, with the inclusive sample being less affected than the gap sample.

7.4.4 Jet Cleaning

The analysis removes events with jets that have $p_{\mathrm{T}} > 20$ GeV and that fail the loose cleaning selection. This event-level jet cleaning selection has been compared to a jet-level cleaning selection, which only removes the jets that fail the loose cleaning selection, and the impact of rejecting events due to bad jets is less than 1% for all of the final distributions.

The loose jet cleaning selection does not remove all of the bad jets, and to assess the effect of the remaining bad jets, the final distributions are compared to the more stringent "medium" jet cleaning, which removes a higher proportion of bad jets. The concern with using the medium jet cleaning selection is that it has inefficiencies for good jets that have a low p_{T}. These inefficiencies have been estimated in [39]. The differences from comparing the medium and loose cleaning

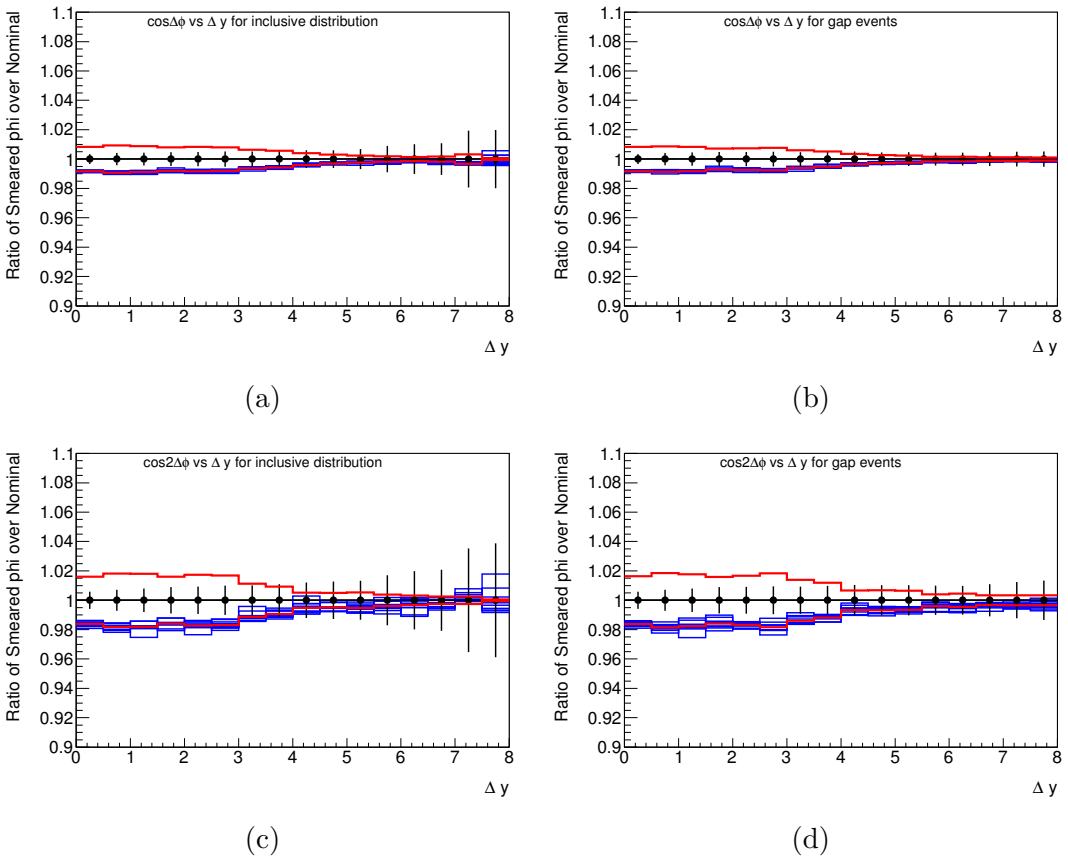

Figure 7.9: The ratio of the ϕ-smeared reconstructed PYTHIA sample to the standard reconstructed PYTHIA sample of (a,b) $\langle\cos(\pi - \Delta\phi)\rangle$ and (c,d) $\langle\cos(2\Delta\phi)\rangle$ as a function of Δy using the (a,c) inclusive and (b,d) gap samples. The blue histograms represent the ten implementations of the increased jet ϕ resolution, the two red histograms show the uncertainty band found from the average of the blue histograms, and the black points show the PYTHIA statistical uncertainties.

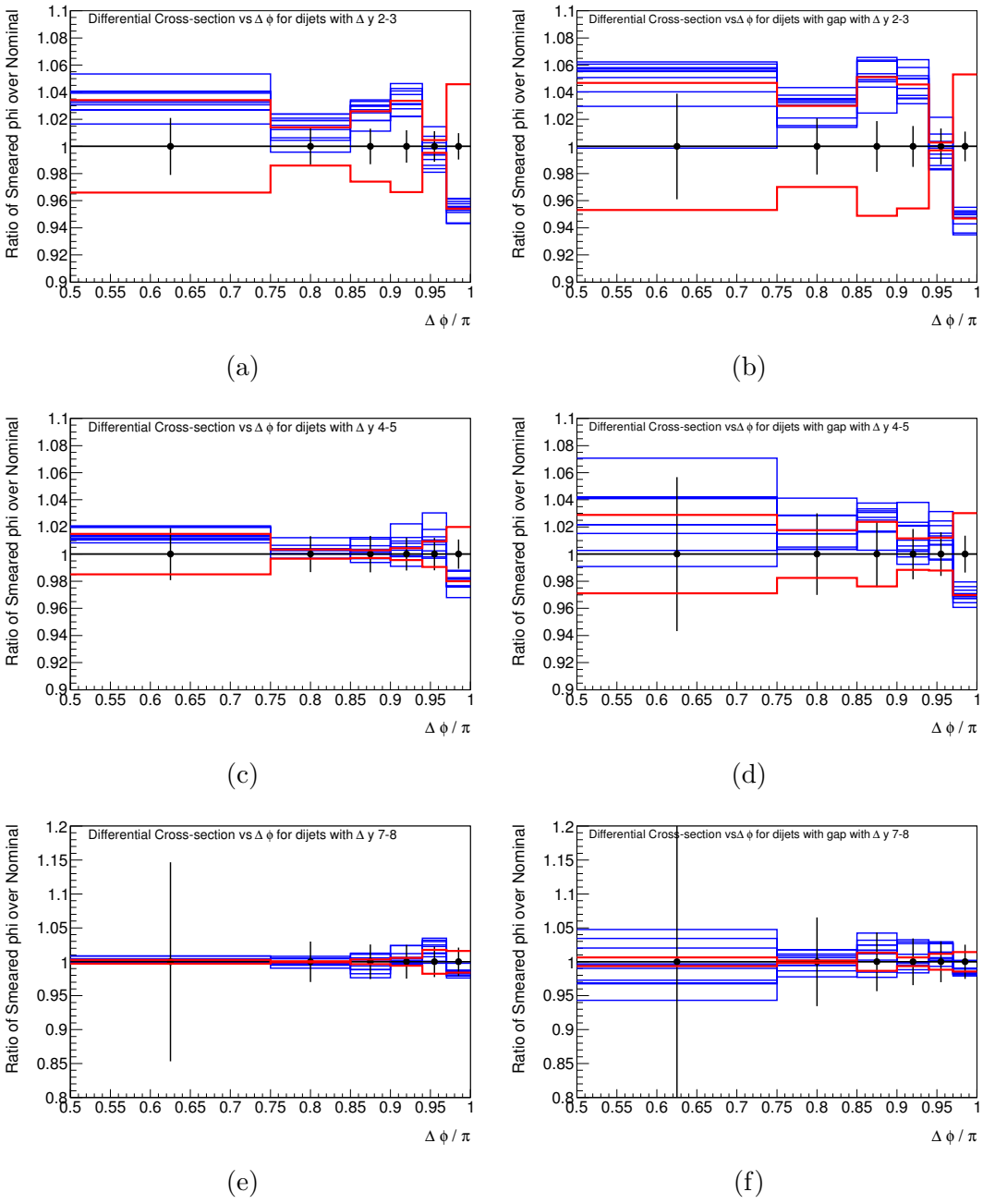

Figure 7.10: The ratio of the ϕ-smeared reconstructed PYTHIA sample to the standard reconstructed PYTHIA sample of the $d\sigma/d\Delta\phi$ distribution for (a,b) $2 < \Delta y < 3$, (c,d) $5 < \Delta y < 6$ and (e,f) $7 < \Delta y < 8$ using the (a,c,e) inclusive and (b,d,f) gap samples. The blue histograms represent the ten implementations of the increased jet ϕ resolution, the two red histograms show the uncertainty band found from the average of the blue histograms, and the black points show the PYTHIA statistical uncertainties.

selections will come from removing more bad jets and the good jet inefficiencies. To try to isolate the effect due to the bad jets on each distribution, the medium jet cleaning selection are compared to events that have the inefficiencies from [39] applied to events selected using the loose cleaning selection, termed "inefficient loose cleaning". Figures 7.11 – 7.13 show the ratio of both medium cleaning selection and inefficient loose cleaning selection to the loose cleaning selection for the main final distributions.

Changing to the medium cleaning causes the gap fraction to increase with a maximum difference of $\approx 2\%$ at high Δy and $\approx 1\%$ at low Q_0. This increase in the gap fraction results from gap events having less jets than inclusive events, meaning they are less likely to fail the jet cleaning selection . The inefficient loose cleaning matches the medium data well, which would indicate that the effect from bad jets on the gap fraction is small and the main effect is from the good jet inefficiency. Similar results are seen for the gap fraction against Q_0 in the other slices in Δy.

The ratios of the $\langle\cos(\pi - \Delta\phi)\rangle$ and $\langle\cos(2\Delta\phi)\rangle$ distributions show that the effect of the bad jets and inefficiency is small for both gap and inclusive events. At larger Δy there are some statistical fluctuations.

There is a reduction of $\approx 2\%$ for the $d\sigma/d\Delta\phi$ with both the gap and inclusive sample when the medium cleaning selection is applied. The inefficient loose cleaning selection causes a reduction to $d\sigma/d\Delta\phi$ of between $2-4\%$, and crucially it falls to below the medium jet cleaning ratio. This indicates that the inefficiencies of the medium jet cleaning on good jets are overestimated. The maximum effect from the bad jets would occur if there was no inefficiency in the medium jet cleaning, ie corresponding to the deviation of the distribution from unity. For the slice of $2 < \Delta y < 3$, the maximum deviation is 3%, which would be a very conservative estimate of the effect. Given that this is an overestimation of a

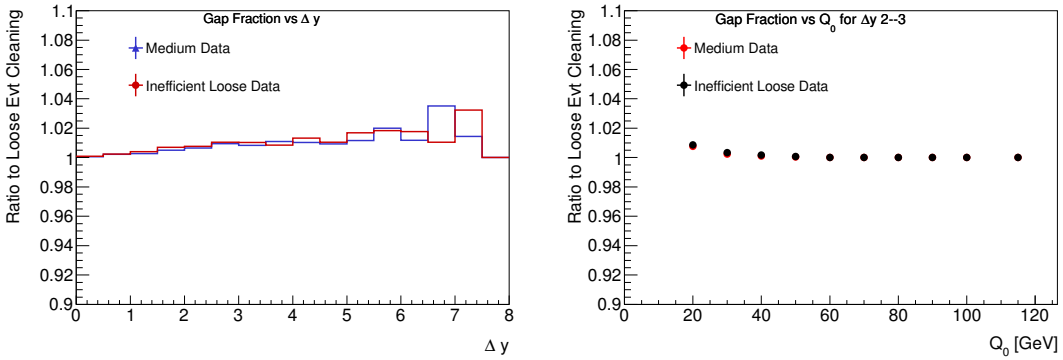

(a) (b)

Figure 7.11: The ratio for both medium cleaning selection and inefficient loose cleaning selection to the loose cleaning selection for the gap fraction as a function of (a) Δy and (b) Q_0.

effect that is expected to be small, and the uncertainty from the JES adds an uncertainty band of about 20%, this difference is disregarded. The other slices in Δy show a similar results when comparing the difference between medium jet cleaning and loose cleaning to the systematic band from JES.

The method of jet cleaning used this analysis was the loose cleaning definitions and event-level criteria. No bias due to using event-level was found. The loose cleaning definition was used due to the high efficiency for good jets. The effect from bad jets was assessed, and while it is hard to get an accurate value for the effect due to the medium jet inefficiencies for good jets being overestimated, the upper limit of the effect was significantly less than the effect from the JES uncertainty. No systematic uncertainty from cleaning is applied for the final analysis.

7.4.5 Other Systematics

Two other sources of systematic uncertainty were assessed by other members of the analysis team and are outlined in this section [2].

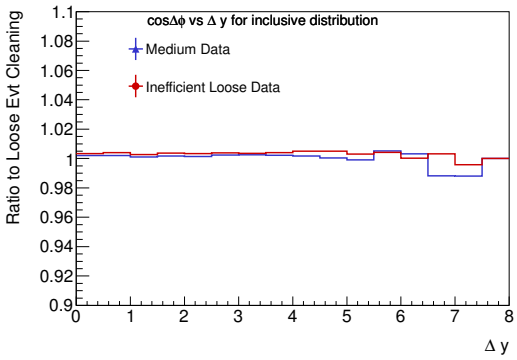

(a)

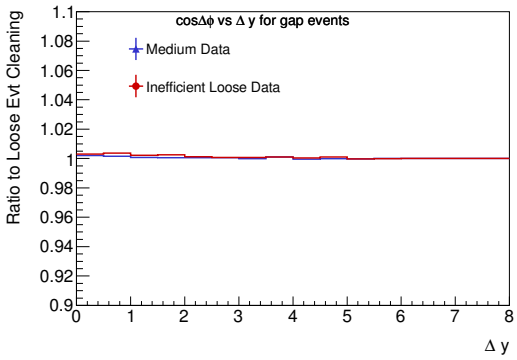

(b)

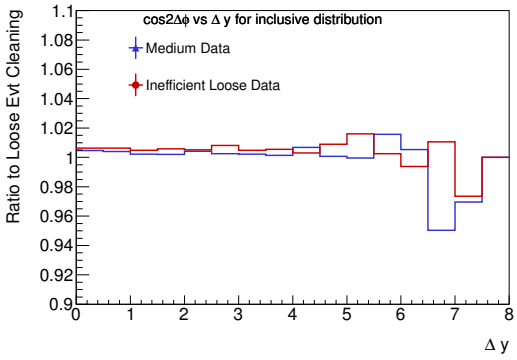

(c)

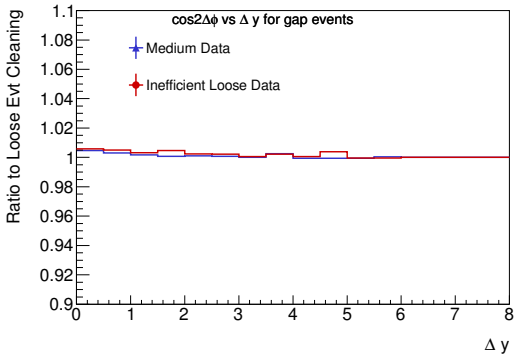

(d)

Figure 7.12: The ratio for both medium cleaning selection and inefficient loose cleaning selection to the loose cleaning selection for (a,b) $\langle\cos(\pi - \Delta\phi)\rangle$ and (c,d)$\langle\cos(2\Delta\phi)\rangle$ as a function of Δy using the (a,c) inclusive and (b,d) gap sample.

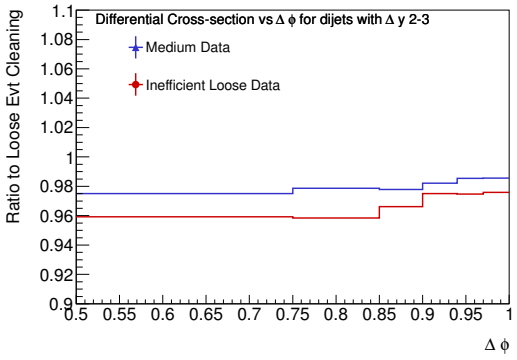

(a)

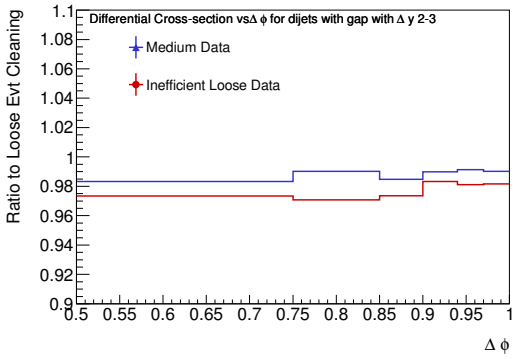

(b)

Figure 7.13: The ratio for both medium cleaning selection and inefficient loose cleaning selection to the loose cleaning selection for the $d\sigma/d\Delta\phi$ distribution for $2 < \Delta y < 3$ using the (a) inclusive and (b) gap sample.

The systematic due to the prescale, luminosity weights and trigger inefficiencies in the trigger strategy was assessed using the PYTHIA sample and found to be negligible in all final distributions.

To correct for detector effects on the final distributions a Bayesian unfolding method [70] was used. This method determines the bin migration in the distributions between particle level and detector level and uses this to unfold the detector effects. Two different uncertainties were assessed and combined in quadrature for the unfolding; one was due to model uncertainty and the other was due to the statistics in the MC sample. The main contribution to the model uncertainty was due to the uncertainty in the shape of the $p_{\mathrm{T}3}$ distribution, where $p_{\mathrm{T}3}$ is the highest p_{T} jet bounded by the dijet system. This $p_{\mathrm{T}3}$ distributions is allowed to vary maximally within the JES uncertainty by weighting the events. Figure 7.14 shows ratio between uncorrected data and MC with the JES uncertainty band and two lines showing the weights that were applied. The unfolding was then recalculated and the uncertainty found from the spread.

7.4.6 Combined Systematics

The systematics studied above were combined with the systematic uncertainties from the unfolding process and the trigger inefficiencies, to produce the overall systematic uncertainty, some of which are shown in Figures 7.15 – 7.17. Only effects that are greater than 0.1% are shown on the plots.

The dominant systematic on both the gap fraction and the average number of jets is due to the JES uncertainty, while the unfolding also makes a significant contribution. The effect from trigger inefficiencies is small, and the effects due to jet ϕ resolution and JER is less than 0.1%. The systematic uncertainty on the differential cross-section, $d\sigma/d\Delta\phi$, for both the gap and inclusive sample are dominated by the JES uncertainty and the unfolding. The effect from the ϕ

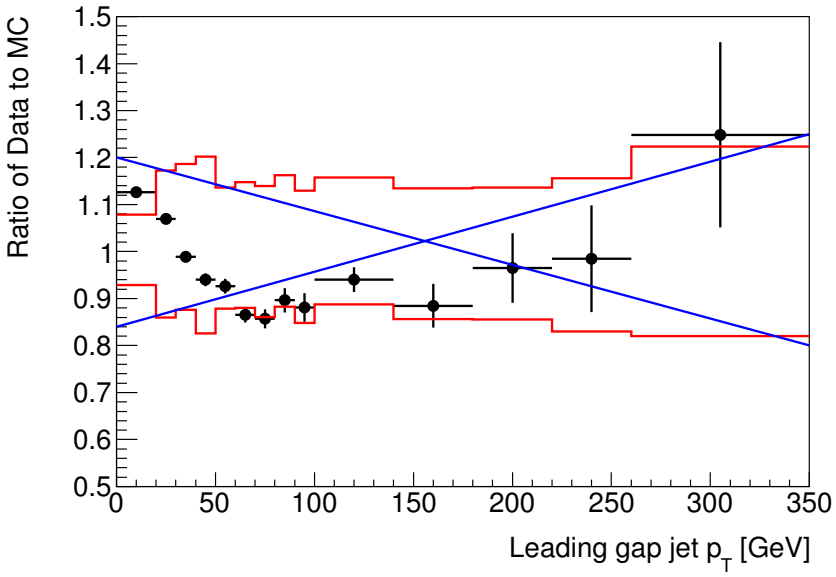

Figure 7.14: Ratio of the p_{T} of the leading gap jet from 2010 uncorrected data to that of the reconstructed PYTHIA sample. The red lines show the JES uncertainty bands and the two blue lines on the plot shows the event reweighting factors.

resolution is small at low $\Delta\phi$, but increases for high $\Delta\phi$.

For the $\langle\cos(2\Delta\phi)\rangle$ using the inclusive sample there is no overall dominant systematic. At low Δy, the uncertainty from the ϕ resolution is dominant, with JES and unfolding uncertainties also contributing. At large Δy, the uncertainty is dominated by the JES and unfolding. For the $\langle\cos(2\Delta\phi)\rangle$ using the gap sample, at low Δy the ϕ resolution is the dominant systematic and at larger Δy all the uncertainties have an effect.

7.5 Comparison of Data and MC Before Unfolding

This section presents the data compared to the reconstructed PYTHIA sample. Figures 7.18 – 7.22 show the data before unfolding compared to PYTHIA. The PYTHIA error bands are the quadrature sum of the statistical error and the JES

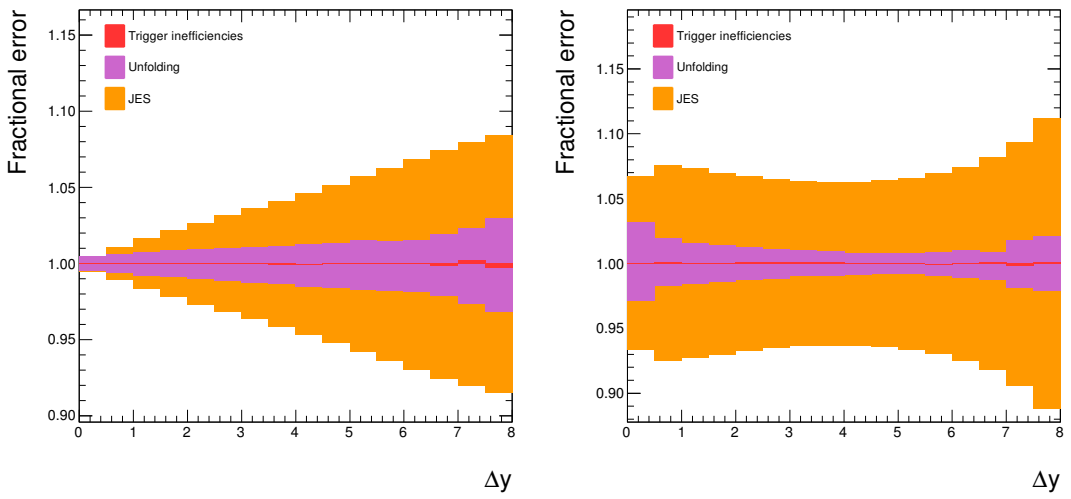

(a) (b)

Figure 7.15: The combined systematics for (a) the gap fraction and (b) the average number of jets in the dijet rapidity region as a function of Δy. The combined systematics are from unfolding, trigger inefficiencies, JES uncertainty, JER and jet ϕ resolution. Only systematics with an effect greater than 0.1% are displayed.

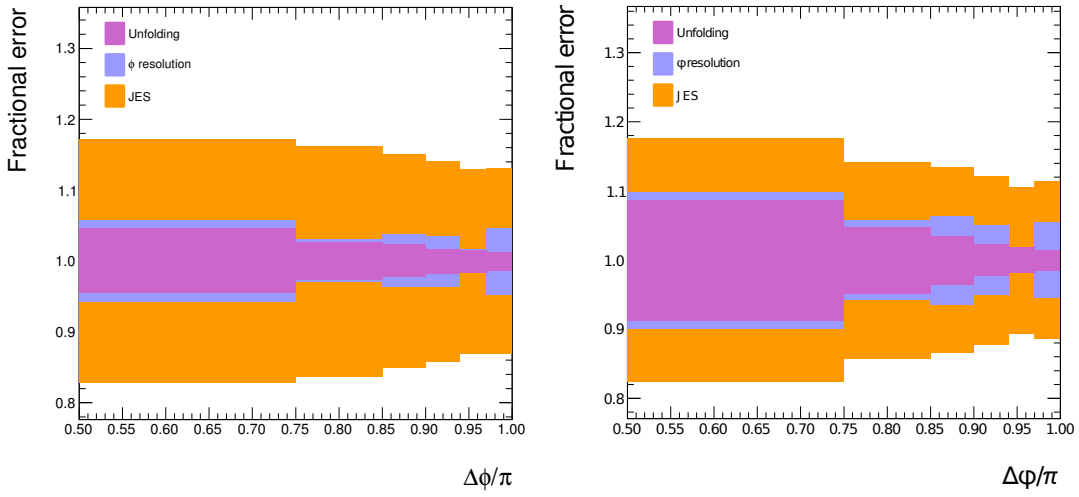

(a) (b)

Figure 7.16: The combined systematics for $d\sigma/d\Delta\phi$ for (a) inclusive events and (b) gap events for $2 < \Delta y < 3$. The combined systematics are from unfolding, trigger inefficiencies, JES uncertainty, JER and jet ϕ resolution. Only systematics with an effect greater than 0.1% are displayed.

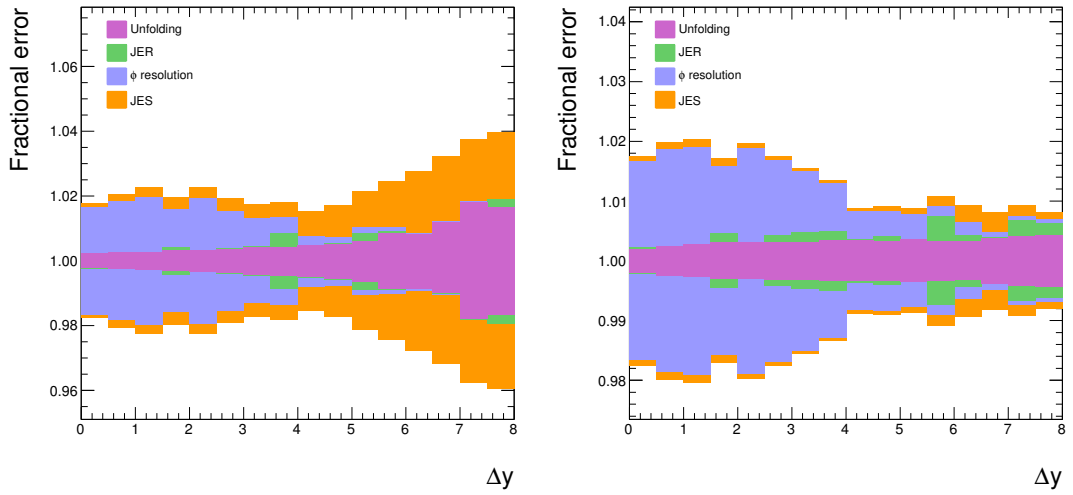

(a) (b)

Figure 7.17: The combined systematics for the $\langle\cos(2\Delta\phi)\rangle$ as a function of Δy for (a) inclusive events and (b) gap events. The combined systematics are from unfolding, trigger inefficiencies, JES uncertainty, JER and jet ϕ resolution. Only systematics with an effect greater than 0.1% are displayed.

uncertainty bands.

The gap fraction measured from data falls as a function of Δy, up to $\Delta y > 5.5$ where it starts to level off. The PYTHIA gap fraction curve is consistently below the data up to a $\Delta y = 6.5$. PYTHIA then rises for the larges Δy bins, and has a higher gap fraction for $\Delta y > 7$. The mean multiplicity of jets in the rapidity region increases as a function of Δy, to a peak of about 1.2 at $\Delta y = 7$, and then plateaus. Both the flattening out of the gap fraction and the plateau in the mean number of jets could be due to PDF effects, such as those seen in the previous analysis for dijets with large Δy and $\overline{p_{\mathrm{T}}}$.

Figure 7.19 show $d^2\sigma/dyd\Delta\phi$ for $2 < \Delta y < 3$, $4 < \Delta y < 5$, and $7 < \Delta y < 8$ for inclusive events and gap events. PYTHIA is consistently below the data, especially at high $\Delta\phi$ for $2 < \Delta y < 3$ and $4 < \Delta y < 5$ slices where it is about 20% below the data. In the $7 < \Delta y < 8$ slice, the PYTHIA results are still consistently below the data, but they agree within the JES uncertainty band.

The cross-section from PYTHIA does not agree with the measured cross-section, however there are potentially large PDF uncertainties that have not been shown.

The $\langle\cos(\pi - \Delta\phi)\rangle$ distribution, shown in Figure 7.20, for the inclusive events have a value of about 0.94 for $\Delta y < 2$, where a $\langle\cos(\pi - \Delta\phi)\rangle$ value of 1 corresponds to perfectly back-to-back jets in azimuth. As the Δy increases, the jets become less back-to-back and the value of $\langle\cos(\pi - \Delta\phi)\rangle$ falls and then levels off at a value of about 0.86 for $\Delta y = 6$. As the Δy increases, the available phase space to emit into is larger due to the jets being at very high energies. For the gap events, the $\langle\cos(\pi - \Delta\phi)\rangle$ at low Δy starts at a similar level to the inclusive events, but then slowly rises to a maximum of about 0.96. When the Δy is low, emissions can fall outside the rapidity region, but as the Δy increases this region becomes smaller, and the jet veto is stopping hard emission into the rapidity region, thus the dijets are more back-to-back. The PYTHIA distribution show a slightly different shape from the data. At both low and high Δy, the $\langle\cos(\pi - \Delta\phi)\rangle$ for PYTHIA is higher than the data for both gap and inclusive events. In the range $2 < \Delta y < 5.5$, PYTHIA describes the data well. The shape of the $\langle\cos(2\Delta\phi)\rangle$ distribution, shown in Figure 7.21, has a similar explanation as for the $\langle\cos(\pi - \Delta\phi)\rangle$ distribution, and shows similar features. For both inclusive and gap events, PYTHIA's description of the $\langle\cos(2\Delta\phi)\rangle$ distribution is too low at low Δy and too high at high Δy.

Figure 7.22 shows the gap fraction as a function of the jet veto scale, Q_0, for the Δy ranges $2 < \Delta y < 3$, $4 < \Delta y < 5$, and $7 < \Delta y < 8$. As Q_0 is increased, fewer events are defined as gap events, until at high Q_0 the gap fraction is at 1.0. In the range $2 < \Delta y < 3$, the PYTHIA gap fraction is lower than the data for $Q_0 < 50$ GeV, though it is within the JES uncertainty. In the range $4 < \Delta y < 5$, the PYTHIA gap fraction describes the data well for the full Q_0 range. For dijets within the range $7 < \Delta y < 8$, the PYTHIA gap fraction is higher than the data

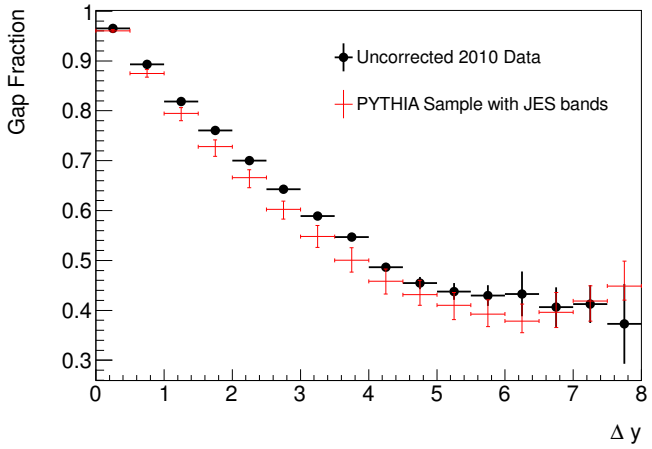

(a)

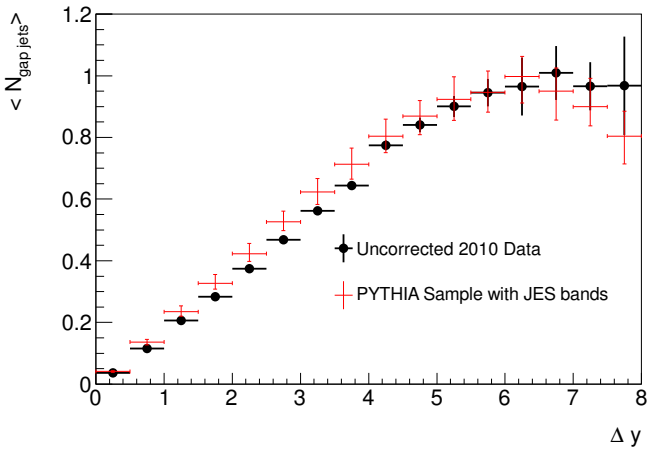

(b)

Figure 7.18: (a) The gap fraction and (b) the mean number of jets in the rapidity region bounded by the dijet system as a function of Δy for 2010 data before unfolding (black points) and reconstructed PYTHIA sample (red points).

until both gap fractions plateau at 1.0.

This extended analysis going to larger Δy has show similar features to the previous analysis. A flattening out of the gap fraction and mean number of jets at large Δy has been observed, which was not observed previously. This could be due to PDF effects, although colour singlet exchange could also explain the shape.

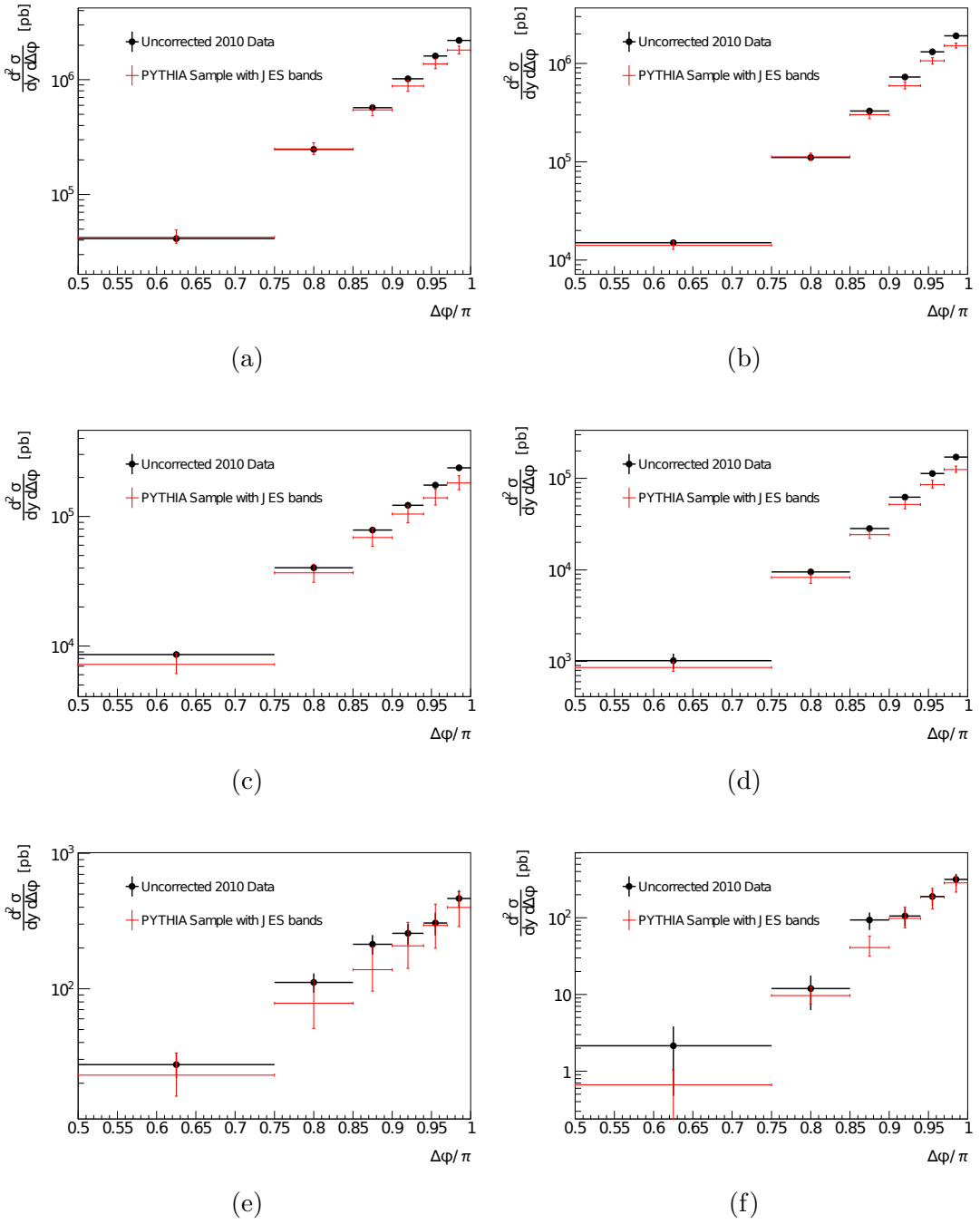

Figure 7.19: $d^2\sigma/dyd\Delta\phi$ for (a,c,e) the inclusive and (b,d,f) gap samples for a dijet separation of (a,b) $2 < \Delta y < 3$, (c,d) $4 < \Delta y < 5$ and (e,f) $7 < \Delta y < 8$ for 2010 data before unfolding (black points) and reconstructed PYTHIA sample (red points).

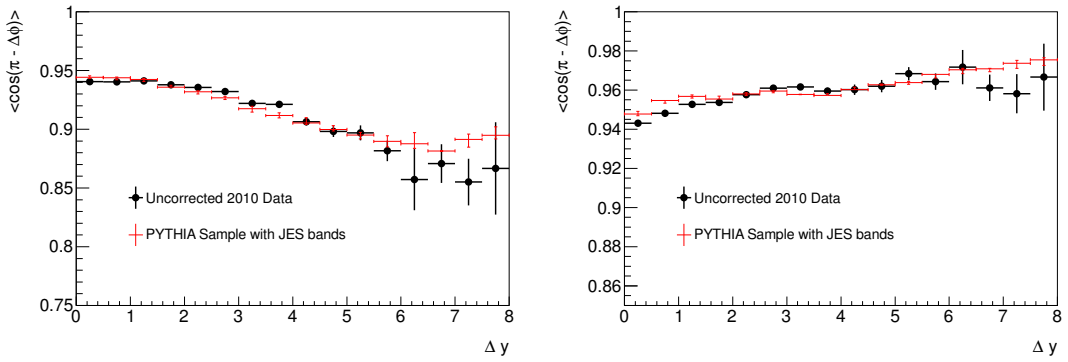

(a) (b)

Figure 7.20: $\langle\cos(\pi - \Delta\phi)\rangle$ as a function of Δy for (a) inclusive and (b) gap events for 2010 data before unfolding (black points) and reconstructed PYTHIA sample (red points).

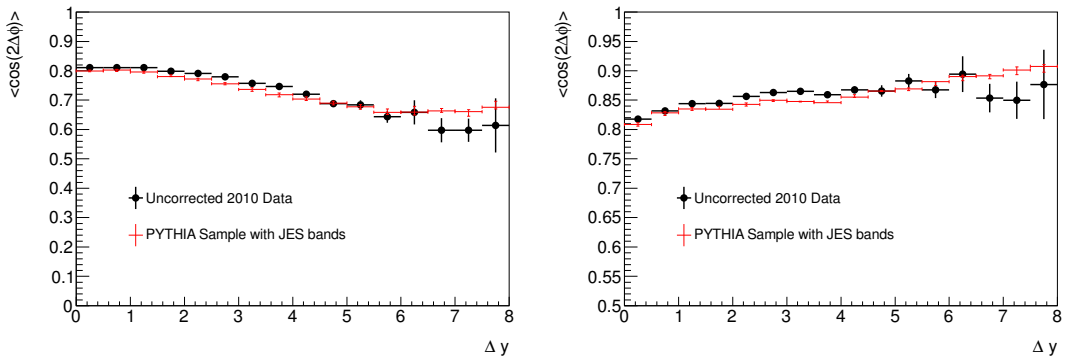

(a) (b)

Figure 7.21: $\langle\cos(2\Delta\phi)\rangle$ as a function of Δy for (a) inclusive and (b) gap events for 2010 data before unfolding (black points) and reconstructed PYTHIA sample (red points).

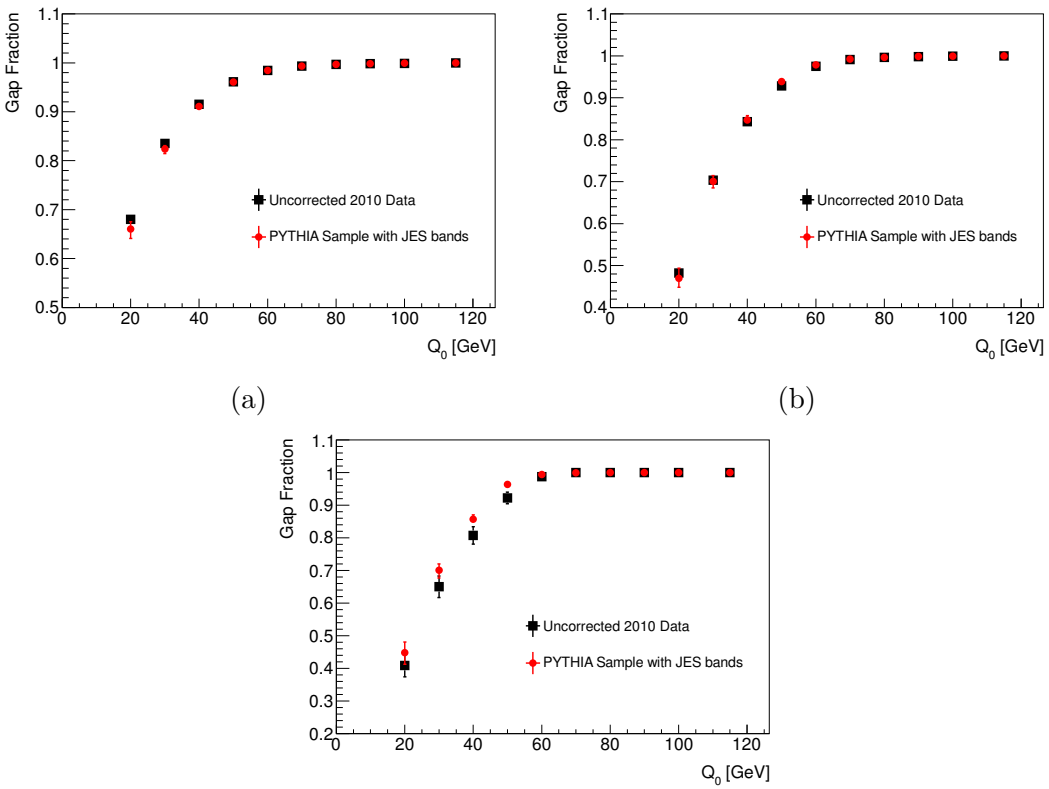

Figure 7.22: The gap fraction against Q_0 for (a) $2 < \Delta y < 3$, (b) $4 < \Delta y < 5$ and (c) $7 < \Delta y < 8$ for 2010 data before unfolding (black points) and reconstructed PYTHIA sample (red points).

Chapter 8

Summary and Conclusions

In this thesis a summary of two precision jet measurements are presented that probe higher-order QCD phenomena by studying the amount of radiation from a dijet system.

To make precision jet measurements, a good understanding of the detector and its response to jets is vital. The monitoring of the calorimeter high-level trigger, which is used in the analyses to trigger events, has been detailed. The trigger was shown to be stable over different data periods, and problems, such as noisy cells, could be monitored and masked. The performance of jets within the calorimeter was also assessed. The dijet p_{T} balance method was used to extend a determination of the central jet energy scale uncertainty out to y of 4.4, and the effect from pile-up and a closure of the method were studied. In addition, some properties of jets in the transition region between the end-cap and FCal and in the FCal were studied and compared to different showering models. The closure of the dijet p_{T} balance method and the properties of the jets in the transition region between the end-cap and FCal and in the FCal itself have been published as an ATLAS conference note [45].

Dijet production with a jet veto for fixed regions of phase space was studied for rapidity separations of up to six units in rapidity with average p_{T} of the dijets

from 50 to 500 GeV. The measurement of the fraction of events that survived a jet veto were compared to PYTHIA, HERWIG++ and ALPGEN event generators as well as to next-to-leading-order predictions from POWHEG, interfaced with the partons showering from PYTHIA and HERWIG, and to a prediction using the HEJ generator. Two different dijet selections were studied, the leading p_{T} dijet selection and the forward/backward dijet selection. No prediction agreed in all the areas of phase space considered. POWHEG + PYTHIA had the best agreement with data, but differences were observed at high Δy. HEJ described the data as a function of Δy, but only for low $\overline{p_{\mathrm{T}}}$; at high $\overline{p_{\mathrm{T}}}$ the gap fraction was too high. POWHEG + HERWIG gave a poor description of the data with too low a gap fraction throughout. The mean multiplicity of jets in the rapidity region has also been presented for the leading p_{T} dijet selection. The activity of HEJ was significantly lower than the data for all but the lowest Δy bin. Given the agreement for the gap fraction, it seems HEJ describes the veto jet well, but does not cope well with any additional jets beyond that. POWHEG + HERWIG had too much activity throughout, which correlates well with the predicted gap fraction that is too low. POWHEG + PYTHIA gave the best description of the data, although they did deviate at high Δy. The results of this analysis have been published in JHEP [1] as well in the ATLAS conference notes [59, 71].

A preliminary analysis studying emissions from very high rapidity separated jets was also presented, with a measurement up to a separation of eight units in rapidity. The systematic uncertainties from the data selection and jet uncertainties were assessed. In the analysis both the gap fraction and the mean number of jets in the rapidity region between the dijet system were studied. The azimuthal decorrelation variables, $d\sigma/d\Delta\phi$, $\langle\cos(\pi - \Delta\phi)\rangle$ and $\langle\cos(2\Delta\phi)\rangle$ were also studied. The data were compared to fully reconstructed PYTHIA. In the high Δy region, the gap fraction levelled off in the data. This feature was only observed

at high p_{T} in the previous analysis. This maybe due to PDF effects, or maybe signs of colour singlet exchange. The shape of the PYTHIA distributions in the variables $\langle\cos(\pi - \Delta\phi)\rangle$ and $\langle\cos(2\Delta\phi)\rangle$ were different to the data, with the data having a lower value at very high Δy. The results of this second analysis are currently being reviewed internally by the ATLAS collaboration [2].

The jet veto analyses studied in this thesis have probed regions that are sensitive to higher order QCD emissions, and have tested both HEJ, which models hard, wide-angle emissions, and the NLO calculations plus parton showering of POWHEG + PYTHIA and POWHEG + HERWIG. In certain regions neither gave a good description and since the publication other models have been tested to try to describe these data.

References

[1] ATLAS Collaboration, *Measurement of dijet production with a veto on additional central jet activity in pp collisions at $\sqrt{s} = 7$ TeV using the ATLAS detector*, JHEP **1109** (2011) 053, arXiv:1107.1641 [hep-ex].

[2] ATLAS Collaboration, *Measurement of dijet production and azimuthal decorrelation with a jet veto in pp collision at $\sqrt{s} = 7$ TeV using the ATLAS detector*, ATL-COM-PHYS-2012-1220 (2012). https://cds.cern.ch/record/1473139.

[3] Particle Data Group Collaboration, J. Beringer et al., *Review of Particle Physics (RPP)*, Phys.Rev. **D86** (2012) 010001.

[4] J. M. Campbell, J. Huston, and W. Stirling, *Hard Interactions of Quarks and Gluons: A Primer for LHC Physics*, Rept.Prog.Phys. **70** (2007) 89, arXiv:hep-ph/0611148 [hep-ph].

[5] R. K. Ellis, W. J. Stirling, and B. Webber, *QCD and Collider Physics*, Camb.Monogr.Part.Phys.Nucl.Phys.Cosmol. **8** (1996) 1–435.

[6] H1 and ZEUS Collaboration, F. Aaron et al., *Combined Measurement and QCD Analysis of the Inclusive* e^+*– p Scattering Cross Sections at HERA*, JHEP **1001** (2010) 109, arXiv:0911.0884 [hep-ex].

[7] M. Guzzi, P. Nadolsky, E. Berger, H.-L. Lai, F. Olness, et al., *CTEQ10*

parton distributions and other developments in the global QCD analysis, arXiv:1101.0561 [hep-ph].

[8] A. Martin, W. Stirling, R. Thorne, and G. Watt, *Parton distributions for the LHC*, Eur.Phys.J. **C63** (2009) 189–285, arXiv:0901.0002 [hep-ph].

[9] ATLAS Collaboration, *Measurement of inclusive jet and dijet production in pp collisions at $\sqrt{s} = 7$ TeV using the ATLAS detector*, Phys. Rev. **D86** (2012) 014022, arXiv:1112.6297 [hep-ex].

[10] J. C. Collins, *Light cone variables, rapidity and all that*, arXiv:hep-ph/9705393 [hep-ph].

[11] S. Marzani, J. Forshaw, and J. Keates, *Gaps between jets and soft gluon resummation*, arXiv:0906.2418 [hep-ph].

[12] J. R. Andersen and J. M. Smillie, *Constructing All-Order Corrections to Multi-Jet Rates*, JHEP **1001** (2010) 039, arXiv:0908.2786 [hep-ph].

[13] J. R. Forshaw, A. Kyrieleis, and M. Seymour, *Gaps between jets in the high energy limit*, JHEP **0506** (2005) 034, arXiv:hep-ph/0502086 [hep-ph].

[14] A. H. Mueller and H. Navelet, *An Inclusive Minijet Cross-Section and the Bare Pomeron in QCD*, Nucl.Phys. **B282** (1987) 727.

[15] B. Ducloue, L. Szymanowski, and S. Wallon, *Mueller-Navelet jets at LHC: the first complete NLL BFKL study*, arXiv:1208.6111 [hep-ph].

[16] C. Marquet, *Testing BFKL evolution with Mueller-Navelet jets*, Acta Phys.Polon.Supp. **1** (2008) 463–467, arXiv:0712.0746 [hep-ph].

[17] S. Alioli, J. R. Andersen, C. Oleari, E. Re, and J. M. Smillie, *Probing higher-order corrections in dijet production at the LHC*, Phys.Rev. **D85** (2012) 114034, arXiv:1202.1475 [hep-ph].

[18] J. R. Andersen and J. M. Smillie, *High Energy Description of Processes with Multiple Hard Jets*, Nucl.Phys.Proc.Suppl. **205-206** (2010) 205–210, arXiv:1007.4449 [hep-ph].

[19] J. Forshaw, J. Keates, and S. Marzani, *Jet vetoing at the LHC*, JHEP **0907** (2009) 023, arXiv:0905.1350 [hep-ph].

[20] M. Cacciari, G. P. Salam, and G. Soyez, *The Anti-k(t) jet clustering algorithm*, JHEP **0804** (2008) 063, arXiv:0802.1189 [hep-ph].

[21] ATLAS Collaboration, *Study of Jet Shapes in Inclusive Jet Production in pp Collisions at $\sqrt{s} = 7$ TeV using the ATLAS Detector*, Phys.Rev. **D83** (2011) 052003, arXiv:1101.0070 [hep-ex].

[22] T. Sjostrand, S. Mrenna, and P. Z. Skands, *PYTHIA 6.4 Physics and Manual*, JHEP **0605** (2006) 026, arXiv:hep-ph/0603175 [hep-ph].

[23] B. Andersson, G. Gustafson, G. Ingelman, and T. Sjostrand, *Parton Fragmentation and String Dynamics*, Phys.Rept. **97** (1983) 31–145.

[24] ATLAS Collaboration, *Charged particle multiplicities in p p interactions at $\sqrt{s}$ = 0.9 and 7 TeV in a diractive limited phase-space measured with the ATLAS detector at the LHC and new PYTHIA6 tune*, ATLAS-COM-CONF-2010-031 (2010). https://cds.cern.ch/record/1277665.

[25] GEANT4 Collaboration, S. Agostinelli et al., *GEANT4: A Simulation toolkit*, Nucl.Instrum.Meth. **A506** (2003) 250–303.

[26] M. Bahr, S. Gieseke, M. Gigg, D. Grellscheid, K. Hamilton, et al., *Herwig++ Physics and Manual*, Eur.Phys.J. **C58** (2008) 639–707, arXiv:0803.0883 [hep-ph].

[27] R. D. Field and S. Wolfram, *A QCD Model for e+ e- Annihilation*, Nucl.Phys. **B213** (1983) 65.

[28] S. Gieseke, C. Rohr, and A. Siodmok, *Colour reconnections in Herwig++*, arXiv:1206.0041 [hep-ph].

[29] S. Frixione, P. Nason, and C. Oleari, *Matching NLO QCD computations with Parton Shower simulations: the POWHEG method*, JHEP **0711** (2007) 070, arXiv:0709.2092 [hep-ph].

[30] S. Alioli, K. Hamilton, P. Nason, C. Oleari, and E. Re, *Jet pair production in POWHEG*, JHEP **1104** (2011) 081, arXiv:1012.3380 [hep-ph].

[31] S. Alioli, P. Nason, C. Oleari, and E. Re, *A general framework for implementing NLO calculations in shower Monte Carlo programs: the POWHEG BOX*, JHEP **1006** (2010) 043, arXiv:1002.2581 [hep-ph].

[32] J. R. Andersen and J. M. Smillie, *Multiple Jets at the LHC with High Energy Jets*, JHEP **1106** (2011) 010, arXiv:1101.5394 [hep-ph].

[33] ATLAS Collaboration, *Luminosity Determination in pp Collisions at $\sqrt{s} = 7$ TeV Using the ATLAS Detector at the LHC*, Eur.Phys.J. **C71** (2011) 1630, arXiv:1101.2185 [hep-ex].

[34] ATLAS Collaboration, *The ATLAS Experiment at the CERN Large Hadron Collider*, JINST **3** (2008) S08003.

[35] ATLAS Collaboration, *Electron performance measurements with the ATLAS detector using the 2010 LHC proton-proton collision data*, Eur.Phys.J. **C72** (2012) 1909, arXiv:1110.3174 [hep-ex].

[36] W. Lampl, S. Laplace, D. Lelas, P. Loch, H. Ma, et al., *Calorimeter clustering algorithms: Description and performance*,

ATL-LARG-PUB-2008-002, ATL-COM-LARG-2008-003 (2008). https://cds.cern.ch/record/1099735.

[37] ATLAS Collaboration, *Performance of the ATLAS Trigger System in 2010*, Eur.Phys.J. **C72** (2012) 1849, arXiv:1110.1530 [hep-ex].

[38] ATLAS Collaboration, *In-situ jet energy scale and jet shape corrections for multiple interactions in the first ATLAS data at the LHC*, ATLAS-COM-CONF-2011-009 (2011). http://cdsweb.cern.ch/record/1325337.

[39] ATLAS Collaboration, *Jet energy measurement with the ATLAS detector in proton-proton collisions at* $\sqrt{s} = 7$ *TeV*, arXiv:1112.6426 [hep-ex].

[40] ATLAS Collaboration, *Jet energy scale and its systematic uncertainty for jets produced in proton-proton collisions at* $\sqrt{s} = 7$ *TeV and measured with the ATLAS detector*, ATLAS-CONF-2010-056 (2010). https://cds.cern.ch/record/1281329.

[41] ATLAS Collaboration, *Jet energy resolution and selection efficiency relative to track jets from in-situ techniques with the ATLAS Detector Using Proton-Proton Collisions at a Center of Mass Energy* $\sqrt{s} = 7$ *TeV*, ATLAS-CONF-2010-054 (2010). https://cds.cern.ch/record/1281311.

[42] ATLAS Collaboration, *Jet energy resolution and selection efficiency to track jets from in-situ techniques with the Detector Using Proton-Proton Collisions at a Center Mass Energy* $\sqrt{s} = 7$ *TeV*, ATLAS-CONF-2010-054 (2010). https://cds.cern.ch/record/1281311.

[43] ATLAS Collaboration, *Pile-up corrections for jets from proton-collisions at* $\sqrt{s} = 7$ *TeV in ATLAS in 2011*, ATLAS-CONF-2012-064 (2012). https://cds.cern.ch/record/1459529.

[44] ATLAS Collaboration, *Jet energy scale and its systematic uncertainty in proton-proton collisions at $\sqrt{s} = 7$ TeV with ATLAS 2011 data*, ATLAS-CONF-2013-004 (2012). https://cds.cern.ch/record/1509552.

[45] ATLAS Collaboration, *In-situ pseudo-rapidity inter-calibration to jet energy scale uncertainty and calorimeter in the forward region*, ATLAS-CONF-2010-055 (2010). https://cds.cern.ch/record/1281312.

[46] E. Abat, J. Abdallah, T. Addy, P. Adragna, M. Aharrouche, et al., *Response and shower topology of 2 to 180 GeV measured with the ATLAS barrel calorimeter at the test-beam and comparison to Monte Carlo simulations*, ATL-CAL-PUB-2010-001 (2010). https://cds.cern.ch/record/1263861.

[47] J. Beringer, G. Folger, F. Gianotti, A. Ribon, J. Wellisch, D. Barberis, M. Cervetto, and B. Osculati, *Validation of Geant4 hadronic physics*, Nuclear Science Symposium Conference Record, 2003 IEEE **1** (2003) 494 – 498 Vol.1.

[48] M. Guthrie, R. Alsmiller, and H. Bertini, *Calculation of the capture of negative pions in light elements and comparison with experiments pertaining to cancer radiotherapy*, Nucl.Instrum.Meth. **66** (1968) 29–36.

[49] B. Andersson, G. Gustafson, and B. Nilsson-Almqvist, *A Model for Low p(t) Hadronic Reactions, with Generalizations to Hadron - Nucleus and Nucleus-Nucleus Collisions*, Nucl.Phys. **B281** (1987) 289.

[50] ATLAS Collaboration, *Properties of Jets and Inputs to Jet Reconstruction Calibration with the ATLAS Detector Using Proton-Collisions at $\sqrt{s} = 7$ TeV*, ATLAS-CONF-2010-053 (2010). https://cds.cern.ch/record/1281310.

[51] ZEUS Collaboration, M. Derrick et al., *Rapidity gaps between jets in photoproduction at HERA*, Phys.Lett. **B369** (1996) 55–68, arXiv:hep-ex/9510012 [hep-ex].

[52] H1 Collaboration, C. Adloff et al., *Energy flow and rapidity gaps between jets in photoproduction at HERA*, Eur.Phys.J. **C24** (2002) 517–527, arXiv:hep-ex/0203011 [hep-ex].

[53] ZEUS Collaboration, S. Chekanov et al., *Photoproduction of events with rapidity gaps between jets at HERA*, Eur.Phys.J. **C50** (2007) 283–297, arXiv:hep-ex/0612008 [hep-ex].

[54] D0 Collaboration, S. Abachi et al., *Rapidity gaps between jets in $p\bar{p}$ collisions at $\sqrt{s} = 1.8$ TeV*, Phys.Rev.Lett. **72** (1994) 2332–2336.

[55] CDF Collaboration, F. Abe et al., *Observation of rapidity gaps in $\bar{p}p$ collisions at 1.8 TeV*, Phys.Rev.Lett. **74** (1995) 855–859.

[56] CDF Collaboration, F. Abe et al., *Events with a rapidity gap between jets in $\bar{p}p$ collisions at $\sqrt{s} = 630$ GeV*, Phys.Rev.Lett. **81** (1998) 5278–5283.

[57] D0 Collaboration, B. Abbott et al., *Probing hard color-singlet exchange in $p\bar{p}$ collisions at $\sqrt{s} = 630$ GeV and 1800 GeV*, Phys.Lett. **B440** (1998) 189–202, arXiv:hep-ex/9809016 [hep-ex].

[58] CDF Collaboration, F. Abe et al., *Dijet production by color - singlet exchange at the Fermilab Tevatron*, Phys.Rev.Lett. **80** (1998) 1156–1161.

[59] ATLAS Collaboration, *Dijet production with a jet veto in pp collisions at $\sqrt{s} = 7$ TeV*, ATLAS-CONF-2010-085 (2010). https://cds.cern.ch/record/1298856.

[60] ATLAS Collaboration, *Measurement of dijet production with a jet veto in pp collisions at $\sqrt{s} = 7$ TeV using the ATLAS detector*, ATL-COM-PHYS-2011-077 (2011). https://cds.cern.ch/record/1325367.

[61] Y. Hatta, C. Marquet, C. Royon, G. Soyez, T. Ueda, et al., *A QCD description of the ATLAS jet veto measurement*, arXiv:1301.1910 [hep-ph].

[62] E. Gerwick, T. Plehn, S. Schumann, and P. Schichtel, *Scaling Patterns for QCD Jets*, JHEP **1210** (2012) 162, arXiv:1208.3676 [hep-ph].

[63] S. Hoeche and M. Schonherr, *Uncertainties in next-to-leading order plus parton shower matched simulations of inclusive jet and dijet production*, Phys.Rev. **D86** (2012) 094042, arXiv:1208.2815 [hep-ph].

[64] S. Marzani, *Probing colour flow with jet vetoes*, arXiv:1205.6808 [hep-ph].

[65] R. M. Duran Delgado, J. R. Forshaw, S. Marzani, and M. H. Seymour, *The dijet cross section with a jet veto*, JHEP **1108** (2011) 157, arXiv:1107.2084 [hep-ph].

[66] CMS Collaboration, S. Chatrchyan et al., *Ratios of dijet production cross sections as a function of the absolute difference in rapidity between jets in proton-proton collisions at $\sqrt{s} = 7$ TeV*, Eur.Phys.J. **C72** (2012) 2216, arXiv:1204.0696 [hep-ex].

[67] ATLAS Collaboration, *Measurement of Dijet Azimuthal Decorrelations in pp Collisions at $\sqrt{s} = 7$ TeV*, Phys.Rev.Lett. **106** (2011) 172002, arXiv:1102.2696 [hep-ex].

[68] D0 Collaboration, V. Abazov et al., *Measurement of dijet azimuthal decorrelations at central rapidities in $p\bar{p}$ collisions at $\sqrt{s} = 1.96$ TeV*, Phys.Rev.Lett. **94** (2005) 221801, arXiv:hep-ex/0409040 [hep-ex].

[69] CMS Collaboration, V. Khachatryan et al., *Dijet Azimuthal Decorrelations in pp Collisions at $\sqrt{s} = 7$ TeV*, Phys.Rev.Lett. **106** (2011) 122003, arXiv:1101.5029 [hep-ex].

[70] G. D'Agostini, *Improved iterative Bayesian unfolding*, arXiv:1010.0632 [physics.data-an].

[71] ATLAS Collaboration, *Measurement of dijet production with a jet veto in collisions at $\sqrt{s} = 7$ TeV using the ATLAS detector*, ATLAS-CONF-2011-038 (2011). https://cds.cern.ch/record/1337788.